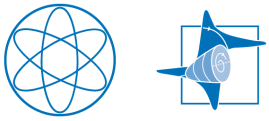

Technische Universität München
Department Physik
E19a - Chemische Physik fern vom Gleichgewicht

Oscillatory systems with nonlinear global coupling: from clusters to chimeras

Lennart Schmidt

Vollständiger Abdruck der von der Fakultät für Physik der Technischen Universität München zur Erlangung des akademischen Grades eines

Doktors der Naturwissenschaften (Dr. rer. nat.)

genehmigten Dissertation.

Vorsitzende: Univ.-Prof. Dr. Chr. M. Papadakis

Prüfer der Dissertation:

1. Univ.-Prof. Dr. K. Krischer
2. Univ.-Prof. Dr. E. Frey, Ludwig-Maximilians-Universität München
3. Univ.-Prof. Dr. U. Feudel (schriftliche Beurteilung), Carl von Ossietzky Universität Oldenburg

Die Dissertation wurde am 19.02.2015 bei der Technischen Universität München eingereicht und durch die Fakultät für Physik am 02.07.2015 angenommen.

Danksagung

An dieser Stelle möchte ich allen danken, die direkt oder indirekt an der Entstehung dieser Arbeit beteiligt waren. Prof. Dr. Katharina Krischer danke ich für die Möglichkeit, die überaus spannenden Welten der nichtlinearen Dynamik zu erforschen, die vielen Diskussionen und motivierenden Gespräche und die zahlreichen Konferenzteilnahmen, die sie ermöglicht hat. Ihre Begeisterung ist absolut ansteckend. Dr. Vladimir García-Morales danke ich für die Unterstützung und die vielen guten Ideen. Konrad Schönleber und Carla Zensen, die maßgeblich die Musterbildung im experimentellen System untersucht haben, danke ich für die produktive Zusammenarbeit und die inspirierenden Diskussionen. Weiterhin danke ich Sindre Haugland für die Entdeckung und Untersuchung der Alternating Chimera States.

Der ganzen Arbeitsgruppe E19a danke ich für die freundschaftliche Atmosphäre und die stete gegenseitige Unterstützung. Besonders zu erwähnen sind hier alle Mitspieler unserer Kicker-Runde: Philipp Bauer, Filippo Cosi, Qi Li, Sindre Haugland, Alexander Lessig und alle anderen, die hin und wieder mal dabei waren.

Meiner Familie danke ich für den steten Rückhalt und die sinnstiftenden Gespräche. Besonders danken möchte ich meiner Frau Madeleine, für ihre bedingungslose Liebe, ihre aufbauenden Worte und ihre fortwährende Unterstützung.

Diese Arbeit wurde mit Unterstützung der Technischen Universität München, Institute for Advanced Study, gefördert durch die Exzellenzinitiative des Bundes und der Länder, und des Exzellenz-Clusters Nanosystems Initiative Munich (NIM), angefertigt.

Abstract

In this thesis, pattern formation in oscillatory media with a nonlinear global coupling is investigated. Predominant patterns are cluster states and so-called chimera states, i.e., the coexistence of synchronized and desynchronized regions. Two types of cluster states are found that give rise to two distinct chimera states. One of these types of cluster and chimera states reproduces experimental results. We perform a bifurcation analysis of the cluster states and identify the prerequisites for the chimera states.

Contents

Chapter 1

Introduction

An der Schwelle jeder wissenschaftlichen
Betrachtung der Welt steht die Verwunderung.
(Wilhelm Röpke)

In 1976, Robert M. May, a physicist and biologist, realized in a seminal article published in Nature [1] that knowing the complexity of dynamics a simple nonlinear equation can exhibit is of great importance to everyones life. As he wrote, focussing on linearized theories even in University courses, "ill equips the student to confront the bizarre behaviour exhibited by the simplest of discrete nonlinear systems" [1]. Solving a linear system can be done by breaking it into parts, and solving each part separately, like solving a partial differential equation in Fourier space for each Fourier mode uncoupled from the other modes. Recombination of all parts then yields the answer; thus, we can say that in a linear system the whole is equal to the sum of its parts. Incorporating a nonlinearity in the system leads to a dramatic change as the principle of superposition fails [2]. Considering a reaction-diffusion system the impact of this becomes obvious: Solving a system with a homogeneous dynamics consisting only of linear terms, yields spatial Fourier modes, which either grow or decay, nothing else can happen (except, of course, in the special case of neutral stability). In order to observe temporally stable patterns or even complex spatio-temporal behavior emerging, we need higher order terms to stabilize linearly unstable modes and, being at the heart of complex spatio-temporal behavior, higher order terms couple the spatial Fourier modes. We see that without nonlinearities life would not only be totally boring, it would not even be possible.

In fact, we need pattern formation at the very beginning of our existence in the process of morphogenesis. Out of nearly homogeneous tissue spatial patterns of tissue structures need to arise [3] to form shapes and functioning structures like organs. One possible mechanism capable of creating basic patterns is the so-called Turing mechanism, after Alan M. Turing, who described it already in 1952 [4]. A Turing pattern, i.e., a stripe- or spot-like pattern, arises when the diffusional coupling yields

an instability of the homogeneous state, which is counterintuitive as diffusion normally tends to homogenize a system. Further examples of pattern formation are given by observations of Lechleiter *et al.* in 1991, indicating that the intracellular milieu of *Xenopus laevis* oocytes behaves like a regenerative excitable medium [5]. They found the spontaneous emergence of plane and spiral calcium waves in stimulated oocytes.

But pattern formation is not resctricted to the early stages of life. In the heart muscle electrical turbulence can be observed [6, 7]. Spiral waves and their break-up could be observed in cardiac tissue and these phenomena could be explained from a solely dynamical point of view. Thus, for example, the spiral break-up is not triggered by inhomogeneities in the system, but rather arises via a dynamic instability. As a spiral wave in the electrical activity in the heart muscle is related to ventricular tachycardia and spiral turbulence to ventricular fibrillation [7], understanding these phenomena is the important first step in finding mechanisms to bring the heartbeat back to a normal rythm.

A study in this direction was performed by Garfinkel *et al.* who could successfully control chaotic cardiac arrythmia in rabbit hearts [8]. They could achieve this via a chaos control scheme that exploits the knowledge of chaotic systems and is not just a rude overwriting of the chaotic signal with a simple periodic stimulation. In fact, simple periodic stimulations failed in controlling the chaos.

Finally, the application of pattern formation and nonlinear dynamics to neural networks is important to understand neural function and disfunction [9]. We will come back to that point later, when considering the relation between unihemispherical sleep and so-called chimera states found in networks of oscillators.

All these examples immediately show that there is a need for model systems to study nonlinear dynamics in complex, pattern forming systems. Such a model system is the catalytic oxidation of carbon monoxide on a platinum surface in UHV [10] exhibiting a variety of patterns, like spiral waves, pulses, solitons, target patterns and turbulence. Another model system is the Belousov-Zhabotinsky reaction, which became a prototypical system for the study of spiral dynamics, but gives also rise to standing, irregular and localized clusters under global feedback [11, 12].

In this thesis we model the photoelectrodissolution of n-type silicon and demonstrate that it exhibits a wealth of spatio-temporal dynamics. It is a relatively easy-to-handle experiment, rendering it a convenient model system to study pattern formation. Patterns form in the thickness of an oxide-layer on the silicon working electrode, which can be spatially resolved in two dimensions. First experimental studies of this pattern formation have been published in 2009 by Miethe *et al.* [13]. In this article, the authors also proposed a generic model to simulate the dynamics, based on the fact that the basic oscillation arises via a Hopf bifurcation [14] (note that the detailed physical mechanism for the oscillation is still unresolved). Thus, they made their ansatz with a complex Ginzburg-Landau equation (CGLE), as this constitutes the normal form in the vicinity of a Hopf bifurcation for a reaction-diffusion system. Additionally, there is a second important feature in the experimental dynamics one has to capture with the model: for many parameter values the spatially averaged oxide-layer thickness exhibits a har-

monic oscillation with preserved amplitude and frequency. To account for this peculiar property, a nonlinear global coupling was introduced in the CGLE, yielding a modified complex Ginzburg-Landau equation (MCGLE). The resulting model, considered in one-dimensional space, already captured cluster dynamics very well [13, 15].

At this point, we start our investigation. Performing extensive simulations of the MCGLE, now in two spatial dimensions, we identify two hierarchies of symmetry-breaking dynamics. Starting from two types of cluster patterns, i.e., patterns consisting of different synchronized, but phase-shifted regions, for each type we find a transition to a so-called chimera state, with different qualitative features. In a chimera state, a system of identical oscillators, coupled identically and symmetrically, splits into two groups, one oscillating in synchrony, while the other group exhibits incoherent behavior. This phenomenon was first discussed by Kuramoto & Battogtokh in 2002 [16] and was named a chimera state in 2004 by Abrams & Strogatz [17], referring to the chimera in Greek mythology. In fact, such states have been observed earlier [18–20], without pointing out its importance. Subsequently, many theoretical investigations dealt with this topic, see for instance Refs. [21–30]. They could also be realized experimentally in chemical, optical, mechanical and electrochemical systems [29, 31–34]. For a recent review see Ref. [35].

It has long been thought that for the formation of chimera states a nonlocal coupling, i.e., a coupling with a coupling range between local and global, is indispensable. In this thesis we will question this assumption, since the nonlinear global coupling present in our system suggests that chimera states arise also under global coupling. Furthermore, a detailed comparison with the experimental dynamics is performed, aiming to proof the existence of chimera states in the experiments.

Despite the above mentioned work on chimera states, concerning the prerequisites of their existence and the mechanisms of their emergence only very little is known. Bifurcation analysis revealed that they can emerge via a saddle-node bifurcation [17, 23, 26, 36], and they were found in maps with coupling-induced bistability [27]. First analytical studies aiming to analyze the stability and to characterize the emergence and dynamics of chimera states in nonlocally coupled systems in a general way are presented in Refs. [36, 37]. In this thesis, we investigate if a clustering mechanism observed typically in globally coupled systems is a sufficient feature, rendering chimera states possible.

Chimera states might be of importance for some peculiar observations in different disciplines, such as the unihemispheric sleep of animals [38, 39], the need for synchronized bumps in otherwise chaotic neuronal networks for signal propagation [40] and the existence of turbulent-laminar patterns in a Couette flow [41]. In unihemispherical sleep, one half of the brain is sleeping (synchronized), while the other half is awake (desynchronized) and furthermore, the hemispheres interchange their state from time to time [38, 39, 42]. Up to now, this alternation phenomenon could only be reproduced in models of non-identical oscillators that are grouped a priori, with different intra- and inter-group coupling strengths, without external periodic forcing [43] and with forcing [44]. In contrast, we present alternating chimera states emerging spontaneously in an

isotropic medium and with symmetrical and identical coupling for all oscillators.

The thesis is organized as follows: In Chapter 2 we will briefly introduce the theoretical background, discuss the basic equations and outline the numerical methods used for the simulations. Then, we will introduce the experiment and the corresponding model, the MCGLE, in Chapter 3, discuss the spatio-temporal dynamics found and compare experiment and theory in detail. In order to analyze the patterns found in Chapter 3, we omit the diffusional coupling and investigate an ensemble of discrete oscillators with nonlinear global coupling in Chapter 4. Finally, we compare the results obtained with the discrete oscillators to the dynamcis in the MCGLE in Chapter 5 and sum up in Chapter 6.

Chapter 2

Background & Methods

In this chapter the dynamical equations underlying this work together with important analytical methods are introduced. We develop all necessary ideas step by step, but also as brief as possible.

2.1 Stuart-Landau equation

The first equation we introduce is the so-called Stuart-Landau equation. It constitutes the normal form for a system in the vicinity of a Hopf bifurcation, i.e., a system at the onset of oscillations. The Hopf bifurcation is the typically observed bifurcation leading to oscillations. Other bifurcations resulting in oscillations are the homoclinic bifurcation, the saddle-node of infinite period bifurcation and the saddle-node of periodic orbits bifurcation. As they are more complex, they occur in situations that are more involved. The center-manifold theorem [45] ensures that all systems in the vicinity of a given local bifurcation behave analogously. In a high dimensional system near a low-dimensional bifurcation like the Hopf bifurcation, this can be understood, when looking at the timescales of the different variables. Near a bifurcation most variables will evolve on a fast timescale, allowing their adiabatic elimination. A few slow variables will remain then, exhibiting the essential dynamics. Historically the name Stuart-Landau equation goes back to a paper by Landau in 1944 [46] and a paper by Stuart in 1960 [47]. Landau used an expansion in terms of an order parameter in order to describe the onset of turbulence in fluids and obtained the principal form of the Stuart-Landau equation. Stuart derived the Stuart-Landau equation via a perturbative method in the context of wave disturbances in flows.

We present now two variants to derive the Stuart-Landau equation, first via a reductive perturbation method following chapter 2 in Ref. [48] and second via symmetry considerations following Ref. [49]. The first variant enables one to derive appropriate parameters and also coupling functions for extended systems, once the underlying physical equations are known. However, the second variant underlines the importance of symmetries near bifurcations. We will discuss this point in more detail when moti-

vating a modified complex Ginzburg-Landau equation for an experimental system in Chapter 3.

2.1.1 Stuart-Landau equation via reductive perturbation method

The whole derivation follows chapter 2 in Ref. [48]. Consider a general dynamical system

$$\frac{\mathrm{d}\mathbf{X}}{\mathrm{d}t} = \mathbf{F}(\mathbf{X};\mu) \ , \quad i = 1,2,\dots,n \ ,$$

where $\mathbf{X}$ denotes, e.g., a vector of chemical concentrations for n different chemical species and μ is a parameter. We assume now that the steady state $\mathbf{X}_0$, i.e.,

$$\mathbf{F}((\mathbf{X}_0(\mu);\mu) = 0 \ ,$$

looses its stability for $\mu > 0$ via a Hopf bifurcation, giving rise to oscillations. Introducing a deviation $\mathbf{u} = \mathbf{X} - \mathbf{X}_0$, a Taylor expansion around the steady state reads

$$\frac{\mathrm{d}\mathbf{u}}{\mathrm{d}t} = L\mathbf{u} + M\mathbf{uu} + N\mathbf{uuu} + \dots \ . \tag{2.1}$$

The Jacobian matrix L has elements

$$L_{ij} = \frac{\partial F_i(\mathbf{X}_0)}{\partial X_{0j}} \ ,$$

and $M\mathbf{uu}$, $N\mathbf{uuu}$ are vectors with elements

$$(M\mathbf{uu})_i = \sum_{j,k} \frac{1}{2} \frac{\partial^2 F_i(\mathbf{X}_0)}{\partial X_{0j} \partial X_{0k}} u_j u_k \ , \quad (N\mathbf{uuu})_i = \sum_{j,k,l} \frac{1}{6} \frac{\partial^3 F_i(\mathbf{X}_0)}{\partial X_{0j} \partial X_{0k} \partial X_{0l}} u_j u_k u_l \ .$$

At first order, Eq. (2.1) leads to an eigenvalue problem

$$L\mathbf{u} = \lambda \mathbf{u} \ .$$

Eigenvalues λ determine the linear stability of the steady state $\mathbf{X}_0$. In case of a supercritical Hopf bifurcation, a complex conjugated pair of eigenvalues crosses the imaginary axis at $\mu = 0$ with

$$\left. \frac{\mathrm{dRe}(\lambda(\mu))}{\mathrm{d}\mu} \right|_{\mu=0} > 0 \ , \tag{2.2}$$

while all other eigenvalues are at a nonzero distance to the imaginary axis. Near the critical point $\mu = 0$, we can expand the Jacobian in terms of μ:

$$L = L_0 + \mu L_1 + \mu^2 L_2 + \dots \ ,$$

and analogously for the critical eigenvalues

$$\lambda = \lambda_0 + \mu\lambda_1 + \mu^2\lambda_2 + \dots \ .$$

The eigenvalues are complex numbers, i.e., $\lambda_\nu = \sigma_\nu + i\omega_\nu$. Since at the Hopf bifurcation a complex conjugated pair crosses the imaginary axis, we have $\sigma_0 = 0$ and because of Eq. (2.2) we have $\sigma_1 > 0$. Furthermore, we define $\mathbf{U}$ as the right eigenvector of L_0, corresponding to λ_0, i.e.,

$$L_0\mathbf{U} = \lambda_0\mathbf{U} \,.$$

The deviation $\mathbf{u}$ has to scale at first order like $\sqrt{|\mu|}$, conforming the Hopf-scaling. Thus, we introduce ε via $\varepsilon^2\chi = \mu$, where $\chi = \text{sign}\,(\mu)$. Then, $\varepsilon^2 = |\mu|$ and we can write

$$\mathbf{u} = \varepsilon\mathbf{u}_1 + \varepsilon^2\mathbf{u}_2 + \dots \,,$$

and

$$L = L_0 + \varepsilon^2\chi L_1 + \varepsilon^4 L_2 + \dots \,.$$

The critical eigenvalues λ have a small real part of $O\left(\varepsilon^2\right)$, giving rise to a small growth rate of the same order. Thus, it is convenient to introduce a slow timescale τ as $\tau = \varepsilon^2 t$. Then the temporal derivative in Eq. (2.1) becomes

$$\frac{\mathrm{d}}{\mathrm{d}t} = \frac{\partial}{\partial t} + \varepsilon^2\frac{\partial}{\partial\tau} \,.$$

Putting things together, see chapter 2 in Ref. [48], one obtains at first order

$$\mathbf{u}_1(t,\tau) = W(\tau)\mathbf{U}e^{i\omega_0 t} + \text{c.c.} \,, \tag{2.3}$$

where c.c. stands for the complex conjugate. A solvability condition yields for the dynamics of $W(\tau)$ on the slow timescale τ the Stuart-Landau equation

$$\frac{\partial W}{\partial\tau} = \chi\lambda_1 W - g\,|W|^2\,W \,. \tag{2.4}$$

Here g is a complex number $g = g_r + ig_i$. We can go to a description by means of amplitude and phase via $W = re^{i\phi}$, yielding

$$\begin{aligned}\frac{\partial r}{\partial\tau} &= \chi\sigma_1 r - g_r r^3 \,,\\ \frac{\partial\phi}{\partial\tau} &= \chi\omega_1 - g_i r^2 \,.\end{aligned}$$

In the supercritical case ($\chi > 0$) for $g_r > 0$ and in the subcritical case ($\chi < 0$) for $g_r < 0$, there exists a nontrivial solution, given by

$$\begin{aligned} r &= r_s \,, \quad \phi = \hat{\omega}\tau + \text{const.} \,,\\ r_s &= \sqrt{\frac{\sigma_1}{|g_r|}} \,, \quad \hat{\omega} = \chi\left(\omega_1 - g_i r_s^2\right) \,.\end{aligned}$$

This is a solution to the Stuart-Landau equation for W. To obtain the solution in terms of the original vector $\mathbf{X}$, one has to use Eq. (2.3) and obtains

$$\mathbf{X} \approx \mathbf{X}_0 + \varepsilon \mathbf{u}_1 = \mathbf{X}_0 + \varepsilon \left(\mathbf{U} r_s e^{i(\omega_0 + \varepsilon^2 \hat{\omega})t} + \text{c.c.} \right) ,$$

describing an elliptical oscillation of small amplitude.

As a last step, we will rescale Eq. (2.4) to get rid of dispensable parameters. In full length Eq. (2.4) reads

$$\frac{\partial W}{\partial \tau} = \chi \left(\sigma_1 + i\omega_1 \right) W - \left(g_r + i g_i \right) |W|^2 W .$$

By introducing $\tilde{\tau}$ and $\tilde{W}$ by

$$\tau = \frac{\tilde{\tau}}{\sigma_1} , \quad W = \sqrt{\frac{\sigma_1}{|g_r|}} \tilde{W} ,$$

we obtain

$$\frac{\partial \tilde{W}}{\partial \tilde{\tau}} = \chi \left(1 + i \frac{\omega_1}{\sigma_1} \right) \tilde{W} - \left(\frac{g_r}{|g_r|} + i \frac{g_i}{|g_r|} \right) \left| \tilde{W} \right|^2 \tilde{W} .$$

Under the assumption of a supercritical Hopf bifurcation, i.e., $\chi > 0$, and with $g_r > 0$ we obtain

$$\frac{\partial \tilde{W}}{\partial \tilde{\tau}} = \left(1 + i c_0 \right) \tilde{W} - \left(1 + i c_2 \right) \left| \tilde{W} \right|^2 \tilde{W} ,$$

where $c_0 = \omega_1 / \sigma_1$ and $c_2 = g_i / g_r$. Finally, we transform to a rotating frame by $\tilde{W} = \hat{W} \exp\left(i c_0 \tau \right)$, yielding

$$\frac{\partial \hat{W}}{\partial \tau} = \hat{W} - \left(1 + i c_2 \right) \left| \hat{W} \right|^2 \hat{W} .$$

Renaming $\hat{W} \to W$ and $\tau \to t$ gives the form of the Stuart-Landau equation, which we will use in this thesis:

$$\frac{\partial W}{\partial t} = W - \left(1 + i c_2 \right) |W|^2 W . \tag{2.5}$$

2.1.2 Stuart-Landau equation via symmetry considerations

Following Ref. [49] we will now briefly outline, how basic symmetry considerations are sufficient to conclude the principal form of the Stuart-Landau equation. Let us start with a harmonic oscillator,

$$\frac{\mathrm{d}W}{\mathrm{d}t} = i\omega_0 W . \tag{2.6}$$

The solution of this equation is a harmonic oscillation $W = \exp(i\omega_0 t)$ with frequency ω_0. Any oscillator, thus including the harmonic oscillator, is invariant with respect to an arbitrary phase shift χ, expressed as

$$W \to W e^{i\chi} .$$

The dynamical equations stay invariant under this transformation; it is in fact nothing else than a shift in time. In order to treat now a nonlinear oscillator, we have to find higher order corrections to the harmonic oscillation, Eq. (2.6), such that the resulting dynamical equation still possesses phase invariance:

$$\frac{\mathrm{d}W}{\mathrm{d}t} = i\omega_0 W + f\left(W, W^*\right) \ . \tag{2.7}$$

The asterisk denotes complex conjugation. We need $f\left(W, W^*\right)$ to satisfy

$$f\left(We^{i\chi}, W^* e^{-i\chi}\right) = f\left(W, W^*\right) e^{i\chi} \ ,$$

in order to keep Eq. (2.7) invariant with respect to phase shifts. Up to third order,

$$f\left(W, W^*\right) = \alpha_1 W + \alpha_2 \left|W\right|^2 W \ ,$$

fulfills the requirements, whereas all other second or third order terms would break the phase invariance. The parameters $\alpha_1 = \alpha_{1r} + i\alpha_{1i}$ and $\alpha_2 = \alpha_{2r} + i\alpha_{2i}$ are complex numbers. Finally, we obtain the principal form of the Stuart-Landau equation:

$$\frac{\mathrm{d}W}{\mathrm{d}t} = \left[\alpha_{1r} + i\left(\alpha_{1i} + \omega_0\right)\right] W + \left(\alpha_{2r} + i\alpha_{2i}\right) \left|W\right|^2 W \ .$$

2.2 Complex Ginzburg-Landau equation

In the previous section we introduced the basic oscillator, the so-called Stuart-Landau oscillator, constituting the normal form in the vicinity of a Hopf bifurcation. So far, this describes only single oscillators and extended systems that perform synchronized oscillations. To extend the scope of the model to spatially extended oscillatory media exhibiting spatio-temporal dynamics, we have to add a diffusional coupling to the system. This gives the picture of a medium, composed of local oscillators, interacting diffusively. Considering an oscillating chemical reaction for example, this is reasonable, as the oscillation will take place also, if we take a small part of the whole system and, as chemical species can spread via diffusion, these small parts are coupled diffusively.

In order to derive now a general description of oscillatory media close to a Hopf bifurcation, we again follow Kuramoto in Ref. [48]. We start with the general form of a reaction-diffusion system

$$\frac{\partial \mathbf{X}}{\partial t} = \mathbf{F}(\mathbf{X}) + D\nabla^2 \mathbf{X} \ .$$

If we consider now the stability of the uniform mode, we end up with an eigenvalue problem, depending on the wavenumbers of spatio-temporal modes. Thus, one obtains eigenvalues as for the Stuart-Landau oscillators, but every eigenvalue now forms a branch, parametrized by the wavenumbers of modes in the system. The situation we describe is that all eigenvalues are in the left half-plane up to $\mu = 0$ and a pair

of complex conjugated eigenvalues corresponding to the uniform mode crosses the imaginary axis at $\mu = 0$. Analogously to the situation of the discrete oscillator, the deviation $\mathbf{u}(\mathbf{r}, t) = \mathbf{X} - \mathbf{X}_0$ obeys

$$\frac{\partial \mathbf{u}}{\partial t} = \left(L + D\nabla^2\right)\mathbf{u} + M\mathbf{uu} + N\mathbf{uuu} + \dots ,$$

now including the diffusional coupling. As in the case of Stuart-Landau oscillators we have two timescales, t and the slow one τ. As we consider long wavelength modes, since they cross the imaginay axis next after the uniform mode, we introduce a slow space dependence $\mathbf{s} = \varepsilon\mathbf{r}$. This gives also rise to $\nabla \to \varepsilon\nabla_s$. Analogously to the derivation of the Stuart-Landau equation, we obtain

$$\mathbf{u}_1(t, \tau, \mathbf{s}) = W(\tau, \mathbf{s})\mathbf{U}e^{i\omega_0 t} + \text{c.c.} .$$

Finally, we obtain for $W(\tau, \mathbf{s})$ the complex Ginzburg-Landau equation (CGLE):

$$\frac{\partial W}{\partial \tau} = \chi\lambda_1 W + d\nabla_s^2 W - g\,|W|^2\,W .$$

d is a complex number, i.e., $d = d_r + id_i$, and g and λ_1 are the same as in the Stuart-Landau equation (2.4). We again rescale the equation using

$$\tau \to \sigma_1^{-1}\tau , \quad s \to \sqrt{\frac{d_r}{\sigma_1}}s , \quad W \to \sqrt{\frac{\sigma_1}{|g_r|}}W ,$$

which yields

$$\frac{\partial W}{\partial \tau} = (1 + ic_0)W + (1 + ic_1)\nabla_s^2 W - (1 + ic_2)\,|W|^2\,W ,$$

where

$$c_0 = \frac{\omega_1}{\sigma_1} , \quad c_1 = \frac{d_i}{d_r} , \quad c_2 = \frac{g_i}{g_r} ,$$

and we assumed a supercritical Hopf bifurcation and $g_r > 0$. As a last step, we go to a rotating frame and rename $\tau \to t$, $\mathbf{s} \to \mathbf{r}$, resulting in the form of the CGLE, which we will use throughout the thesis:

$$\frac{\partial W}{\partial t} = W + (1 + ic_1)\nabla^2 W - (1 + ic_2)\,|W|^2\,W . \tag{2.8}$$

In order to get an understanding of the influence of parameters c_1 and c_2 on the dynamics, we consider plane-wave solutions of the CGLE in a one-dimensional system. They read

$$W_Q(x, t) = R_Q e^{i(Qx - \omega_Q t)} ,$$

where

$$R_Q = \sqrt{1 - Q^2}\,,$$
$$\omega_Q = c_2 + (c_1 - c_2)Q^2\,,$$

and thus $|Q| < 1$. We can conclude that c_2 is the frequency of the uniform oscillation with $Q = 0$ and the difference $c_1 - c_2$ controls the nonlinear frequency-dispersion of non-uniform modes with $Q \neq 0$.

Historically, the CGLE has first been derived by Newell & Whitehead in 1969, when modelling the onset of instabilities in fluid convection [50]. In 1971, Stewartson & Stuart extended the Stuart-Landau equation derived by Stuart [47] to capture space and time dependence of instabilities in plane Poiseuille flow [51]. Also in 1971, DiPrima, Eckhaus and Segel derived the CGLE in the context of general hydrodynamic stability problems, where they performed a nonlinear analysis of disturbances to a basic flow [52]. In the 90's a lot of studies dealt with spatiotemporal pattern formation in the CGLE, see for example Refs. [53–64]. This list is far from being complete, but it shows already, how much interest in the CGLE was triggered, after Kuramoto & Tsuzuki derived it for reaction-diffusion systems [65, 66], albeit more than 15 years had to pass. Besides its applications to reaction-diffusion systems, the CGLE can be applied to second order phase transitions, superconductivity, superfluidity, Bose-Einstein condensation, liquid crystals, hyrdodynamics and optical systems. For reviews on this see Refs. [48, 49, 67–69].

Two limiting cases of the CGLE should also be mentioned. For $c_1, c_2 \to \infty$, the CGLE becomes the conservative nonlinear Schrödinger equation, i.e., a Hamiltonian system. The other limit is $c_1 = c_2 = 0$, yielding the real Ginzburg-Landau equation, which describes stationary periodic instabilities, see again Ref. [67].

The scope of the CGLE can even be extended, by considering more general coupling functions than the diffusional coupling, which constitutes a local, nearest-neighbor interaction. For example, in electrochemical systems [70, 71], as well as in multicomponent systems, where one fast diffusing species can be eliminated adiabatically [72], the range of coupling can be much larger, and one obtains a so-called nonlocal coupling. However, for a nonlocal coupling, the coupling strength still decreases with the distance and it has some finite range. Another type of coupling, so-called global coupling, does not decrease with the distance. In a system with solely global coupling, all individual oscillators or points experience the same coupling force. This can be realized for example in surface chemical reactions, where a rapid mixing in the gas phase takes place [73, 74] and thus, changes in the local dynamics at one point on the surface influence all other points on the surface nearly immediately. A CGLE with a general coupling function, encompassing the above mentioned examples, can be written as

$$\frac{\partial W}{\partial t} = W - (1 + ic_2)\,|W|^2\,W + (1 + ic_1)\int H\left(|x - x'|\right)\left[W(x') - W(x)\right]\mathrm{d}x'\,.$$

The function $H(|x - x'|)$ constitutes a general coupling function.

Typically, global couplings are linear functions of state variables, like simple linear averages. In this thesis, we go one step further and consider averages of nonlinear functions of state variables and thus, treat a nonlinear global coupling. This becomes necessary, when modelling the spatiotemporal dynamics in the oxide-layer thickness during the photoelectrodissolution of n-type silicon, as we will show in the next chapter.

2.3 Complex Ginzburg-Landau equation near a 2:1 resonance

In this section, we give a very brief description of the CGLE with external resonant forcing near a 2:1 resonance. More detailed information on this topic can be found in Refs. [49, 75, 76]. Let us consider an extended system undergoing a Hopf bifurcation with frequency Ω. The system is externally forced with a forcing frequency $\omega_f \approx 2\Omega$. Then, in the vicinity of the Hopf, we can write

$$u = u_0 + \left[A e^{i\omega t} + c.c. \right] + \dots ,$$

with $\omega := \omega_f/2$. For weak forcing, one obtains the forced CGLE as

$$\frac{\partial A}{\partial t} = (\mu + i\nu)A + (1 + ic_1)\nabla^2 A - (1 + ic_2)\,|A|^2 A + \gamma A^* . \tag{2.9}$$

μ describes the distance from the Hopf bifurcation and $\nu = \Omega - \omega_f/2$ is the so-called detuning, i.e., the difference between the natural frequency Ω and the resonance frequency $\omega_f/2$. γ denotes the forcing amplitude. The presence of the external forcing breaks the continuous phase invariance, which is present in the CGLE. In case of a 2:1 resonance, the invariance with respect to an arbitrary phase shift is reduced to the discrete symmetry $A \to e^{i\pi}A$. This is reflected in the occurrence of A^* in the forced CGLE.

Resonant solutions of Eq. (2.9) are given by stationary solutions $A = Re^{i\phi}$. Then, the original variable u behaves like

$$u = u_0 + \left[Re^{i\phi} e^{i\frac{\omega_f}{2}t} + c.c. \right] + \dots ,$$

which means that u oscillates at exactly half the forcing frequency, i.e., at $\omega_f/2$. Therefore, these solutions are called locked solutions. They arise in a pair of saddle-node bifurcations at $\gamma = \gamma_b$, where [76]

$$\gamma_b = \frac{\left|\nu - \mu c_2\right|}{\sqrt{1 + c_2^2}} ,$$

which changes for $\nu < \mu(c_2^2 - 1)/(2c_2)$ (for $c_2 > 0$) to [76]

$$\gamma_b = \frac{1}{2}\sqrt{\mu^2 + (\mu c_2 - 2\nu)^2} .$$

We see that the locked solutions exist inside a tongue-shaped region defined by $\gamma \geq \gamma_b$, which can be called the 2:1 resonance tongue.

2.4 Numerical Methods

2.4.1 Numerical solution of the modified complex Ginzburg-Landau equation

In this section, we will outline how the modified complex Ginzburg-Landau equation (MCGLE), used in Chapter 3 to study pattern formation, is solved numerically, as developed in Ref. [77]. The equation reads (cf. Eq. (3.4))

$$\partial_t W = W + (1 + ic_1)\nabla^2 W - (1 + ic_2)\,|W|^2\,W - (1 + i\nu)\,\langle W\rangle + (1 + ic_2)\left\langle |W|^2\,W\right\rangle . \quad (2.10)$$

Note that the nonlinear global coupling leads to a conserved mean-field oscillation, $\langle W\rangle = \eta \exp(-i\nu t)$, with amplitude η and frequency ν. In general we can say about Eq. (2.10) that its dynamics will exhibit several timescales due to the presence of the diffusional coupling and the nonlinear terms. Thinking in terms of spatial modes, the higher order modes will be damped on a very fast timescale, while the important dynamics are then exhibited by the slowly evolving lower order modes. This renders the problem stiff, as fast and slow timescales act together. Furthermore, the diffusional coupling suggests solving the system in Fourier space rather than with finite differences in real space, since the diffusion operator becomes diagonal in Fourier space and thus, the modes are decoupled. But the presence of the cubic term proportional to $|W|^2\,W$ renders the problem more complex, as it couples the Fourier modes. We will see that one can overcome this problem by using a so-called pseudospectral method. This means that the nonlinear terms are evaluated in real space and then transformed numerically to Fourier space, yielding decoupled equations in Fourier space. After the next timestep has been calculated in Fourier space, one transforms back to real space and evaluates the nonlinear term again, and so on.

The first step in solving the MCGLE is to expand W into a Fourier series,

$$W(x, y, t) = \sum_{n_x, n_y} W_{n_x n_y}(t) e^{i\mathbf{q}_{n_x n_y}\mathbf{r}} ,$$

with $\mathbf{q}_{n_x n_y} = \left(q_{n_x}, q_{n_y}\right)^T$ and $\mathbf{r} = (x, y)^T$. A typical experimental boundary condition is the no-flux boundary condition, describing an experiment performed in a closed cell without any incoming flow. Mathematically the no-flux boundary condition is expressed as

$$\left.\frac{\partial W(x, y, t)}{\partial x}\right|_{x=\pm L/2} = 0 , \quad \left.\frac{\partial W(x, y, t)}{\partial y}\right|_{y=\pm L/2} = 0 .$$

To find the allowed wavenumbers in case of no-flux boundary conditions, let us consider a one-dimensional system for simplicity. Then, we have

$$W(x,t) = \sum_n W_n(t) e^{iq_n x} ,$$

and the no-flux boundary conditions give

$$\begin{aligned} \left.\frac{\partial W}{\partial x}\right|_{x=\pm L/2} &= \sum_{n\neq 0} iq_n W_n(t) e^{iq_n x}\Big|_{x=\pm L/2} = 0 \\ &= \sum_{n>0} \left(iq_n W_n(t) e^{iq_n x} - iq_n W_{-n}(t) e^{-iq_n x} \right)\Big|_{x=\pm L/2} = 0 . \end{aligned}$$

The terms inside the parentheses have to vanish for each n separately:

$$\begin{aligned} & iq_n W_n(t) e^{iq_n x} - iq_n W_{-n}(t) e^{-iq_n x}\big|_{x=\pm L/2} = 0 \\ \rightarrow\ & W_n(t) e^{iq_n x} = W_{-n}(t) e^{-iq_n x}\big|_{x=\pm L/2} \\ & e^{\pm iq_n L} = \frac{W_{-n}(t)}{W_n(t)} . \end{aligned}$$

As the last equation has to hold for all times t, there are two cases:

$$\begin{aligned} &\text{(i) } W_{-n}(t) = W_n(t) \ \Rightarrow\ e^{\pm iq_n L} = 1 \ \Rightarrow\ q_n = \frac{2\pi n}{L} , n = 1,2,3,\dots , \\ &\text{(ii) } W_{-n}(t) = -W_n(t) \ \Rightarrow\ e^{\pm iq_n L} = -1 \ \Rightarrow\ q_n = \frac{\pi n}{L} , n = 1,3,5,\dots . \end{aligned}$$

Thus, the allowed wavenumbers are given by

$$q_n = \frac{\pi n}{L} , \ n = 0,1,2,3,\dots ,$$

with an additional condition on the mode amplitudes

$$W_n = (-1)^n W_{-n} .$$

With this result we can turn back to our two-dimensional system and the ansatz reads now

$$W(x,y,t) = \sum_{n_x,n_y} W_{n_x n_y}(t) e^{i\mathbf{q}_{n_x n_y}\mathbf{r}} , \ \mathbf{q}_{n_x n_y} = \left(\frac{n_x \pi}{L}, \frac{n_y \pi}{L} \right)^T , \tag{2.11}$$

where we used the allowed wavenumbers. In the next step, we have to find the conditions for the mode amplitudes $W_{n_x n_y}(t)$ in order to fulfill the boundary conditions.

In x-direction the no-flux conditions give

$$\left.\frac{\partial W(\mathbf{r},t)}{\partial x}\right|_{x=\pm L/2} = \sum_{n_x>0,n_y\geq 0}\Big[\frac{in_x\pi}{L}A_{n_xn_y}(t)e^{i(n_x\pi x+n_y\pi y)/L} - \frac{in_x\pi}{L}B_{n_xn_y}(t)e^{i(-n_x\pi x+n_y\pi y)/L} + \frac{in_x\pi}{L}C_{n_xn_y}(t)e^{i(n_x\pi x-n_y\pi y)/L} - \frac{in_x\pi}{L}D_{n_xn_y}(t)e^{i(-n_x\pi x-n_y\pi y)/L}\Big]\Big|_{x=\pm L/2} = 0\,.$$

As the latter equation has to hold independently of y, for every set n_x, n_y the A, B and the C, D terms have to vanish separately, yielding

$$\begin{aligned} &A_{n_xn_y}(t)e^{i(n_x\pi x+n_y\pi y)/L} - B_{n_xn_y}(t)e^{i(-n_x\pi x+n_y\pi y)/L}\big|_{x=\pm L/2} = 0 \\ &\Rightarrow A_{n_xn_y}(t)e^{\pm in_x\pi} = B_{n_xn_y}(t) \\ &\Rightarrow A_{n_xn_y}(t)(-1)^{n_x} = B_{n_xn_y}(t)\,. \end{aligned}$$

With the same consideration for C, D and for the no-flux condition in y-direction, one finally obtains the full conditions on the mode amplitudes:

$$\begin{aligned} A_{n_xn_y}(t)(-1)^{n_x} &= B_{n_xn_y}(t)\,, \\ A_{n_xn_y}(t)(-1)^{n_y} &= C_{n_xn_y}(t)\,, \\ A_{n_xn_y}(t)(-1)^{n_x+n_y} &= D_{n_xn_y}(t)\,. \end{aligned} \tag{2.12}$$

We see that it is sufficient to solve the equations for the A amplitudes only, as all other amplitudes are then predicted by the boundary conditions. Now, we insert our Fourier series, Eq. (2.11), into the MCGLE, Eq. (2.10). The exponential functions $\exp(i2\pi nx/L)$ are orthogonal with respect to an integration over $[-L/2, L/2]$. In our case the wavevectors read $q_n = n\pi/L = 2\pi n/2L$ and thus we have to integrate over $[-L, L]$. Exploiting this fact, we obtain

$$\begin{aligned} \frac{\partial W_{00}}{\partial t} &= -i\nu W_{00}\,, \\ \frac{\partial W_{n_xn_y}}{\partial t} &= W_{n_xn_y} - (1+ic_1)\left(q_{n_x}^2 + q_{n_y}^2\right)W_{n_xn_y} - (1+ic_2)G_{n_xn_y}\,, \quad |n_x|+|n_y|\neq 0\,, \end{aligned} \tag{2.13}$$

where

$$|W|^2 W = \sum_{n_x,n_y} G_{n_xn_y}(t)e^{i\mathbf{q}_{n_xn_y}\mathbf{r}}\,.$$

For a one-dimensional system with periodic boundary conditions, $|W|^2 W$ gives in Fourier space $\sum_{n=j-k+l} W_j W_k^* W_l$. Thus, this cubic term couples the modes in Fourier space. We solve the equations by using a pseudospectral method: we Fourier transform the term $|W|^2 W$ numerically, yielding $G_{n_xn_y}$, resulting in an uncoupled system of ordinary differential equations in Fourier space (note that the coupling is hidden in $G_{n_xn_y}$). We solve this system as described below, transform back to real space and evaluate $|W|^2 W$ in real space. Then, we can again calculate $G_{n_xn_y}$, and so on.

But before solving the equations in Fourier space now, we have to clarify, how to calculate the Fourier modes with $q_n = \pi n/L$. The standard Fast Fourier Transform (FFT) uses $q_n = 2\pi n/L$. To use the FFT nevertheless, we incorporate a trick

$$q_n = \frac{\pi n}{L} = \frac{2\pi n}{2L} \equiv \frac{2\pi n}{L'} ,$$

where $L' = 2L$. This means, the modes with $q_n = \pi n/L$ on the domain $[-L/2, L/2]$ are modes with $q_n = 2\pi n/L'$ on the domain $[-L'/2, L'/2] = [-L, L]$. Thus, we simulate a system of size $L' = 2L$ and enforce the no-flux boundary conditions at $\pm L/2 = \pm L'/4$ with the conditions on the mode amplitudes in Eq. (2.12). At the end of the simulation, we omit the part of the system lying outside the no-flux boundaries. In this way, we can make use of the computationally fast FFT.

Finally, we can solve the system of ordinary differential equations (ODEs) in Eqs. (2.13) using a technique called exponential time stepping [78]. In order to understand how this method works, we follow Ref. [78] and consider a general ODE

$$\frac{\mathrm{d}u}{\mathrm{d}t} = cu + F(u, t) ,$$

where c is a constant and $F(u, t)$ contains nonlinear and forcing terms. The exact solution of the above equation is given by

$$u(t_n + h) = u(t_n)e^{ch} + e^{ch} \int_0^h e^{-c\tau} F\left(u(t_n + \tau), t_n + \tau\right) \mathrm{d}\tau . \tag{2.14}$$

Let us write

$$u(t_n) = u_n \ , \ u(t_n + h) = u_{n+1} \ , \ F(u(t_n), t_n) = F_n .$$

The idea of the method is now to approximate the function F under the integral and here we use the approximation linear in the timestep h:

$$F(u(t_n + \tau), t_n + \tau) \simeq F_n + \frac{F_n - F_{n-1}}{h}\tau + O(h^2) .$$

Insertion of this approximation into Eq. (2.14) yields the formula for the exponential time stepping [78]:

$$u_{n+1} = u_n e^{ch} + F_n \frac{(1 + hc)e^{ch} - 1 - 2hc}{hc^2} + F_{n-1} \frac{1 + hc - e^{ch}}{hc^2} . \tag{2.15}$$

Thus, we can identify the constant c and the nonlinearity F in Eqs. (2.13) as:

(i) homogeneous mode: $c_{00} = -iv \ , \ F_{00} = 0 \ ,$

(ii) other modes: $c_{n_x n_y} = 1 - (1 + ic_1)\left(q_{n_x}^2 + q_{n_y}^2\right) \ , \ F_{n_x n_y} = -(1 + ic_2)G_{n_x n_y} .$

Finally, we want to consider the homogeneous mode with $F_{00} = 0$. In this case, the formula in Eq. (2.15) yields

$$u_{n+1} = u_n e^{c_{00}h} .$$

Rewriting this as

$$u(t_n + h) = u(t_n) e^{c_{00}h} ,$$

we see that the numerical solution for the homogeneous mode is exact. This is clear, as the only approximation that has been introduced, was for the function F.

For the results presented in this thesis, we simulated the MCGLE mostly with 512x512 Fourier modes, used a computational timestep of $\Delta t = 0.05$ and initialized the system with a two-dimensional circular perturbation (proportional to $1/cosh(\cdot)$) and additional noise. Note that the amplitude of the spatial average $|\langle W \rangle|$ is the parameter η, which is conserved. The initial conditions are set appropriately.

2.4.2 Numerical solution of the Stuart-Landau ensemble with nonlinear global coupling

The system of Stuart-Landau oscillators with nonlinear global coupling employed in Chapter 4 and given in Eqs. (4.1) reads

$$\frac{\mathrm{d}}{\mathrm{d}t} W_k = W_k - (1 + ic_2) |W_k|^2 W_k - (1 + iv) \langle W \rangle + (1 + ic_2) \left\langle |W|^2 W \right\rangle , \quad k = 1, 2, \ldots, N \tag{2.16}$$

Here $\langle \cdots \rangle$ describes the arithmetic mean over the oscillator population, i.e., $\langle W \rangle = \sum_{k=1}^{N} W_k / N$. Taking the average of the whole equation yields for the dynamics of the mean value

$$\frac{\mathrm{d}}{\mathrm{d}t} \langle W \rangle = -iv \langle W \rangle \quad \Rightarrow \quad \langle W \rangle = \eta e^{-ivt} .$$

We solved Eqs. (2.16) using the scipy.integrate.ode() class of `SciPy` for `Python` and chose the implicit Adams method with a timestep of $dt = 0.01$. Initial conditions are random numbers on the real axis fulfilling the conservation law for the mean-field.

Chapter 3

Pattern formation in a complex Ginzburg-Landau equation with nonlinear global coupling

The ability to reduce everything to simple fundamental laws does not imply the ability to start from those laws and reconstruct the universe. [...] The constructionist hypothesis breaks down when confronted with the twin difficulties of scale and complexity. The behavior of large and complex aggregates of elementary particles, it turns out, is not to be understood in terms of a simple extrapolation of the properties of a few particles. Instead, at each level of complexity entirely new properties appear, and the understanding of the new behaviors requires research which I think is as fundamental in its nature as any other.

(Philip W. Anderson)

In this chapter, we introduce the experimental system in detail. Subsequently, we derive the modified complex Ginzburg-Landau equation to model the experiment. After presenting spatio-temporal patterns in the model and comparing them to the experiment, we will discuss the findings and conclusions. The experiments have been conducted and analyzed by Konrad Schönleber and co-workers. Part of the results presented in this chapter can be found in common publications [79, 80].

3.1 Experimental background: the photoelectrodissolution of n-type silicon

During the potentiostatic photoelectrodissolution of n-type silicon under high anodic voltage and in the presence of a flouride containing electrolyte, two competing processes take place. Due to the applied potential, an electrochem-

ical oxidation of the silicon creates an silicon oxide layer on the silicon electrode. The flouride species present in the electrolyte consequently etch this oxide layer back, leading to a competition of oxide growth and shrinkage. The electrochemical equations for these processes read:

$$\begin{aligned} \mathrm{Si} + 4\mathrm{H_2O} + \nu_{\mathrm{VB}}\mathrm{h}^+ &\rightarrow \mathrm{Si(OH)_4} + 4\mathrm{H}^+ + (4 - \nu_{\mathrm{VB}})\mathrm{e}^- \\ \mathrm{Si(OH)_4} &\rightarrow \mathrm{SiO_2} + 2\mathrm{H_2O} \end{aligned} \tag{3.1}$$

for the formation of silicon oxide (SiO_2) [81, 82] and

$$\mathrm{SiO_2} + 6\mathrm{HF} \rightarrow \mathrm{SiF_6^{2-}} + 2\mathrm{H}^+ + 2\mathrm{H_2O} \tag{3.2}$$

describing the etching of SiO_2 to SiF_6^{2-}, protons and water [83]. Also other flouride species present in the electrolyte like HF_2^- lead to an etching of the silicon oxide. In Eqs. (3.1) ν_{VB} is the number of charge carriers from the valence band involved in the oxidation reaction. The initial charge transfer of the electrochemical oxidation occurs by the capture of a hole from the valence band resulting in $\nu_{VB} \geq 1$ [84]. In case of p-type silicon these holes are always present, while in n-type silicon, which we consider here, they have to be generated via illumination. Thus, we can already identify parameters important for the reactions occurring. The oxidation and thus the creation of an oxide layer is driven by the potential and needs illumination. The total etch rate depends on the pH-value and the flourine concentration c_F and might also be influenced by the potential.

By adjusting the parameters, besides a steady state, the system can become oscillatory, which was described in the 1950s. A review on this topic can be found in chapter 5 in Ref. [85]. Despite the potentiostatic control, the oscillations are expressed in an oscillating current, accompanied by oscillations of the oxide-layer thickness with an amplitude in the nm-range [86–90]. We will now briefly present the experimental setup and subsequently discuss the oscillations in more detail.

3.1.1 Experimental setup

A sketch of the experimental setup is depicted in Fig. 3.1. The electrochemical cell consists of three electrodes: reference, working and counter electrode. They are immersed in electrolyte, potentiostatically controlled and there is an external resistance in series with the working electrode (the relevance of this resistance will be discussed below). The sample is illuminated with a laser (dashed line) through the circular counter electrode. In order to obtain and keep uniform conditions at the whole working-electrode surface, the electrolyte is stirred continuously and the counter electrode is placed symmetrically opposite the working electrode.

To investigate the spatial distribution of the oxide-layer thickness, a LED light beam (dashed-dotted line) is reflected from the silicon-electrode surface. Due to reflection the elliptical polarization of the light beam is changed in dependence on the local oxide-layer thickness. Via an optical setup these polarization changes are converted

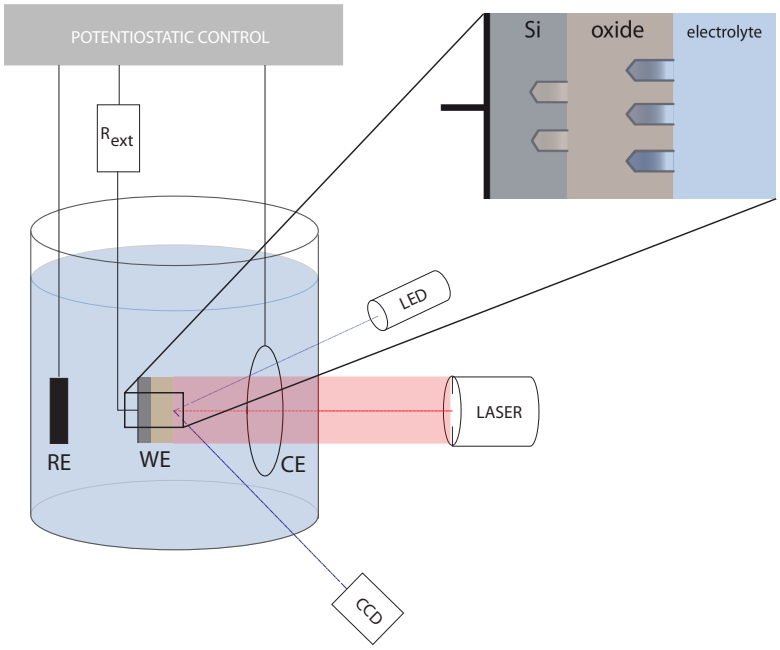

Figure 3.1: Sketch of the experimental setup. RE, WE and CE denote reference, working and counter electrode, respectively. The laser illuminates the silicon sample and the LED is used for the ellipsometric imaging. Images are recorded with the CCD camera. In the top right corner the oxide layer between the silicon on the left and the electrolyte on the right is shown, together with the growth and shrinkage directions. *Taken from Ref. [91] (doi:10.1088/1367-2630/16/6/063024).*

into intensity changes, which are finally measured with a CCD camera, yielding a two-dimensional image of the oxide-layer thickness. This imaging technique is called spatially resolved ellipsometric imaging and was first established by Rotermund *et al.* [92]. For more details on the experimental setup see Ref. [79].

3.1.2 Homogeneous dynamics of the oxide-layer thickness

As already mentioned, for suitable experimental parameters the potentiostatic electrodissolution of n-type silicon can take place in an oscillatory fashion. This oscillation was first observed in 1958 for p-type silicon [81], where no illumination is needed. It can be shown that in this case an external resistor in series with the working electrode is indispensable for the oscillations to be stable [93]. Here, we consider n-type silicon necessitating illumination. For high illumination intensities, the dynamical behavior of n-type silicon becomes equivalent to the one of p-type silicon [91, 94], as then always enough holes as charge carriers are present. For n-type silicon in case

of illumination-limited total current oscillations are also possible without an external resistance. However, the resistance is an important experimental parameter, as it provides a linear global coupling [95], since for a given potential the total current is controlled.

A particular example of uniform oscillations for n-type silicon is depicted in Fig. 3.2. In Fig. 3.2a the oscillations of the spatially averaged relative oxide-layer thickness ξ (top) and of the current density j (bottom) are shown. Figure 3.2b presents the spatially resolved oxide-layer thickness in two snaphots and in a one-dimensional cut versus time, demonstrating that the whole electrode is oscillating in synchrony.

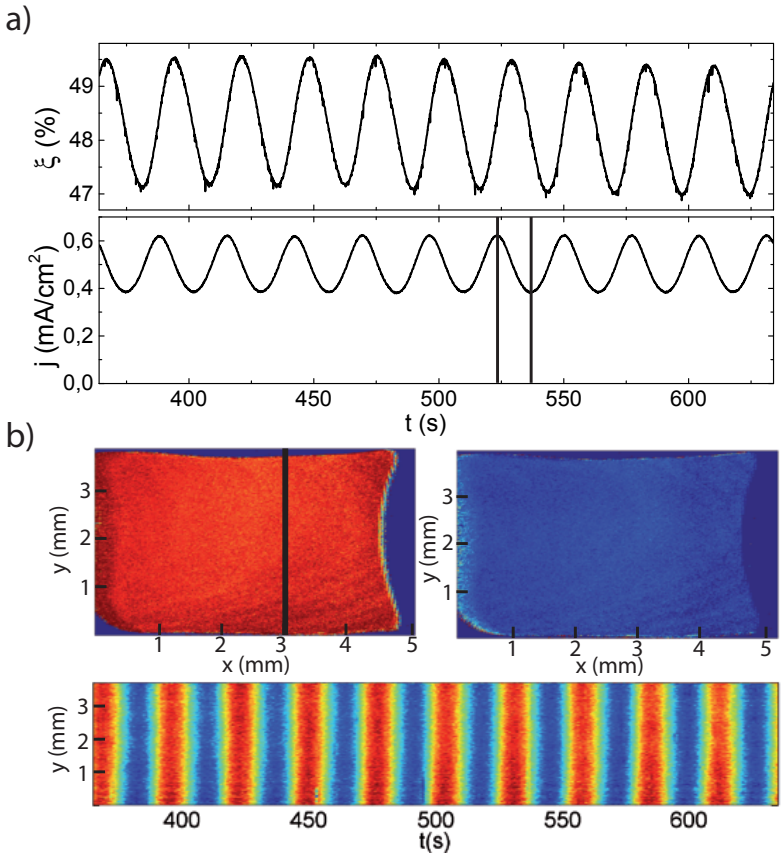

Figure 3.2: Uniform oscillation of oxide-layer thickness ξ and current density j at a high illumination intensity and under constant potential for n-type silicon. Parameters read: c_F = 50 mM, pH = 2.3, $R_{ext}A$ = 2.7 kΩcm^2, I_{ill} = 3.0 mW/cm^2 and U = 8.65 V vs. SHE. (a) Oscillations of spatially averaged oxide-layer thickness ξ (top) and current density j (bottom). (b) Spatially resolved oxide-layer thickness in two snapshots at consecutive maxima of j (indicated by vertical lines in (a)) and a one-dimensional cut along the vertical line in the left snapshot versus time. The intensity information recorded with the CCD camera is expressed in the color coding. As obvious from the figures, the oscillation occurs in a synchronized and thus uniform manner. *Taken from Ref. [80].*

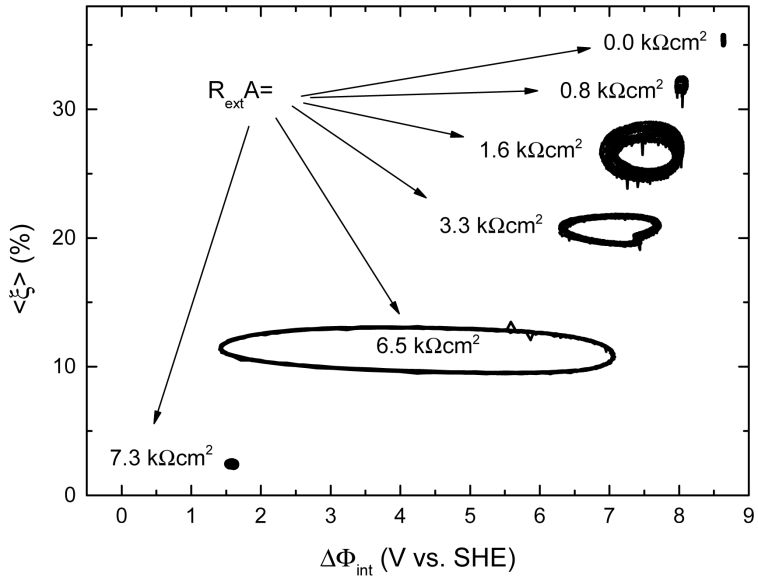

Figure 3.3: Hopf bifurcation in case of highly illuminated n-type silicon for increasing external resistance R_{ext} shown in the phase space of the mean oxide-layer thickness $\langle\xi\rangle$ vs. the potential drop over the interface $\Delta\Phi_{int}$. Other parameters are kept constant to pH = 1, c_F = 75 mM and U = 8.65 V vs. SHE. *Taken from Ref. [80].*

Increasing the external resistance starting from $R_{ext} = 0$ for otherwise constant parameters, reveals that uniform oscillations arise in a Hopf bifurcation [96]. In Fig. 3.3 the resultant growth of the limit cycle is shown in the phase space. At high coupling strength, i.e., at high R_{ext}, the limit cycle breaks down, since then no stable oxide can be formed anymore.

So far, we considered n-type silicon with high illumination intensity, whereby high means that always enough charge carriers are present for the electrooxidation to occur. A second global coupling, in addition to the linear global coupling via the external resistance, can now be realized by reducing the illumination intensity. This limits the total current through the electrode by limiting the available amount of charge carriers. The example in Fig. 3.4 demonstrates the nonlinear effect on the current, while the mean oxide-layer thickness performs nearly harmonic oscillations nonetheless. Due to the effect on the current, the dynamics experience a nonlinear global coupling, which is weak for high illumination intensities and strong for low intensities. Note that the full mechanism how the nonlinear coupling arises and how it could be expressed as a mathematical coupling function is not completely clear yet. The description given here displays our current understanding. The nonlinear global coupling renders stable uniform oscillations without external resistance possible. They are also created in a Hopf bifurcation when varying the illumination intensity, as demonstrated in Fig. 3.5. In this case, the limit cycle shrinks again, when the illumination intensity drops below a certain intermediate value. This suggests another Hopf bifurcation, when coming

from low illumination intensities.

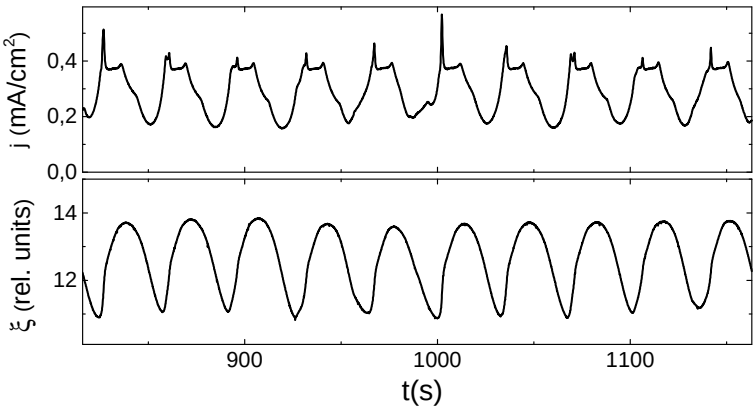

Figure 3.4: Example for the effect of a limited illumination of n-type silicon on the total current and on the mean oxide-layer thickness. The current (top) is effected nonlinearly, while the mean oxide-layer thickness (bottom) performs a still nearly harmonic oscillation, cf. Fig. 3.2. *Taken from Ref. [91] (doi:10.1088/1367-2630/16/6/063024).*

Combining both coupling mechanisms, linear and nonlinear global couplings, renders the formation of spatio-temporal patterns in the oxide-layer thickness possible. In Fig. 3.6 a phase diagram is presented. Pattern formation can be observed for strong nonlinear global coupling, i.e., low illumination intensity, and weak linear global coupling, i.e., small R_{ext}.

The spatio-temporal pattern formation can be monitored and investigated via the ellipsometric imaging technique explained above. Astonishingly, for a huge parameter region, the spatially averaged oxide-layer thickness exhibits persistent and nearly harmonic oscillations, in a way as shown in Fig. 3.2a, despite the formation of patterns in the oxide-layer thickness. In other regions of parameter space, these mean-field oscillations might exhibit two different frequencies or be irregular as well [91]. However, in this thesis we restrict on the case of nearly harmonic mean-field oscillations.

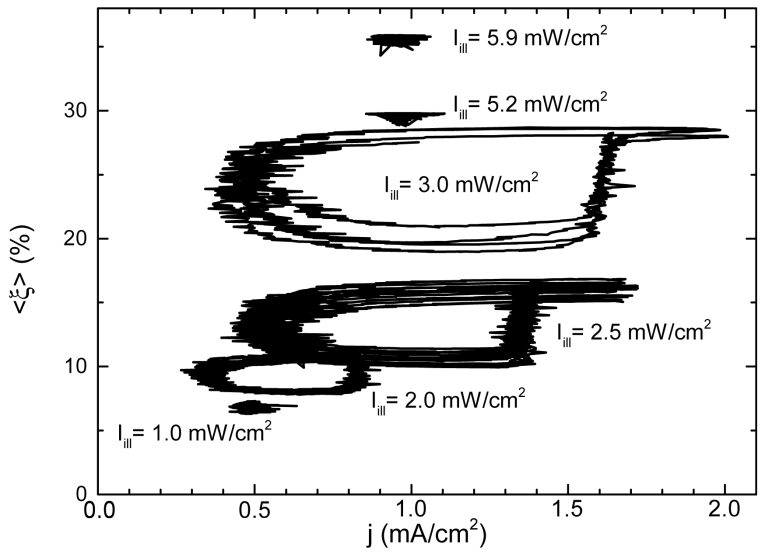

Figure 3.5: Hopf bifurcation in case of n-type silicon without external resistance for varying illumination intensity and otherwise fixed parameters pH = 1 and c_F = 75 mM. *Taken from Ref. [80].*

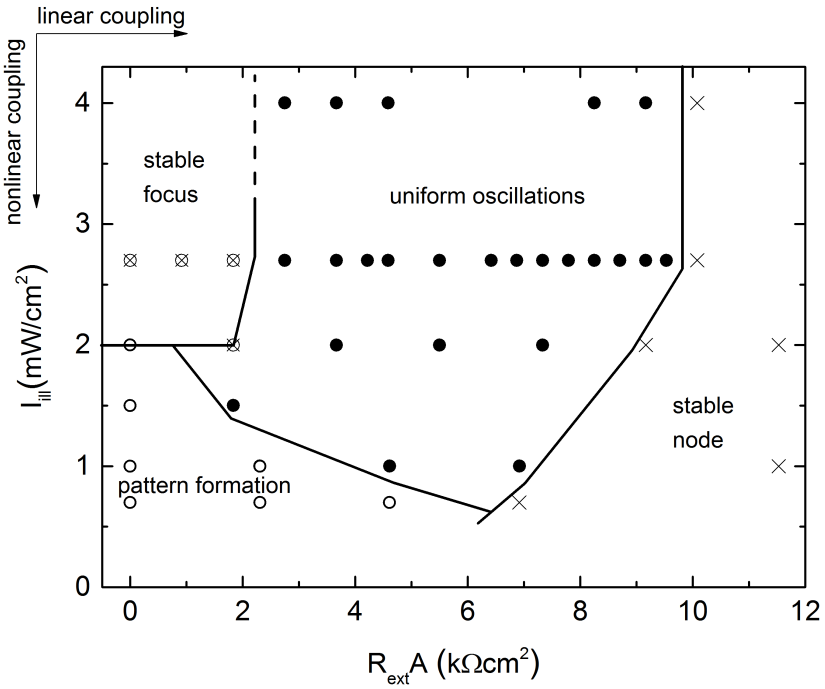

Figure 3.6: Phase diagram: nonlinear global coupling vs. linear global coupling. The strength of the nonlinear global coupling is measured in terms of the illumination intensity I_{ill}, while the strength of the linear global coupling is given by $R_{ext}A$. Other parameters read: c_F = 50 mM and pH = 2.3. *Taken from Ref. [91] (doi:10.1088/1367-2630/16/6/063024).*

An overview of the main patterns, relevant to this thesis, is presented in Fig. 3.7. Shown are two-dimensional snapshots of the oxide-layer thickness, visualized with colors, and one-dimensional spatio-temporal cross sections. In Figs. 3.7a and b the modulated amplitude cluster state is depicted. Consecutive snapshots demonstrate that the system is split into two phases that oscillate in anti-phase. However, as the one-dimensional cut in Fig. 3.7b reveals, these anti-phase oscillations are more complex than one would expect from simple two-phase clusters. There is a strong uniform oscillation present, which is modulated by two-phase clusters. These two-phase clusters are oscillating at half the frequency of the uniform oscillation. This type of clustering has also been termed type II clusters [13, 15, 97].

The modulated amplitude cluster state undergoes a symmetry-breaking transition. We will discuss this transition in detail below, when considering the theoretical results. Here, we give a brief description of the resulting states. The first symmetry-broken state one finds, coming from the modulated amplitude cluster state, is what we call subclustering and the dynamics of it are depicted in Figs. 3.7c and d. The snapshots and the one-dimensional cut demonstrate that the system now splits into a homogeneously oscillating region and a region exhibiting two-phase clusters. These two-phase subclusters oscillate at half the frequency of the homogeneous oscillation.

Changing parameters further one finds a more dramatic kind of symmetry-breaking. In the state presented in Figs 3.7e and f, we observe a homogeneously oscillating region coexisting with a region exhibiting incoherent and turbulent dynamics. Thus, this state is an experimental realization of a chimera state.

An appropriate model has to reproduce the special type of clustering and the symmetry-breaking dynamics. In the next section we will outline how this is achieved with a general ansatz describing a system in the vicinity of a Hopf bifurcation. Subsequently, the spatio-temporal patterns found in simulations of this model are analyzed and then compared to the patterns found in the experiments.

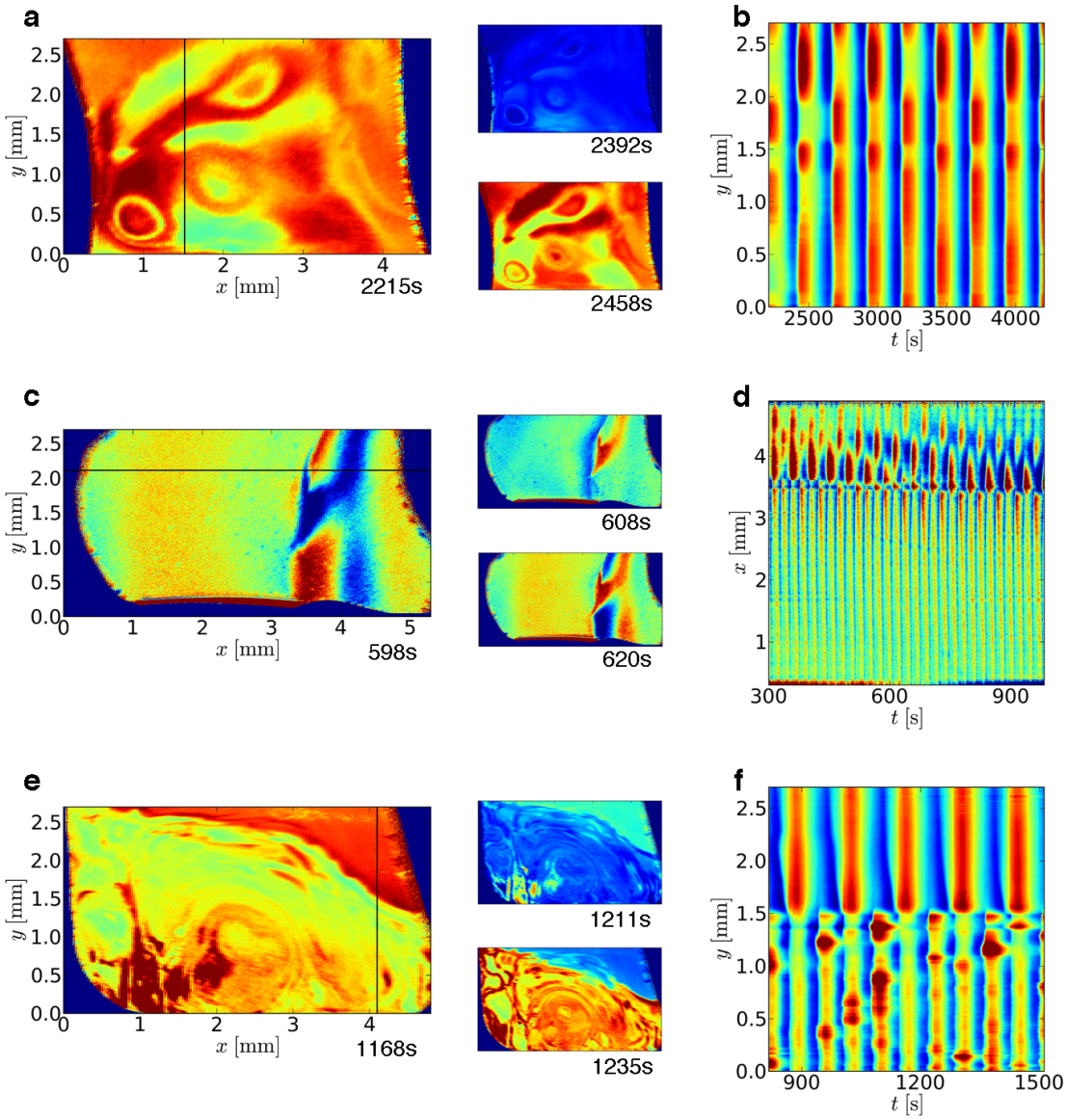

Figure 3.7: Spatio-temporal evolution of the oxide-layer thickness during the photoelectrodissolution of silicon: modulated amplitude clusters, subclustering and chimera state. Shown are snapshots and one-dimensional cuts versus time, colors indicate the thickness of the oxide layer, x and y represent spatial coordinates and t denotes time. (**a,b**) Modulated amplitude cluster state, where two intermixed regions oscillate each uniformly with a phase difference to the respective other one. (**c,d**) The oxide-layer thickness exhibits subclustering: a stripe of two-phase clusters is embedded in an otherwise uniformly oscillating background. The clusters in the stripe oscillate at half the frequency of the background oscillation. (**e,f**) Chimera state: the coexistence of synchrony (domain in upper right corner) and asynchrony is apparent. Parameters read: c_F = 35 mM, pH = 1, A = 22.73 mm^2, R_{ext} = 40 kΩ, $I \simeq$ 0.7 mW/cm^2 (modulated amplitude cluster, a and b), c_F = 50 mM, pH = 2.3, A = 23.06 mm^2, R_{ext} = 0 Ω, $I \simeq$ 1 mW/cm^2 (subclustering, c and d) and c_F = 50 mM, pH = 3, A = 22.42 mm^2, R_{ext} = 0 Ω, $I \simeq$ 0.5 mW/cm^2 (chimera, e and f).

3.2 Theoretical modelling of experiments

The experimental system presented in the preceding section can be modelled in a very general way. This will be summarized in what follows. From Section 3.3 on, results obtained in the framework of this thesis are discussed.

At high illumination intensities we observe homogeneous oscillations over the entire electrode surface. These oscillations originate in a Hopf bifurcation as described above. Thus, in order to model this system, the appropriate normal form to start with is the complex Ginzburg-Landau equation (CGLE) [48, 49, 67] for a complex order parameter $W(\mathbf{x}, t)$

$$\partial_t W = W + (1 + ic_1)\nabla^2 W - (1 + ic_2)\,|W|^2\, W\,. \tag{3.3}$$

This equation describes all reaction-diffusion equations in the vicinity of a supercritical Hopf bifurcation. For more details and a derivation see Chapter 2. Equation (3.3) admits plane wave solutions of wavenumber Q

$$W_Q = R_Q \exp\left[i(\omega_Q t + Qx)\right]\,,$$

with $\left|R_Q\right|^2 = 1 - Q^2$ and $\omega_Q = -c_2 + (c_2 - c_1)Q^2$ [48, 49]. A general solution is then given as a combination of these plane waves. This, in general, results in dynamics with an unpreserved homogeneous mode $W_0 = \langle W \rangle$. In contrast, for a huge parameter space the silicon system exhibits conserved harmonic oscillations in the averaged oxide-layer thickness. To achieve this in the model, the CGLE is extended in a straightforward way by introducing a nonlinear global coupling into Eq. (3.3), leading to a modified complex Ginzburg-Landau equation (MCGLE) [13, 15]

$$\partial_t W = W + (1 + ic_1)\nabla^2 W - (1 + ic_2)\,|W|^2\, W - (1 + iv)\,\langle W \rangle + (1 + ic_2)\left\langle |W|^2\, W \right\rangle\,. \tag{3.4}$$

Since we model a two-dimensional system, the complex order parameter $W(\mathbf{r}, t)$ is a function of the position vector $\mathbf{r} = (x, y)^T$ and time t. Angular brackets $\langle \cdots \rangle$ denote the spatial average. As briefly outlined in Chapter 2, linear global couplings have been already studied and there exist general ways in which in an experimental system a linear global coupling arises. New is the introduction of the nonlinear global-coupling term proportional to $\left\langle |W|^2\, W \right\rangle$, becoming necessary due to the coupling induced by the limitation of illumination. The total coupling is designed in such a way that, when taking the spatial average of the whole equation, Eq. (3.4), one obtains

$$\partial_t \langle W \rangle = -iv\,\langle W \rangle\,, \tag{3.5}$$

which results in conserved harmonic oscillations of the spatial average,

$$\langle W \rangle = W_0 = \eta \exp\left[-i(vt + \phi_0)\right]\,, \tag{3.6}$$

with amplitude η and frequency ν. ϕ_0 is an arbitrary initial phase. The essential dynamical properties of the silicon system are thus met with Eq. (3.4): oscillations arising through a Hopf bifurcation and the conserved harmonic mean-field oscillation. In Section 3.5 we show that this general ansatz indeed captures the pattern dynamics found in the experiments. But before, we calculate the linear stability of the uniform oscillation in the next section. This enables us to choose a suitable parameter region in order to observe pattern formation.

3.2.1 Linear stability analysis

For the linear stability analysis of the MCGLE, Eq. (3.4), we write $W = W_0(1+w)$, where w is a general inhomogeneity and W_0 is the homogeneous mode [15],

$$W_0 = \eta e^{-i\nu t} \,. \tag{3.7}$$

Inserting this ansatz into the MCGLE, one finds for the several parts

$$\begin{aligned}
\partial_t W &= -i\nu W_0 + W_0 \partial_t w - i w \nu W_0 \\
\nabla^2 W &= W_0 \nabla^2 w \\
|W|^2 W &= |W_0|^2 W_0 \left(1 + 2w + w^* + 2|w|^2 + w^2 + |w|^2 w\right) \\
\langle W \rangle &= W_0 \\
\left\langle |W|^2 W \right\rangle &= |W_0|^2 W_0 \left\langle 1 + 2|w|^2 + w^2 + |w|^2 w \right\rangle \,.
\end{aligned}$$

Putting everything together, one obtains

$$\begin{aligned}
W_0 \partial_t w - i\nu w W_0 = {} & W_0 w + (1 + ic_1) W_0 \nabla^2 w \\
& - (1 + ic_2) |W_0|^2 W_0 \left(1 + 2w + w^* + 2|w|^2 + w^2 + |w|^2 w\right) \\
& + (1 + ic_2) |W_0|^2 W_0 \left\langle 1 + 2|w|^2 + w^2 + |w|^2 w \right\rangle \,.
\end{aligned}$$

Division by W_0 and rearranging terms yields for w,

$$\begin{aligned}
\partial_t w = {} & \left(1 + i\nu - 2(1 + ic_2)\eta^2\right) w + (1 + ic_1)\nabla^2 w \\
& - (1 + ic_2)\eta^2 \left(|w|^2 w + w^*\right) + A \,,
\end{aligned}$$

where we defined

$$A = -(1 + ic_2)\eta^2 \left[\left(2|w|^2 + w^2\right) - \left\langle 2|w|^2 + w^2 + |w|^2 w \right\rangle\right] \,.$$

We further introduce

$$a = 1 + i\nu - 2(1 + ic_2)\eta^2 \tag{3.8}$$

and, since we are interested in the linear stability of the system, we neglect nonlinear terms. Thus, we obtain

$$\partial_t w = a w + (1 + ic_1)\nabla^2 w - (1 + ic_2)\eta^2 w^* \,. \tag{3.9}$$

Expanding the complex amplitude w into a Fourier series under the assumption of no-flux boundary conditions at the ends of the domain and, for convenience, considering a one-dimensional system, we have

$$w = \sum_{n\neq 0} w_n e^{iq_n x}\,, \quad q_n = \frac{\pi n}{L}$$
$$w_n = (-1)^n w_{-n}\,.$$

Insertion into Eq. (3.9) yields for the Fourier amplitudes w_n

$$\partial_t w_n = w_n - (1+ic_1)q_n^2 w_n - (1+ic_2)\eta^2(-1)^n w_n^*\,.$$

For w_n and w_n^* one finally obtains

$$\partial_t \begin{pmatrix} w_n \\ w_n^* \end{pmatrix} = \underbrace{\begin{pmatrix} a-(1+ic_1)q_n^2 & -(1+ic_2)\eta^2(-1)^n \\ -(1-ic_2)\eta^2(-1)^n & a^*-(1-ic_1)q_n^2 \end{pmatrix}}_{=:J} \begin{pmatrix} w_n \\ w_n^* \end{pmatrix}\,.$$

The trace τ and the determinant Δ of the matrix J are given by

$$\tau = a + a^* - 2q_n^2$$
$$\Delta = |a|^2 - (1-ic_1)aq_n^2 - (1+ic_1)a^*q_n^2 + (1+c_1^2)q_n^4 - (1+c_2^2)\eta^4\,.$$

Using the definition of a in Eq. (3.8) one obtains [15]

$$\tau = 2 - 4\eta^2 - 2q_n^2 \tag{3.10}$$
$$\Delta = 1 + \nu^2 + 3\eta^4(1+c_2^2) + (1+c_1^2)q_n^4 - 4\eta^2(1+c_2\nu) + 2q_n^2\left(2\eta^2(1+c_1c_2) - (1+c_1\nu)\right)\,. \tag{3.11}$$

The eigenvalues determining the stability can now be calculated as

$$\lambda_\pm = \frac{1}{2}\left(\tau \pm \sqrt{\tau^2 - 4\Delta}\right)\,. \tag{3.12}$$

Thus, the uniform oscillation becomes unstable in two cases: (i) If $\tau > 0$ the system is unstable, independent of the value of Δ. Then, we have

$$\tau = 2 - 4\eta^2 - 2q_n^2 > 0$$
$$\Rightarrow \eta < \sqrt{\frac{1-q_n^2}{2}}\,.$$

For $q_n = 0$ we obtain the threshold η_c: whenever

$$\eta < \eta_c = 1/\sqrt{2} \approx 0.707\,,$$

the uniform oscillation becomes unstable. (ii) If $\tau < 0$, then the determinant has to be negative, $\Delta < 0$, to render the homogeneous mode unstable.

We can conclude from cases (i) and (ii) that for very high values of η the uniform oscillation is always stable, as the η^4 term in the formula for Δ results in a positive determinant. Furthermore, for higher order modes with $q_n > 1$, a positive trace τ is impossible. Also the q_n^4 term in the determinant gives rise to positive Δ at large values of q_n. Thus, higher order modes are always damped, which is important, since in numerical simulations performed in Fourier space, which is also the case in this thesis, very high modes are neglected.

We are now aware of the parameter regions, in which the uniform oscillation is unstable and where hence pattern formation can be expected. In the next sections, we present two hierarchies of dynamics found in simulations of the MCGLE. Subsequently, we will compare one of the two types to the patterns found in the experiments.

3.3 From cluster to chimera states: type I dynamics

The first type of dynamics we present are patterns related to well-known amplitude clusters [98]. The dynamics of such amplitude clusters is visualized in Fig. 3.8a in a two-dimensional snapshot showing $|W(x, y)|$ (left), a one dimensional cut as indicated in the snapshot versus time (middle) and a snapshot of the arrangement of the local oscillators in the complex plane (right). Parameters read $c_1 = 0.2$, $c_2 = 0.56$, $\nu = 1.5$ and $\eta = 0.9$. Thus, the trace τ is negative in Eq. (3.12) and the determinant Δ renders the system unstable. Amplitude clusters consist of regions separated mainly by an amplitude difference. Both groups oscillate, with a small phase difference to each other, at constant, but different amplitude.

Changing parameter c_2 to $c_2 = 0.58$, we obtain symmetry-breaking dynamics, as shown in Fig. 3.8b. Synchronized regions of constant amplitude coexist with regions, where amplitude waves are emitted from the boundaries and from amplitude-spiral cores. The amplitude spirals are visible in the two-dimensional snapshot. Interestingly, there is no amplitude defect in the spiral core and the spiral dynamics take place in a very curved and confined region. In typical reaction-diffusion systems, the amplitude drops to zero in the center of a spiral, constituting an amplitude defect. This is reasonable as in the spiral center the phase jumps. Furthermore, spiral dynamics are typically strongly present in the phase variables, while they are less pronounced in the amplitudes. Here, dynamics are mainly found in the modulus, while the phase hardly exhibits any spatial pattern, its more or less uniform in the two regions, with a small phase shift between the regions. This is also obvious from the arrangement in the complex plane. In the amplitude cluster state in Fig. 3.8a, the two groups of oscillators reside at the two ends of the string visible in the complex plane. Going to spiral-wave like dynamics in Fig. 3.8b, the group at the lower radius desynchronizes slightly to form a bunch. Inside the bunch the relative amplitude differences are much larger than the mutual phase differences.

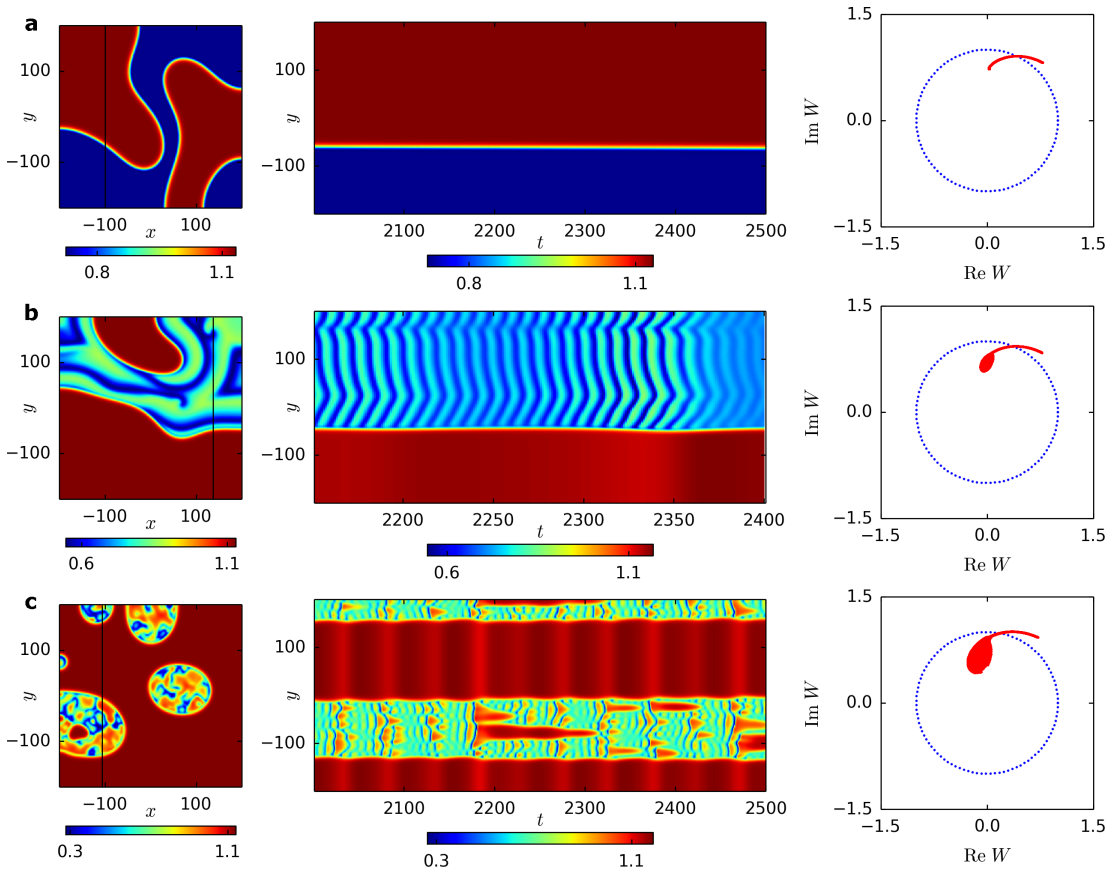

Figure 3.8: Type I patterns found in Eq. (3.4): snapshots of $|W|$ (left column), one-dimensional cuts versus time (also $|W|$) as indicated by the vertical lines in the snapshots (middle column) and snapshots of the arrangement of local oscillators in the complex plane (right column). (a) Amplitude clusters ($c_1 = 0.2$, $c_2 = 0.56$, $\nu = 1.5$, $\eta = 0.9$). (b) Coexistence of synchrony and spiral-wave like dynamics. Waves are emitted from the region boundaries and from the spiral cores ($c_1 = 0.2$, $c_2 = 0.58$, $\nu = 1.5$, $\eta = 0.9$). (c) Type I chimera state consisting of oval-shaped regions exhibiting desynchronized behavior in an otherwise homogeneous background. ($c_1 = 0.2$, $c_2 = 0.61$, $\nu = 1.5$, $\eta = 1.0$).

This bunch of oscillators at the lower radius desynchronizes even more when changing parameters to $c_2 = 0.61$ and $\eta = 1.0$. Now, the symmetry-breaking is more dramatic: Synchronized regions of constant amplitude coexist with regions displaying amplitude turbulence, see Fig. 3.8c. This is an example for a chimera state, which is mainly present in the modulus dynamics. Dynamics in the desynchronized regions are reminiscent of intermittent behavior in the standard complex Ginzburg-Landau equation [57]: homogeneous spots pop up in an irregular manner, vanishing slowly afterwards. Amplitude defects do not occur. One observes a slight oscillation in the amplitude of the homogeneous part and this seems to be connected to size oscillations of the desynchronized

regions, as visible in the one-dimensional cut. Furthermore, in both, the spiral-wave like dynamics and the chimera state, the dynamics in the incoherent regions are overlayed by an overall oscillation, washing out the patterns repeatedly. However, it does not seem that the dynamics are resetted, but rather the visualization becomes blurry.

Type I chimeras are related to amplitude clusters, as the two groups in both states are separated by an amplitude difference. Thus, the clustering mechanism is needed to yield two separated groups in order to obtain the dynamics presented here. Then, the symmetry is broken due to nonlinear amplitude effects: since the response on a force depends on the amplitude of the oscillator, the response is different in the two groups at different moduli. As we will see in Section 3.4, the modulated amplitude clusters give rise to a second type of chimera states.

3.3.1 Type I chimeras under linear global coupling

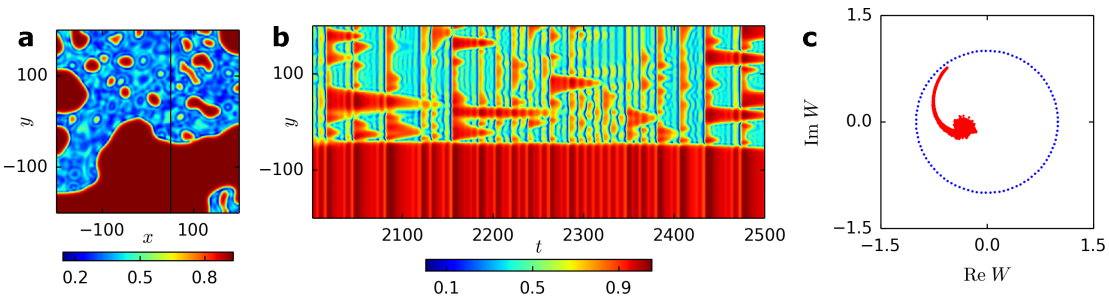

Figure 3.9: Type I chimera state in a CGLE with linear global coupling, given in Eq. (3.13). Shown are a two-dimensional snapshot of the modulus (a), a one-dimensional cut of the modulus versus time (b) and the arrangement of local oscillators in the complex plane (c). Parameters read $c_1 = 1.2$, $c_2 = 1.7$, $K = 0.67$ and $c_3 = -1.25$.

Interestingly, one finds type I chimeras also in a CGLE with linear global coupling:

$$\frac{\partial W}{\partial t} = W - (1 + ic_2)\,|W|^2\,W + (1 + ic_1)\nabla^2 W + K(1 + ic_3)\,(\langle W\rangle - W)\ . \tag{3.13}$$

The linear average $\langle W\rangle$ constitutes the linear global coupling, $K(1 + ic_3)$ is the complex prefactor with parameters K and c_3. Numerical results are depicted in Fig. 3.9. The one-dimensional cut of $|W|$ reveals that the spatio-temporal dynamics are qualitatively the same as in the type I chimeras found in the MCGLE, see Fig. 3.8c. Moreover, the arrangement of local oscillators in the complex plane in Fig. 3.9c resembles the configuration in case of the MCGLE. Differences are that the incoherent domains in Fig. 3.9a are not of oval shape and that one observes a rather irregular oscillation in the modulus in the one-dimensional cut, instead of a more periodic one. These states are related to chimera states found in an ensemble of Stuart-Landau oscillators with linear global coupling [99]. We will see in Section 4.3 that the mean-field in case of the chimera state under linear global coupling oscillates approximately harmonically

and that the amplitude clusters and type I chimeras found in our model constitute idealized dynamics of the corresponding patterns found under linear global coupling.

3.4 From cluster to chimera states: type II dynamics

For $c_2 = -0.7$, $\nu = 0.1$ and $\eta = 0.66$ we find a second type of cluster pattern, which is presented in Fig. 3.10a. Note that here we plot the real part of W in the snapshots, as both the modulus and the phase exhibit significant variations in case of the type II dynamics. The system again splits into two phases, but the one-dimensional cuts versus time show that the dynamics are more complex than in case of amplitude clusters. We observe an overall uniform oscillation, which is modulated by two-phase clusters. Thus, we call this type of clustering modulated amplitude clusters, as the clusters are a modulation of the amplitude of a uniform oscillation. The modulational oscillations can be seen best in the one-dimensional cut of $|W|$, depicted in the right column of Fig. 3.10a. This pattern is one of the most prominent patterns in the photoelectrodissolution of n-type silicon [13, 15, 79, 91] and the MCGLE thus reproduces this pattern very well.

The second type of clusters also undergoes a symmetry-breaking transition [79], here when changing c_2 to $c_2 = -0.67$, resulting in subclustering as shown in Fig. 3.10b. One phase exhibits two phase clusters as a substructure, while the other one stays homogeneous. The substructure-clusters oscillate at half the frequency of the modulational oscillations as the cut of $|W|$ in the right column of Fig. 3.10b demonstrates. Therefore, we suspect the subclustering being connected to a period-doubling bifurcation.

Changing the parameter further to $c_2 = -0.58$ the symmetry-breaking becomes again more dramatic: the beforehand existing two-phase subclusters turn into turbulence, thus realizing a second type of chimera states, see Fig. 3.10c. We could not resolve, whether the transition from subclustering to the chimera state is a period-doubling route to chaos or the breakdown of a 3-torus [100]. Both seems to be reasonable.

At this point, we have to emphasize the connection to the photoelectrodissolution of silicon, since this second type of chimera states can be observed in experiments, too [79, 91]. We compare the simulations and the experiments in detail in the next section.

In type II states, the specific interaction between the two phases via the nonlinear global coupling leads to a symmetry-breaking transition, as we will show in the following. Let us call the two phases A and B, respectively. Simulations show that the system evolves according to a minimization of the interface between A and B. This leads to a demixing of the phases. Long-term simulations for a modulated amplitude cluster state and a chimera state are shown in Figs. 3.11a and b, respectively, demonstrating that the phase boundary eventually becomes straight. As the diffusional coupling between A and B acts only near the boundaries, for large domain sizes it can be neglected. Under this assumption, the dynamics in each phase is governed by

$$\partial_t W_X(\mathbf{r},t) = W_X(\mathbf{r},t) + (1+ic_1)\nabla^2 W_X(\mathbf{r},t) - (1+ic_2)\,|W_X(\mathbf{r},t)|^2\, W_X(\mathbf{r},t) + Z(W_A,W_B)\,,$$

where X = A, B and $Z(W_A, W_B)$ is the coupling between A and B and has to be deter-

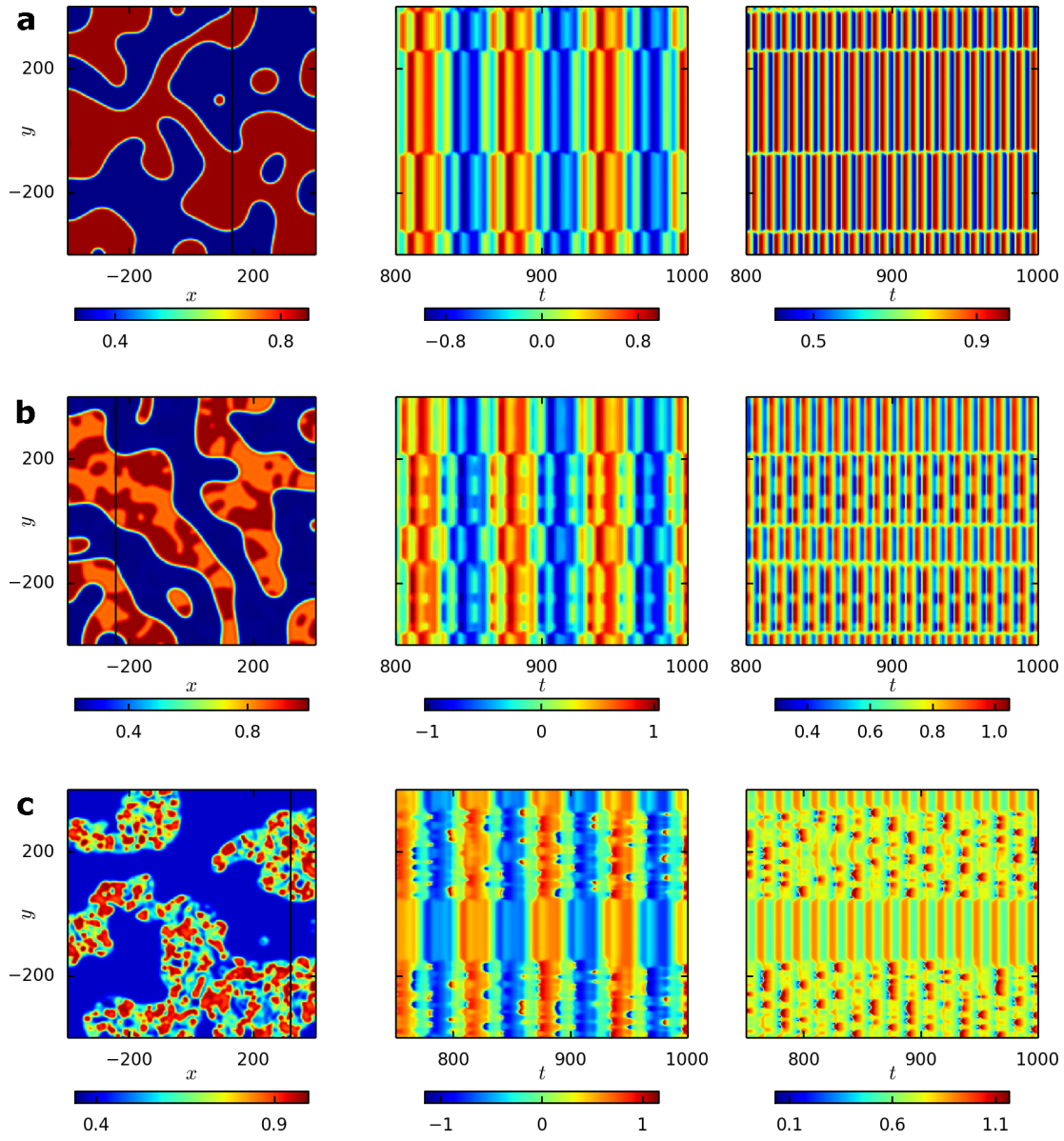

Figure 3.10: Type II patterns found in Eq. (3.4): two-dimensional snapshots of Re W in left column, one-dimensional cuts of Re W in middle column and of $|W|$ in right column. (a) Modulated amplitude clusters ($c_1 = 0.2$, $c_2 = -0.7$, $\nu = 0.1$, $\eta = 0.66$). (b) Subclustering, where one phase is synchronized, while the other one exhibits two-phase clusters as a substructure ($c_1 = 0.2$, $c_2 = -0.67$, $\nu = 0.1$, $\eta = 0.66$). (c) Type II chimera ($c_1 = 0.2$, $c_2 = -0.58$, $\nu = 0.1$, $\eta = 0.66$).

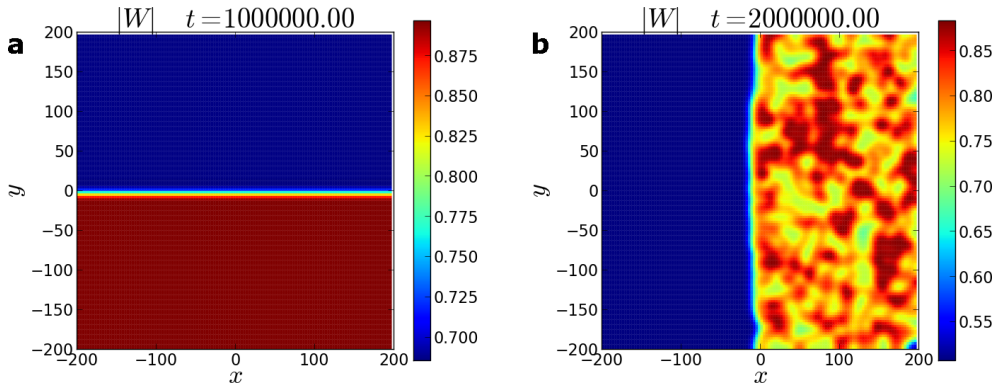

Figure 3.11: After long simulation times the boundaries between the phases in case of modulated amplitude clusters (a) and type II chimera states (b) become approximately straight. Simulation times are indicated in the figures. Note that the chimera state shown here is in fact an alternating chimera state, cf. Section 3.6. Parameters read: $c_1 = 0.2$, $c_2 = -0.7$, $\nu = 0.1$, $\eta = 0.66$ (modulated amplitude cluster, a); $c_1 = 0.2$, $c_2 = -0.64$, $\nu = 0.1$, $\eta = 0.66$ (type II chimera, b). I thank Sindre W. Haugland for providing these figures.

mined. Exploiting the conservation law for the homogeneous mode, one finds

$$Z(W_A, W_B) = -(1 + i\nu)\eta \exp(-i\nu t) + (1 + ic_2)\frac{1}{2}\left(\left\langle |W_A|^2 W_A \right\rangle + \left\langle |W_B|^2 W_B \right\rangle\right) .$$

We can further write for the spatial averages over phases A and B, $R_A \exp(-i\alpha) \equiv \left\langle |W_A|^2 W_A \right\rangle$ and $R_B \exp(-i\beta) \equiv \left\langle |W_B|^2 W_B \right\rangle$, respectively, and $K \exp(i\gamma) \equiv (1 + ic_2)/2$, where $\gamma = \gamma(c_2)$. With the phase difference $\Delta\phi \equiv \beta - \alpha$ between A and B, one can now show that the intra-group coupling differs from the inter-group coupling. Note that $\Delta\phi$ is generally unequal to π for the dynamics we consider here. One obtains in terms of α

$$Z(W_A, W_B) = -(1 + i\nu)\eta e^{-i\nu t} + KR_A e^{i(\gamma-\alpha)} + e^{-i\Delta\phi} KR_B e^{i(\gamma-\alpha)} .$$

We see that phases A and B experience each a different influence from the intra- and inter-group couplings. This is not due to a difference in coupling strength defined a priori, but is the result of the intrinsic dynamics causing the phase difference. As studies of two subpopulations in Refs. [23, 31] with global intra- and inter-group couplings of different strength show the existence of chimera states, we conclude that the similar situation arising here renders the emergence of chimeras possible. The coupling can be tuned with the parameter c_2, where the influence is different on inter- and intra-group coupling if $\Delta\phi$ depends also on c_2, which is a reasonable assumption. Note that these considerations in principle also apply to type I chimeras. However, we think that the difference in the mean amplitudes between the groups is more important in case of type I chimeras, since, due to nonlinear amplitude effects, the response on a force depends on the actual amplitude and thus, the response differs in the two groups. This strongly breaks the symmetry between the two groups.

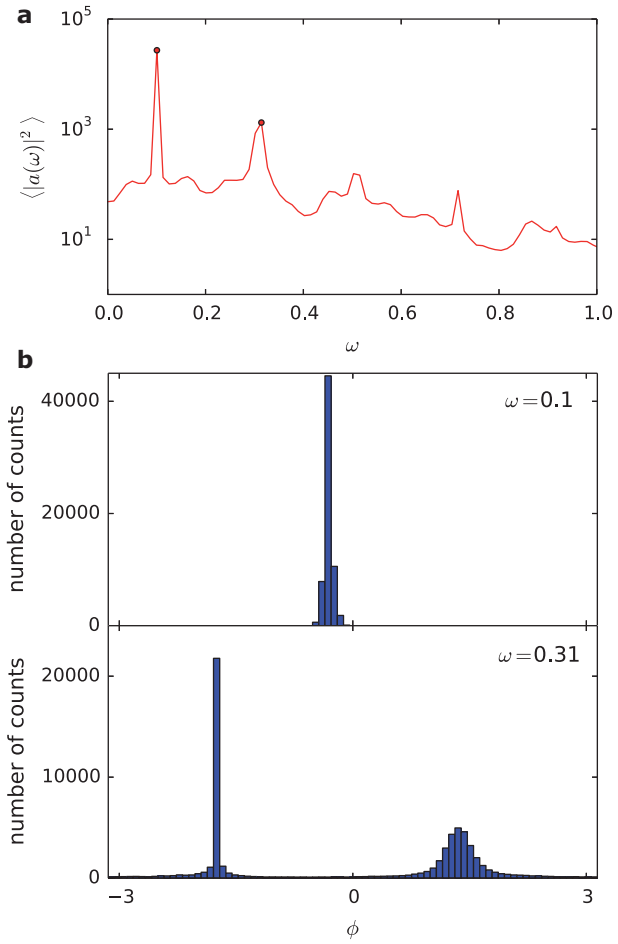

Figure 3.12: Cumulative power spectrum in (a) and phase histograms for the Fourier amplitudes $a(\mathbf{r}, \omega)$ at the highest peak in (b) and at the second highest peak in (c), which are indicated by circles in (a).

The observations above rationalize the symmetry-breaking. Now, we analyze the frequency spectrum of the type II chimeras. Therefore, we perform a Fourier transformation in time of the real part of $W(\mathbf{r}, t)$ at every point $\mathbf{r} = (x, y)$ [13]. We spatially average the resulting squared amplitudes $|a(\mathbf{r}, \omega)|^2$ to obtain the cumulative power spectrum $S(\omega) = \left\langle |a(\mathbf{r}, \omega)|^2 \right\rangle$. The resulting spectrum for the simulation presented in Fig. 3.10c is depicted in Fig. 3.12a. Due to the turbulence in the incoherent phase it consists of a large background, but exhibits also two major peaks, marked with circles. The highest peak is at the frequency ν of the mean-field oscillation, see Eq. (3.6). The second highest peak stems from the clustering frequency: as outlined above, in the modulated amplitude clusters one observes two major frequencies, one of the homogeneous oscillation and one as a result of the modulational oscillation. In the type II

chimera, the separation into two different phases occurs via this clustering mechanism and therefore, some properties of it are still present. This becomes more clear, when inspecting the Fourier amplitudes $a(\mathbf{r}, \omega)$ at the two highest peaks, which consist of moduli and phases. The distribution of phases of the local oscillators at the two peaks is shown in histograms in Figs. 3.12b and c. At frequency ν, Fig. 3.12b, the existence of only one, sharp peak demonstrates that all local oscillators perform the homogeneous oscillation in synchrony. The histogram for the second highest peak at $\omega \approx 0.31$ reveals that the clustering mechanism is still active: we encounter two peaks for the two groups, which are phase shifted by π, indicating that at this frequency the clustering occurs. The left peak is sharp and describes the synchronized oscillators, while the right peak has a Gaussian-like shape, thus, describing the incoherent oscillators.

The type II dynamics presented in this section are in fact the type of patterns that are also found in the experiments. Therefore, we compare simulation results and experimental results in detail in the next section. Even the chimera state can be observed in the experiments. Furthermore, in Section 4.3 we investigate the type II chimeras also in the Stuart-Landau ensemble. We will highlight the connection to the modulated amplitude clusters and show that the motions in the incoherent parts of both types of chimeras are indeed chaotic.

3.5 Experiment versus theory

We presented two types of spatio-temporal dynamics found in simulations of the MCGLE in the last two sections. The MCGLE was proposed as a general model describing the dynamics during the photoelectrodissolution of n-type silicon. In this section, we test this assumption by comparing the simulation results with patterns found in the experiments. So far, only the type II dynamics reproduce experimental patterns, while type I dynamics have not been found in the experiment yet. We depicted the type II dynamics in the experiments in Fig. 3.7. We see that typical features are similar and that we can thus identify experimental patterns with patterns found in the MCGLE. In what follows, we will compare each of the states in detail and will additionally have a look at spatio-temporal turbulence.

3.5.1 Cluster patterns

We found two types of cluster patterns in the simulations. Here, we will compare the modulated amplitude clusters to experimental cluster patterns. In Fig. 3.13 we depict the cluster dynamics in the simulations of Eq. (3.4) and the experimental ones [79]. In Figs. 3.13a and c two-dimensional snapshots of the simulations and the experiments, respectively, are shown. The spatio-temporal dynamics can be seen in one-dimensional cuts in Figs. 3.13b and d for the simulations and the experiments, respectively. They show that the homogeneous oscillation is modulated by two-phase clusters, in both cases. Therefore, it is clear, that the phase shift between two regions is not given by π.

To analyze and compare time series of the dynamics, we perform a Fourier transformation in time at every point $\mathbf{r}$ of the ellipsometric signal and of the real part of $W(\mathbf{r}, t)$ for the experiments and simulations, respectively [13]. We spatially average the resulting squared amplitudes $|a(\mathbf{r}, \omega)|^2$ to obtain the cumulative power spectrum $S(\omega) = \left\langle |a(\mathbf{r}, \omega)|^2 \right\rangle$. Results are shown in Fig. 3.14.

Two major peaks occur in both cumulative power spectra in Fig. 3.14a (theory) and d (experiment), one at the frequency ν of the mean-field oscillation. The other one describes the frequency of the clusters. This becomes clear when considering the Fourier amplitudes, corresponding to these peaks, in the complex plane: At $\omega = \nu$ (Figs. 3.14b and e) all local oscillators form a bunch, while at $\omega \approx \nu/2$ (Figs. 3.14c and f) the oscillators arrange into two clusters, located at the endpoints of the bar visible. Due to the diffusive coupling, the clusters are connected by an interfacial region, leading to the intermediate oscillators of the bar. The fact that the connection of the two clusters crosses the zero point implies that the borders between them are Ising-type walls. As in this picture the phase shift between the two clusters is given by π, we conclude that at this frequency the clustering takes place. Due to the Ising-type walls, the borders are static, at least on a short time scale. In fact, on a long time scale the borders in the simulation move, thereby reducing curvature. The experiments cannot be performed on such a long time scale, as the basic oscillation has a period of about 250s. Waiting for e.g. 1000 oscillations of the mean-field would take several

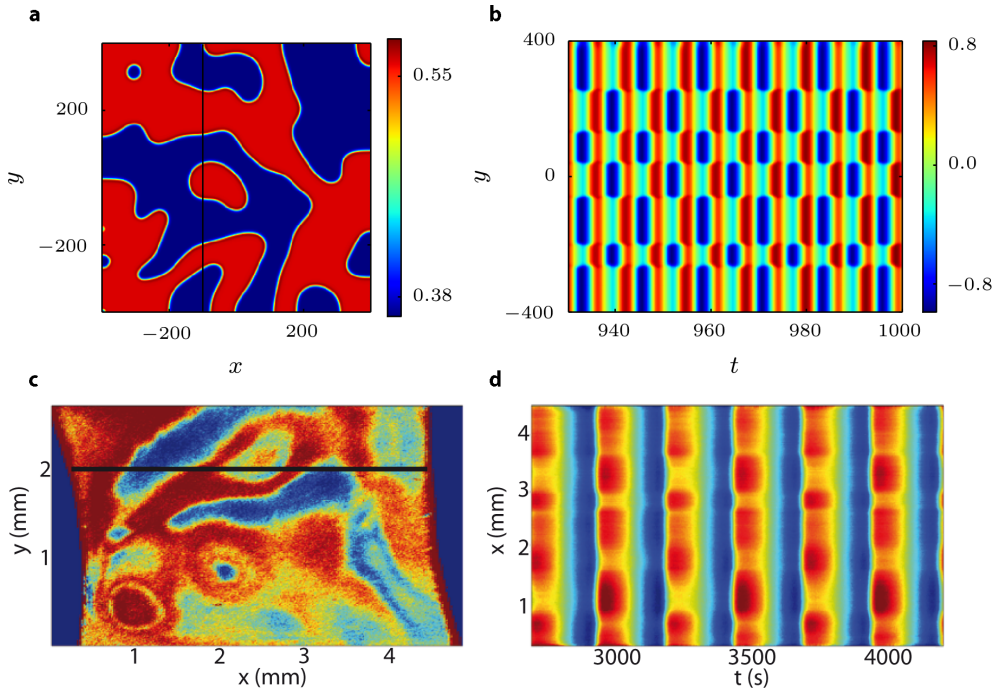

Figure 3.13: Two-phase clusters in theory (a,b) and experiment (c,d). (a) Snapshot of the two-dimensional oscillatory medium in the theory. Shown is the real part of W. (b) Spatio-temporal dynamics in a one-dimensional cut versus time in the theory. (c,d) The same as (a,b) now for the experimental results. The simulation captures the experimental dynamics very well. Note that the colorbars are different for each subfigure. Parameters read: $c_1 = 0.2$, $c_2 = -0.58$, $\nu = 1.0$, $\eta = 0.66$ (simulation) and $c_F = 35$ mM, pH=1, $R_{ext} \cdot A = 9.1$ kΩcm^2, $I_{ill} = 0.7$ mW/cm^2 (experiment). *Taken from Ref. [80].*

days. During this timespan, it is not possible to keep the experimental parameters constant in the present setup. In the experiments, in most cases the cluster frequency is given by approximately $\nu/2$. This leads to the conclusion that the clusters arise via a period-doubling bifurcation. Contrarily, in the theory the cluster frequency can be tuned continuously. This suggests that the modulated amplitude clusters arise in the MCGLE in a secondary Hopf bifurcation, not in a period-doubling bifurcation. We will investigate this question in Chapter 4. However, we cannot proof that it is a period-doubling bifurcation in the experiments. Maybe the dynamics are confined to a parameter region, where the clustering frequency approximately amounts to $\nu/2$; or cluster patterns with other frequencies are simply unstable. For better comparison of theory and experiment, we chose the parameter values in the simulations such that the clustering frequency also amounts to $\nu/2$.

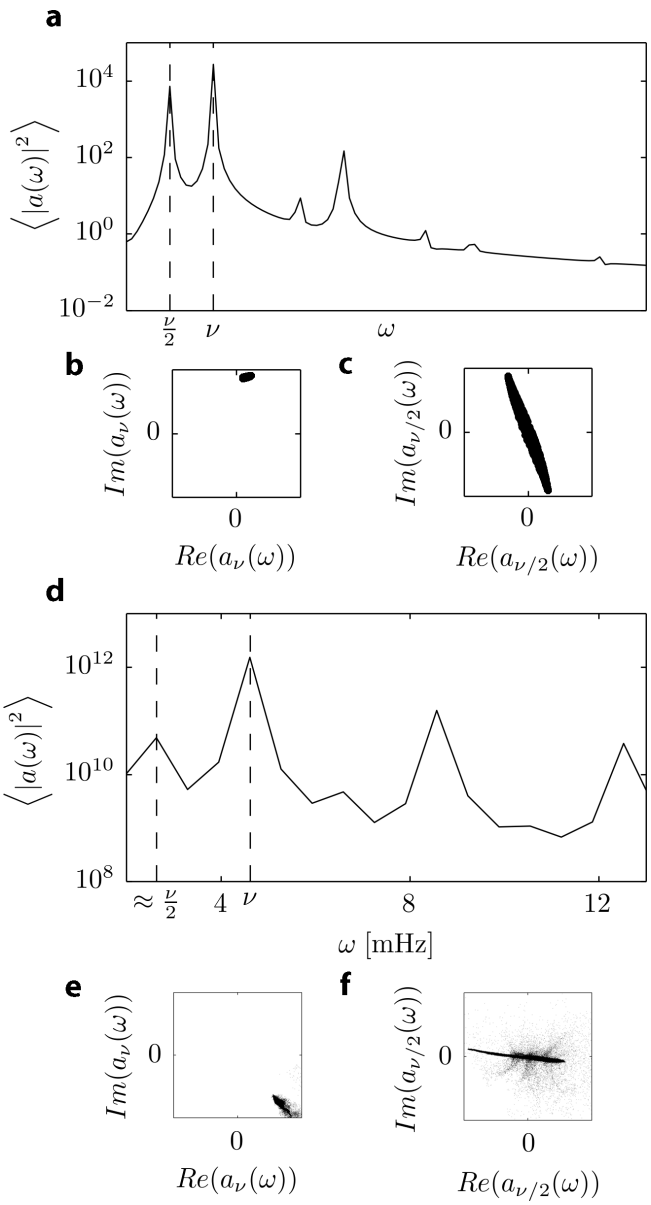

Figure 3.14: (a,d) Cumulative power spectra for simulations and experiments, respectively. The two major peaks at ν and approximately $\nu/2$ are indicated. The arrangement of the local Fourier amplitudes in the complex plane corresponding to these peaks are depicted in (b) and (c) for the theory and (e) and (f) for the experiments, respectively. The whole two-dimensional system is considered, which leads to the scattered oscillators in the experimental result in (f). *Taken from Ref. [80].*

3.5.2 Subclustering

The symmetry-breaking type of clustering found in our simulations also occurs in the experiments. The system again separates into two regions as in the case of the two-phase clusters, but now one region is homogeneous, while the other one exhibits two-phase clusters as a substructure [79]. Such states were also observed in Refs. [19, 31]. Results are depicted in Fig. 3.15. Note that we present in Fig. 3.15b the modulus

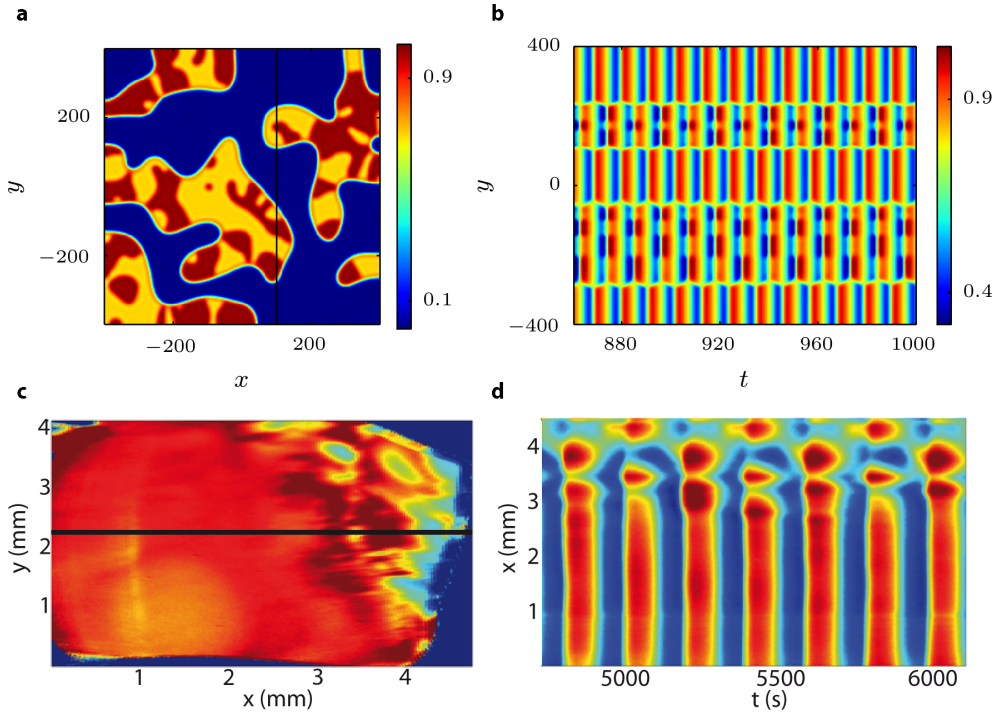

Figure 3.15: Subclustering in theory (a,b) and experiment (c,d). Again snapshots (a,c) and one-dimensional cuts (b,d) are shown. The system splits into two regions, one region being homogeneous and one exhibiting two-phase clusters as a substructure. Note that in (b) for better visibility $|W(y,t)|$ is shown. Parameters read: $c_1 = 0.2$, $c_2 = -0.67$, $\nu = 0.1$, $\eta = 0.66$ (simulation) and $c_F = 35$ mM, pH=1, $R_{ext} \cdot A = 7.6$ kΩcm^2, $I_{ill} = 0.5$ mW/cm^2 (experiment). *Taken from Ref. [80].*

$|W(y,t)|$ instead of the real part. For a picture of the real part see Fig. 3.10b. In $|W|$ one observes oscillations with a main frequency given by the frequency of the modulations. In the cut in Fig. 3.15b it is visible that the subclusters oscillate at half of this frequency, indicating that this phenomenon is related to a period-doubling bifurcation. In contrast, in the experiments the mechanism seems to be a demixing of the modulated amplitude cluster state into a synchronized region oscillating with the mean-field frequency and a region with two-phase clusters that are not a modulation of an underlying oscillation. These two-phase clusters oscillate at half the frequency of the synchronized region. Demixing thus means here that the oscillation with two frequencies, present in the

modulated amplitude cluster state, separates spatially into two regions with the two frequencies. Thus, simulation and experiment share qualitative features, while there are differences in the detailed dynamics.

3.5.3 Chimera states

Also the peculiar dynamics of the chimera state can be found in the photoelectrodissolution of n-type silicon. It resembles the type II chimeras found in the simulations. For comparison, we present in Fig. 3.16 the chimera state found in the simulations (a,b) and the one found in the experiments (c,d) [79].

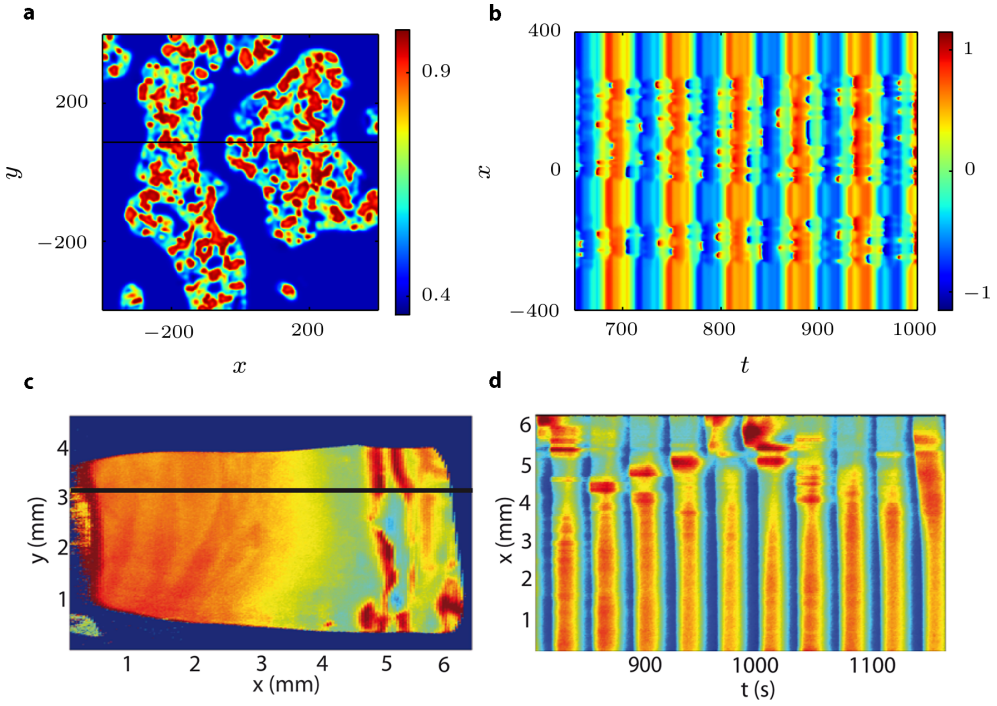

Figure 3.16: Chimera states in theory (a,b) and experiment (c,d). Snapshots (a,c) and one-dimensional cuts (b,d) are shown. In both, the simulation and the experimental pattern, the synchronized and turbulent regions can be distinguished clearly. Parameters read: $c_1 = 0.2$, $c_2 = -0.58$, $\nu = 0.1$, $\eta = 0.66$ (simulation) and $c_F = 75$ mM, pH=3.5, $R_{ext} \cdot A = 5.61$ kΩcm^2, $I_{ill} = 1.8$ mW/cm^2 (experiment).

In both, the experiments and the simulations nothing is imposed to induce this symmetry-breaking. The experimental conditions are kept uniform over the entire electrode. Furthermore, these patterns form spontaneously, i.e., no specially prepared initial conditions are required to obtain them.

We make a direct comparison of the theoretical and experimental spatial profiles in Fig. 3.17. The real part of W is shown in Fig. 3.17a and the oxide-layer thickness ξ is shown in Fig. 3.17b, respectively. The experimental results are from the run shown in

Fig. 3.7(e,f). The plots in Figs. 3.17a and b show an excellent qualitative agreement.

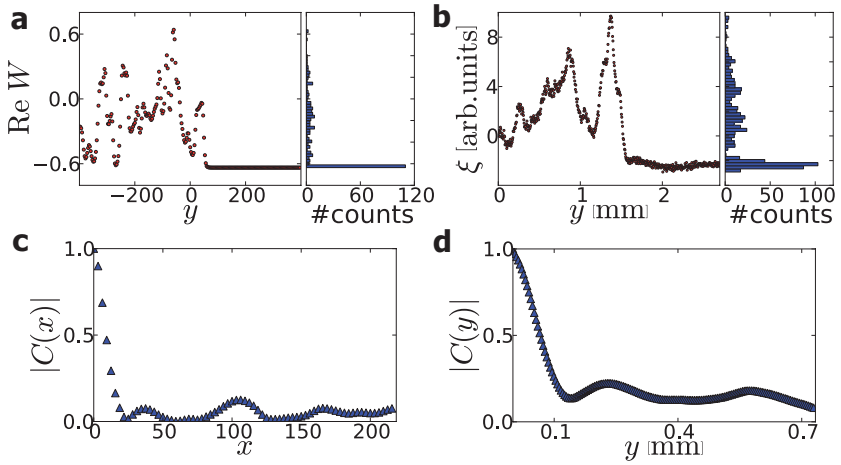

Figure 3.17: Comparison of theoretical and experimental chimera states. The one-dimensional spatial profiles in theory (**a**) and experiment (**b**) are in excellent agreement. Furthermore, both correlation functions $|C(x)|$ (for details see text) exhibit a fast drop to nearly zero. This shows the fast decrease of spatial correlations in theory (**c**) and experiment (**d**). Experimental parameters are as in Fig. 3.7(e,f).

Finally, we quantify the incoherence in the turbulent regions of the chimera state: We calculate the correlation function $C(x,t) = \left\langle \tilde{W}(x,t)\tilde{W}^*(0,0)\right\rangle_{x',t'} / \left\langle \left|\tilde{W}(0,0)\right|^2\right\rangle_{x',t'}$ (the asterisk denotes complex conjugation and the average is performed over space and time) in a cut in the incoherent region for both theory and experiment, where $\tilde{W}$ is obtained by subtracting the average of this cut from the original data. From the experimental data the complex signal $W(x,t)$ was obtained via a Hilbert transformation [101]. The resulting $|C(x)| \equiv |C(x,0)|$ is shown in Figs 3.17c (theory) and d (experiment). As seen in the figures, $|C(x)|$ drops very fast to approximately zero, demonstrating that after this distance the individual oscillators behave uncorrelated. Note that the fluctuations of $|C(x)|$ are due to the finiteness of the sample.

3.5.4 Turbulence

As the coexistence of synchrony and turbulence in the chimera state suggests, we find this state in parameter space between fully synchronized and turbulent states. Therefore, the chimera state can be regarded as a mediator between synchrony and turbulence. An experimental example of the synchronized state is shown in Fig. 3.2, whereas the turbulent dynamics in simulation and experiment are presented in Fig. 3.18.

An uniform oscillation is still present in the dynamics, but it is modulated by incoherent and aperiodic oscillations. Similar turbulent patterns have been described in Ref. [11], where also localized clusters are discussed, which are reminiscent of the

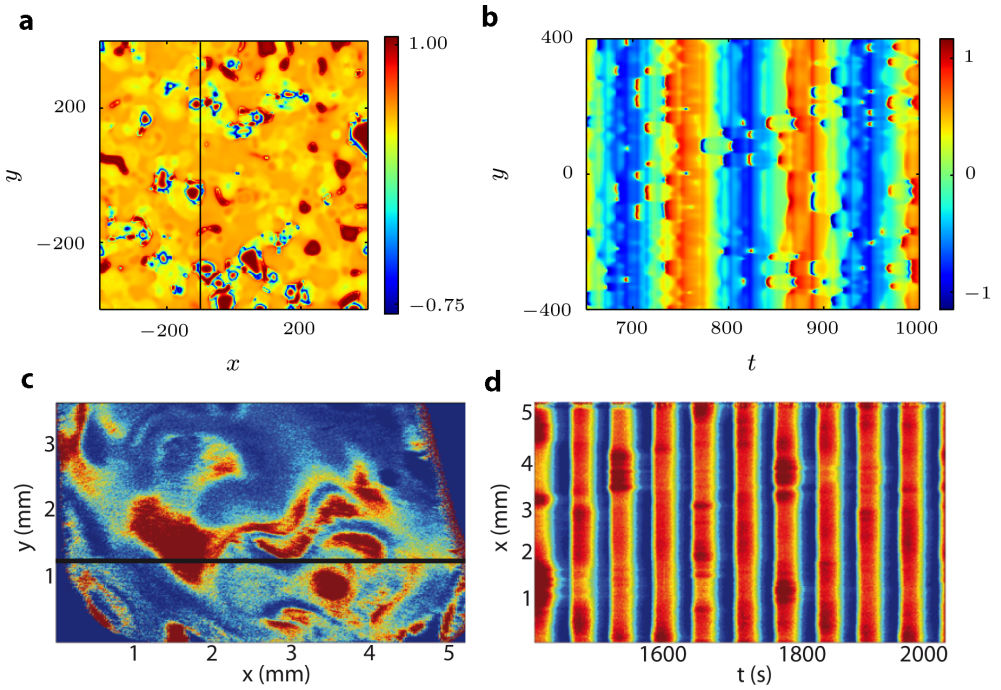

Figure 3.18: Turbulent dynamics in theory (a,b) and experiment (c,d). Snapshots (a,c) and one-dimensional cuts (b,d) are shown. The whole system exhibits turbulent dynamics. Parameters read: $c_1 = 0.2$, $c_2 = -0.58$, $\nu = 0.05$, $\eta = 0.66$ (simulation) and $c_F = 50$ mM, pH=3, $R_{ext} \cdot A = 6.7$ kΩcm^2, $I_{ill} = 1.0$ mW/cm^2 (experiment). *Taken from Ref. [80].*

subclusters presented in Fig. 3.15. In this reference, the authors consider the Belousov-Zhabotinsky reaction-diffusion system with photochemical global feedback. Interestingly, the average concentration of the catalyst also displays periodic oscillations in case of "irregular clusters", which is the dynamics similar to the ones presented in Fig. 3.18.

This finishes our comparison of theory and experiment. In the discussion at the end of this chapter, we will summarize the results and identify similarities, as well as differences.

3.6 Alternating chimera states

In the chimera states presented so far, synchronized and desynchronized regions might grow and shrink, but will not switch their character, meaning there is no interchange of synchronized and desynchronized regions. However, in unihemispherical sleep, a prominent example in nature exhibiting similar features like chimera states, the sleeping (synchronized) and awake (desynchronized) cerebral hemispheres interchange their state from time to time [38, 39, 42]. This kind of sleep is performed by, e.g., various dolphins and birds. Up to now, the alternation phenomenon could only be

reproduced in models of non-identical oscillators that are grouped a priori, with different intra- and inter-group coupling strengths, without external periodic forcing [43] and with forcing [44]. In contrast, here we present alternating chimera states emerging spontaneously in an isotropic medium and with symmetrical and identical coupling for all oscillators. This work was done together with Sindre W. Haugland, in the course of his Master Thesis. The principle existence of these states in our model is reasonable, since the type II chimera states described in the preceding sections seem to occur always in a phase-balanced configuration, i.e., both phases are of the same size. In such a situation, interchanging both regions again yields a solution to the underlying equations. This renders alternating chimeras possible.

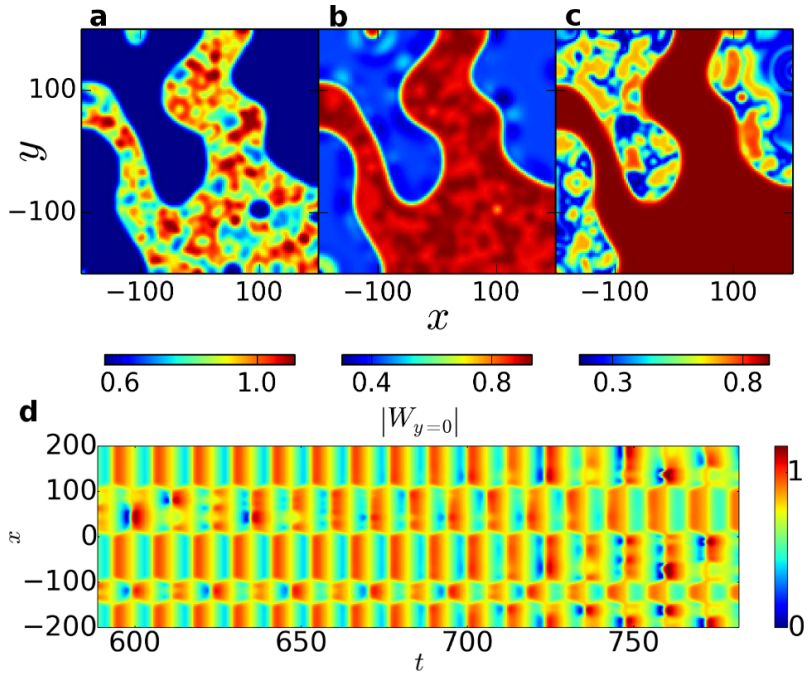

Figure 3.19: Alternating chimera state with curved boundaries. (a)-(c) Two-dimensional snapshots of $|W|$ at consecutive times showing the interchange of synchrony and incoherence. (d) One-dimensional cut along the x-axis showing the spatio-temporal dynamics of $|W|$ during the alternation process from (a) to (c). Parameters read: $c_1 = 0.2$, $c_2 = -0.64$, $\nu = 0.1$, $\eta = 0.66$.

A series of snapshots is presented in Figs. 3.19a-c, elucidating the interchange of synchrony and incoherence. A spatio-temporal visualization of this process is given in Fig. 3.19d. This alternation process occurs rather erratically in time, as long as the domain boundaries are very curvy. Simulating the system for at least $T = 1 \cdot 10^6$, the domain boundaries straighten, as they always do in order to decrease curvature and therefore some interfacial energy (in case of type II dynamics). Then, one is left with two domains separated by a straight boundary as presented in Fig. 3.20. Now

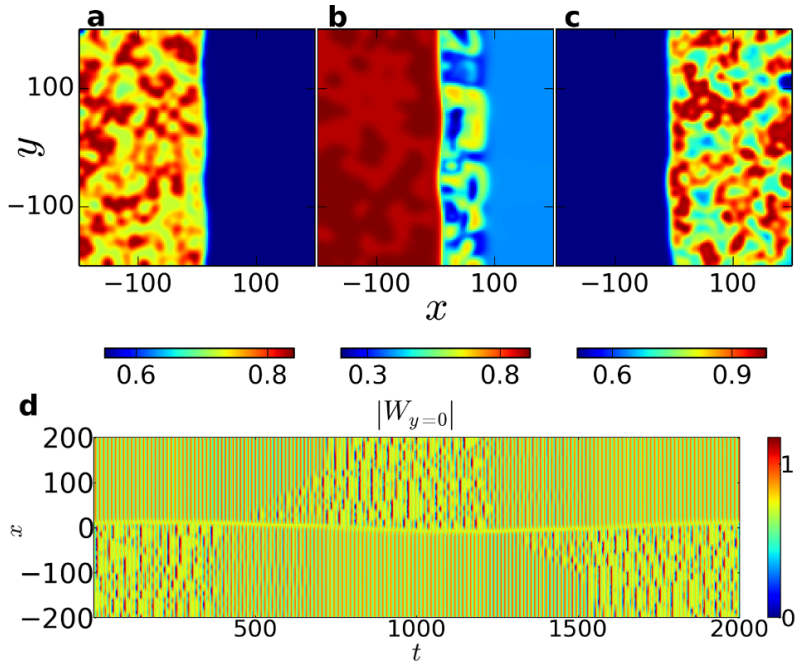

Figure 3.20: Alternating chimera state with straight boundaries. (a)-(c) Two-dimensional snapshots of $|W|$ at consecutive times showing one alternation. (d) One-dimensional cut along the x-axis. Snapshots in (a)-(c) are at $t = 0, 600, 1000$ in the timeline of the cut, respectively.

alternations occur in a more periodic fashion with an approximate period of about $\Delta T = 10^3$. The alternating chimera state seems to be stable, as a simulation up to $T = 3.7 \cdot 10^7$ does not show any break down. The one-dimensional cut in Fig. 3.20d demonstrates how the alternation takes place. First, the turbulence in the incoherent part starts to become synchronized. This is followed by a spread of turbulence in the beforehand synchronized part, which is initiated at the domain boundary acting as an incoherent nucleus.

Of course, the question arises what triggers the alternation. A critical look at the one-dimensional cut in Fig. 3.20d gives a first hint: alternations seem to be connected to a movement of the domain boundary and therefore to a change in the relative sizes of the two domains. It seems that an alternation takes place once the turbulent region becomes larger than the synchronized one. To test this assumption, we modified the initial conditions in order to start on the one hand with a much smaller turbulent region and on the other hand with a much larger turbulent region. The larger turbulent region was obtained via reflection at the system boundary. The results of this investigation are presented in Fig. 3.21. Starting with a small turbulent region, as in Figs. 3.21a and b, gives the following behavior: the turbulent region grows until it becomes slightly larger than the synchronized region, followed by an interchange of dynamics. The growth speed is initially larger and decreases with convergence of the domain sizes, since the phase-balanced state, though unstable in the present case, constitutes an

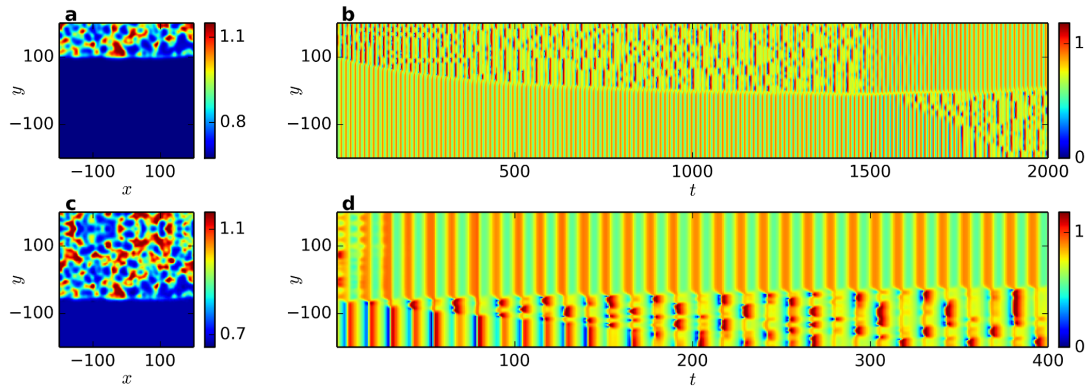

Figure 3.21: Investigating the influence of the domain sizes on the alternation. (a,b) Starting with a small turbulent region, this region will grow until it is slightly larger than the synchronized one, followed by an alternation. (c,d) Starting with a large turbulent region, an immediate, rapid alternation occurs: After the turbulent region synchronized, turbulence spreads in the initially synchronized region.

equilibrium situation.

If the initial coverage of turbulence is significantly larger, shown in Figs. 3.21c and d, an immediate, rapid alternation occurs: After the synchronization of the turbulent region has taken place, turbulence starts to spread from the domain boundary into the initially synchronized domain. Concurrently, this region grows, which occurs at a smaller velocity.

Performing the same type of simulations with modified initial conditions for non-alternating chimera states, one finds the following behavior: an initially smaller turbulent domain grows until phase balance is reached, while in case of an initially larger turbulent domain an alternation takes place. Then, the now smaller turbulent region grows again until phase balance is reached.

We can conclude that an alternation is triggered once the turbulent region becomes larger than the synchronized one. In case of alternating chimera states, the phase-balanced situation is unstable and a turbulent region will always grow and therefore alternations occur repeatedly. In non-alternating chimera states, the phase-balanced configuration is stable and thus, no spontaneous alternations do occur. The question stays, why the turbulent region is growing. This growth behavior has also been found in other reaction-diffusion systems, including a model of catalytic CO oxidation on a Pt(110) surface [102–106].

Similar to the alternating chimera states, also the subclustering state can alternate for $c_2 = -0.66$. However, up to now we could only observe a limited number of alternations as an initial transient.

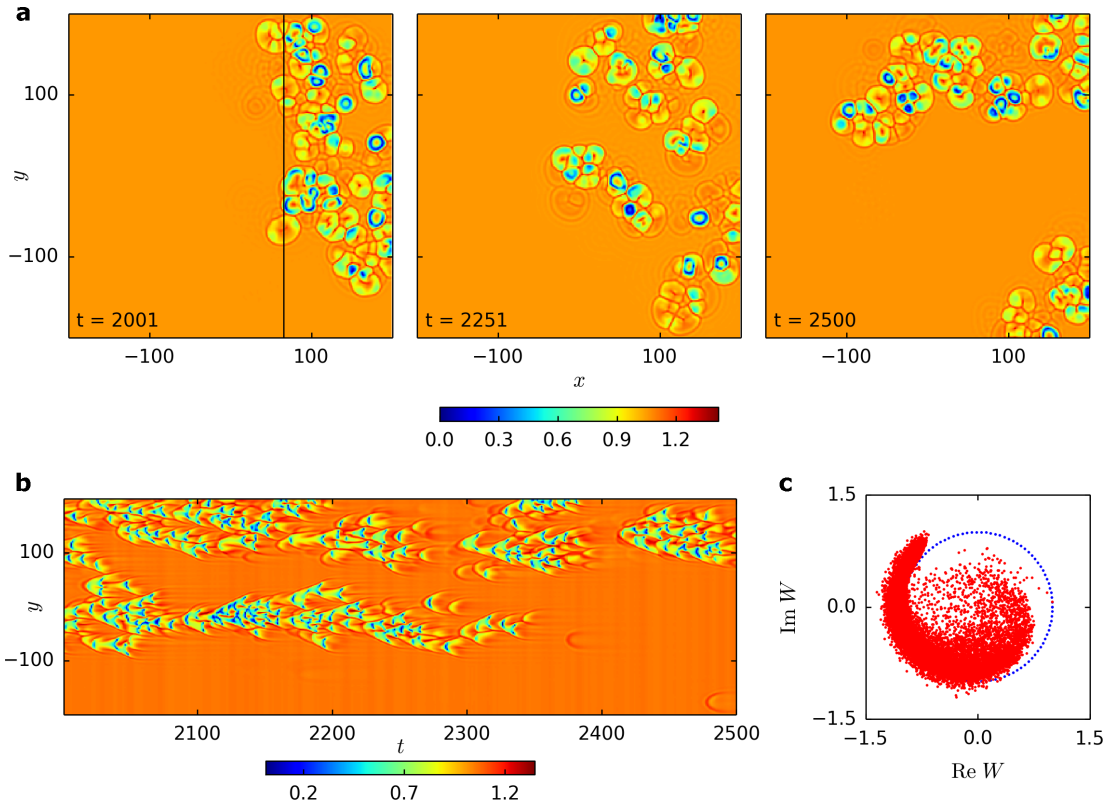

Figure 3.22: Localized turbulence: two-dimensional snapshots of $|W|$ in (a) at times indicated in the figures, one-dimensional cut (also $|W|$) in (b) as indicated in the first snapshot and a snapshot of the arrangement of local oscillators in the complex plane in (c) ($c_1 = -1.6$, $c_2 = 1.5$, $\nu = 1.5$, $\eta = 0.9$).

3.7 Localized turbulence

For a totally different set of parameters, $c_1 = -1.6$, $c_2 = 1.5$, $\nu = 1.5$ and $\eta = 0.9$, we encounter so-called localized turbulence. We depict our results in Fig. 3.22, where we present three snapshots at times indicated in the figures in (a), a one-dimensional cut versus time in (b) and a snapshot of the arrangement of local oscillators in the complex plane in (c). Here, we show again $|W|$. Small spots of turbulence are randomly created in an otherwise homogeneous background, which then move through the system and spread, but always keeping an overall small size. As for their creation, they also vanish in an irregular manner. The turbulence can be described as circular defect lines (or at least lines of very small amplitude) expanding and breaking down. After their breakdown, new defect circles are created. Such localized turbulence has also been observed in the CGLE with delayed global coupling [107]. It is a phenomenon similar to chimera states as the system also shows the coexistence of synchronized and turbulent regions. However, the separation of these regions is fundamentally different.

In the chimera states considered in this thesis and also those discussed in literature, there is a clear separation of coherent and incoherent phases via a phase boundary, as clearly visible in Fig. 3.8c, Fig. 3.9 and Fig. 3.10c. Also in nonlocally coupled systems, where the boundaries are rather smooth, the separation is clearly identifiable [16]. Furthermore, the boundaries move only on a slow timescale. In contrast, the incoherent spots in localized turbulence are not separated from the homogeneous regions by phase boundaries. Albeit, there is also a coexistence of synchrony and incoherence, matching the definition of a chimera state, the two phases, i.e., the synchronized and the incoherent phases, cannot be clearly identified. Therefore, we think the term localized turbulence is more appropriate than chimera state.

3.8 Discussion

During the photoelectrodissolution of n-type silicon, the oxide-layer on the silicon working electrode exhibits peculiar spatio-temporal pattern formation [13, 14, 79, 80, 91]. Essential features of the experimental dynamics are: (i) the nearly harmonic oscillation of the mean oxide-layer thickness, (ii) the uniform oscillation arising via a Hopf bifurcation, (iii) an external resistance in series with the working electrode giving rise to a linear global coupling and (iv) a nonlinear global coupling being suspected to be caused by a cut-off of the total current due to a limitation of charge carriers. A general model capturing these features is given by a complex Ginzburg-Landau equation with a nonlinear global coupling [13, 15]. Simulations of this MCGLE yield a huge variety of different patterns. We presented two types of cluster patterns, the amplitude clusters and the modulated amplitude clusters, which both undergoe a symmetry-breaking transition towards two different types of chimera states.

We demonstrated that type II dynamics describe experimental patterns very well. In both, the experiments and the simulations, we found modulated amplitude clusters, subclustering, chimera states and turbulence. Chimera states and turbulence show the best agreement, while there are some differences between experiment and theory in case of modulated amplitude clusters and subclustering. In the experiment, the second frequency in the modulated amplitude clusters (for the case of two-phase clusters) is always given by approximately half the frequency of the mean-field oscillation. This strongly suggests a period-doubling bifurcation being the reason of this second frequency. In contrast, in the MCGLE the modulated amplitude clusters seem to arise via a secondary Hopf bifurcation, giving rise to a continuously tunable second frequency. Also in the case of subclustering we find differences between experiment and simulation. In the experiments it seems that a demixing process takes place, spatially separating the modulational oscillation of the modulated amplitude clusters from the mean-field oscillation. The part with the modulational oscillations exhibits the clustering and therefore this part of the system then constitutes the region with the substructure, while the other part oscillates uniformly. Contrarily, the simulations suggest a period-doubling bifurcation for the mechanism yielding the subclustering,

as the two-phase subclusters oscillate at half the frequency of the modulational oscillations. However, the overall experimental dynamics are captured very well with this general ansatz, which describes only the essential features of the experiment, but not the detailed physical mechanisms behind the osclllations and pattern formation.

The theory shows even further interesting dynamics. We discussed alternating chimera states, where the synchronized and desynchronized regions interchange their state repeatedly [108]. These alternations occur rather irregularly at early times, but become more and more periodic at later times, when the boundary between the two phases tends to become straight.

Finally, we depicted simulation results showing so-called localized turbulence [107]. In this state, turbulent spots spread through the system, by means of circular lines of very small amplitude, expanding and breaking down. This dynamics raises the question of a robust definition of chimera states, since in localized turbulence one also observes a coexistence of synchrony and incoherence. However, we argue that a phase boundary between the synchronized and incoherent regions is crucial. Nevertheless, further research in this direction is needed.

3.8.1 Clusters

The common notion of phase clusters describes a state, where the oscillatory medium separates into several parts. The oscillations in the different parts are phase shifted with respect to each other [11, 109–112]. Each phase cluster can be described as a point rotating on a circle. In the most simple case the clusters are arranged symmetrically on this circle and therefore, the phase shifts in case of n clusters amount to $2\pi m/n$ [111–113], where $m = 1, 2, \ldots, n-1$. Typically, in the case of cluster patterns the dynamics can be reduced to a phase model [113]. However, there exist a second type of clusters, where essential variations in the amplitudes are present, called type II clusters [13, 15, 97]. We demonstrated that this second type of cluster patterns naturally arises in our experiments and can be reproduced with the MCGLE.

Now, we clarify, how such clustering can occur and why it is possible in the MCGLE. In what follows we consider clusters, where the two groups are in anti-phase configuration, at least in some reference frame. Note that in the CGLE, Eq. (3.3), the cluster patterns we consider cannot emerge, since the dynamics are invariant under a phase shift $W \to e^{i\chi}W$, for arbitrary χ and no terms are present to break the symmetry. For such clustering to occur this symmetry has to be broken [49]. This becomes clear when considering two-phase clusters with phase balance, i.e., both clusters have the same size. Then, if W_1 is a solution, a rotation by π, $W_1 e^{i\pi}$, yields the second solution, while a rotation by an arbitrary angle $\alpha \neq \pi$ does not yield a solution.

Thus, the general equation can be reduced to a form that describes cluster solutions only and therefore, prossesses only the discrete symmetry. In terms of the complex order parameter W this means that the dynamical equations are only invariant under the discrete transformation

$$W \quad \to \quad e^{i\pi}W\,.$$

In general, for n clusters, one needs that the equations are invariant under the discrete symmetry [49]

$$W \quad \rightarrow \quad e^{i2\pi/n} W \, .$$

To account for this symmetry the proper extension of the CGLE is given by the term $\gamma_n W^{*n-1}$, describing also an external resonant forcing [49, 75, 76, 111, 112, 114–118], see also Chapter 2. The asterisk denotes complex conjugation.

We will see that such a symmetry breaking term is intrinsically present in the MCGLE. Therefore, we write $W = W_0(1+w)$ for the complex amplitude in Eq. (3.4). By exploiting the conservation law, Eq. (3.6), and the resulting fact that $\langle w \rangle = \langle w^* \rangle = 0$, one obtains again a CGLE, now for the inhomogeneity w, which reads [15]

$$\partial_t w = (\mu + i\beta) w + (1 + ic_1)\nabla^2 w - (1 + ic_2)\eta^2 (|w|^2 w + w^*) + C \, , \tag{3.14}$$

where

$$C = (1 + ic_2)\eta^2 \left[\left\langle 2|w|^2 + w^2 + |w|^2 w \right\rangle - \left(2|w|^2 + w^2 \right) \right]$$

and $\mu = 1 - 2\eta^2$, $\beta = \nu - 2c_2\eta^2$. Here, the necessary symmetry-breaking term $-(1+ic_2)\eta^2 w^*$ occurs. But note that this term does not arise from the nonlinear global coupling. It would be present also when considering the CGLE, Eq. (3.3), without additional couplings. Crucial are the terms in C proportional to $|w|^2$ and w^2. As long as they are present, the equation is not symmetric with respect to the transformation $w \rightarrow e^{i\psi} w$ for any ψ. Here, the nonlinear global coupling comes into play, as it renders a vanishing C possible via the term proportional to $\left\langle 2|w|^2 + w^2 \right\rangle$. To show this, we assume a two-cluster state, where the two regions are described by solutions w_1 and w_2 in anti-phase, i.e., $w_1 = R\exp(i\phi)$ and $w_2 = R\exp(i(\phi + \pi))$. Then,

$$\begin{aligned} |w_1|^2 = |w_2|^2 = R^2 = \langle |w| \rangle \\ w_1^2 = w_2^2 = R^2 \exp\left(i2\phi\right) = \left\langle w^2 \right\rangle \, . \end{aligned}$$

Furthermore, since $|w_1|^2 w_1 = R^3 \exp(i\phi)$ and $|w_2|^2 w_2 = -R^3 \exp(i\phi) = -|w_1|^2 w_1$, also the nonlinear average vanishes, i.e., $\left\langle |w|^2 w \right\rangle = 0$. In essence, in case of a two-cluster state, the term C vanishes.

In turn, for $C = 0$, the occurrence of phase-balanced clusters is possible, since then the equation is symmetric with respect to the discrete symmetry $w \rightarrow e^{i\pi} w$. Then, it describes the subclass of phase-balanced two-cluster solutions. Note that this is impossible for a solely linear global coupling and that in case of clusters of different size these symmetry considerations do not hold.

Cluster solutions of Eq. (3.14) are then characterized by uniform regions, corresponding to different uniform solutions, with phase shifts to each other, as we already assumed above. Each of these solutions describes one cluster. As they are homogeneous, for such solutions the diffusional coupling vanishes and one obtains

$$\partial_t w_A = (\mu + i\beta) w_A - (1 + ic_2)\eta^2 (|w_A|^2 w_A + w_A^*) + C \, ,$$

where the subscript A indicates that this is the solution for one part of the system. At the borders between such regions, the diffusional coupling is active. In Section 4.2 we will encounter this equation again, when making the ansatz of two groups of equal size, leading to $C = 0$, in an ensemble of Stuart-Landau oscillators with the nonlinear global coupling of the MCGLE, i.e., the MCGLE without diffusional coupling. The two groups represent the two clusters. Then, we perform a bifurcation analysis of these two-cluster solutions. We will see that the results of this analysis can be transferred to the two-cluster solutions in the MCGLE without any restrictions.

3.8.2 Chimera states

Chimera states were mostly found in systems with nonlocal coupling. Typically, in these systems the synchronized state coexists with the chimera state and is stable. This bistability makes the observation rather difficult, as in many cases very special initial conditions have to be used, otherwise all oscillators would simply synchronize. However, there are a few examples, where they arise spontaneously (in some cases the synchronized solution is also unstable), see, e.g., Refs. [25, 29, 34]. Concerning the mechanisms of their emergence in nonlocally coupled systems only very little is known. Bifurcation analysis revealed that they can emerge via a saddle-node bifurcation [17, 23, 26, 36], and they were found in maps with coupling-induced bistability [27]. First analytical studies aiming to analyze the stability and to characterize the emergence and dynamics of chimera states in nonlocally coupled systems in a general way are presented in Refs. [36, 37].

Under global coupling, chimera states exhibit different properties. In our system, the synchronized state is unstable in the parameter region, where chimera states could be found. As a consequence, they form always spontaneously from random initial conditions. However, there is an additional prerequisite in globally coupled systems that is not present in nonlocally coupled ones: the system has to split into two well-defined groups that are separated in phase space. Only then, the symmetry of the system can be broken and the groups can behave differently. Both types of chimera states presented in this thesis occur in the vicinity of cluster states. Thus, the clustering mechanism seems to be responsible for the separation into groups. We will investigate this point in detail in the next chapter. This would be an example of a dynamically induced bistability, also encountered in Refs. [99, 119]. One can also choose a system composed of already bistable units [119] or split the ensemble of oscillators into two groups artificially, by setting up two groups with different intra- and inter-group coupling strengths [23, 31]. In fact, the type II chimeras seem to be related to the chimera states found with the two groups with different intra- and inter-group coupling, as the same situation arises dynamically. We discussed that point in Section 3.4.

Under nonlocal coupling one can observe also a type of chimera state that is different to the original chimera state described by Kuramoto & Battogtokh [16]. Considering coupled logistic maps, one finds a chimera state, where the incoherent part is periodic, i.e., frequency locked [27, 28]. Thus, this chimera state is only spatially incoherent,

exhibiting a profile with coherent and incoherent parts that oscillates periodically. The same behavior was also found in Ref. [22]. In contrast, in nonlocally coupled systems one typically finds a distribution of mean frequencies in the incoherent part of the chimera state [16].

First experimental observations of chimera states were achieved in an experimental realization of the two-groups system with different intra- and inter-group coupling [31] and a realization of the coupled-map lattice [32]. The two-groups system was realized using an ensemble of photosensitive Belousov-Zhabotinsky particles. Due to the photosensitivity of the reaction, the feedback could be implemented via illumination controlled by a computer to obtain the desired coupling. As already discussed, this type of chimera state shares properties with the type II chimeras found in the MCGLE and therefore also with the chimeras found during the photoelectrodissolution of n-type silicon. The same setup was used later to investigate a typical nonlocal coupling [29]. The realization of a coupled-map lattice was achieved by controlling the polarization properties of an optical wavefront with a liquid-crystal spatial light modulator. In this experiment, the coupling is also implemented using a computer [32]. Thus, these experiments have in common that they need external control to obtain the desired coupling function, which is not the case in the experiments described in the present thesis.

Furthermore, there are other experiments that do not incorporate an external control. The first example is by Martens *et al.*, who built up the two-groups model with two sets of metronomes [33]. As we will see in the next chapter, the dynamics of the chimera state they describe and the surrounding states are similar to the case of type I chimeras. The second example of experimental chimeras without control from outside is a network of electrochemical oscillators, where the discrete units exhibit the oscillatory dissolution of nickel wires and are coupled via a resistance network [34]. The introduction of a delay in this system is possible by implementing also capacitances. In this experiment, the chimera states form also spontaneously. Incoherent oscillators display phase-slipping behavior, i.e., their motion is very slow in the vicinity of the synchronized group, followed by relatively fast 2π phase slips. Type II chimeras exhibit similar behavior.

3.8.3 Open questions

Our analysis of spatio-temporal dynamics found in the MCGLE including the two types of chimera states still leaves some questions open. Both chimeras inherit properties from the cluster states in which they originate. Type I chimeras are created coming from amplitude clusters and consequently, the synchronized and the incoherent group are also separated by an amplitude difference, while the phase difference stays small. All oscillators exhibit one dominant time scale, which is the period of the mean-field oscillation. In contrast, type II chimeras stem from the modulated amplitude clusters and hence, exhibit a second characteristic time scale, which is the clustering frequency. This connection to the cluster states has to be investigated in more detail. Furthermore, we did not unravel the bifurcations leading to the cluster states yet.

Modulated amplitude clusters seem to be created in a secondary Hopf bifurcation as the frequency of modulational oscillations can be tuned continuously. This has to be shown rigorously, enabling one to approximate the cluster frequency with the corresponding Hopf frequency. However, a bifurcation analysis of a spatially extended system is not straightforward to perform.

To overcome this issue and address the above mentioned questions, we will reduce the spatially extended MCGLE to a discrete ensemble of Stuart-Landau oscillators with nonlinear global coupling. This is simply done by omitting the diffusional coupling in the MCGLE and will be the topic of the next chapter.

Chapter 4

Stuart-Landau oscillators with nonlinear global coupling

Das Ziel der Wissenschaft ist es immer gewesen, die Komplexität der Welt auf simple Regeln zu reduzieren.

(Benoît Mandelbrot)

4.1 Motivation

In the preceding chapter we presented quite complex spatio-temporal patterns found in numerical simulations of a modified complex Ginzburg-Landau equation with nonlinear global coupling. We successively compared the results to patterns forming in the oxide-layer thickness during the photoelectrodissolution of n-type silicon. So far, we could only provide a qualitative description of the dynamics, a detailed investigation of their creation in terms of a bifurcation analysis was unfeasible in the extended system, due to the high number of degrees of freedom. Now, we make the hypothesis that the diffusional coupling leads only to the spatial arrangement of the patterns, at least for a subset of patterns. In the next chapter, we will demonstrate that this is a reasonable assumption. Of course, there are patterns, where the diffusional coupling plays an important role in the overall dynamics, an example is localized turbulence, which seems to depend on the diffusional spreading of turbulence. However, for some patterns it is a correct assumption, and, therefore, we drop the diffusive term in the MCGLE, Eq. (3.4), and investigate N Stuart-Landau oscillators coupled via a nonlinear global coupling:

$$\frac{\mathrm{d}}{\mathrm{d}t} W_k = W_k - (1+ic_2)\,|W_k|^2\,W_k - (1+iv)\,\langle W\rangle + (1+ic_2)\left\langle |W|^2\,W\right\rangle , \quad k = 1,2,\ldots,N\,. \tag{4.1}$$

Here $\langle\cdots\rangle$ describes the arithmetic mean over the oscillator population, i.e., $\langle W\rangle = \sum_{k=1}^{N} W_k/N$. Taking the average of the whole equation yields for the dynamics of the

mean value

$$\frac{\mathrm{d}}{\mathrm{d}t}\langle W\rangle = -i\nu\langle W\rangle \quad \Rightarrow \quad \langle W\rangle = \eta e^{-i\nu t}\,. \tag{4.2}$$

Again, the dynamics exhibit a preserved and harmonic mean-field oscillation, which is important as it constitutes a relevant feature of the MCGLE and of the experiments.

In the next section we will investigate cluster solutions in this ensemble of Stuart-Landau oscillators and reveal the underlying bifurcations leading to their formation. As we can identify the cluster solutions with cluster patterns in the extended system, the results apply also to the patterns found in the MCGLE. Subsequently, we present two types of chimera states found in Eqs. (4.1) and investigate their relation to the cluster patterns. It turns out that the clustering mechanism constitutes the first symmetry-breaking step rendering the formation of chimera states possible. Again, the connection to the spatio-temporal patterns in the MCGLE is discussed.

4.2 Two-cluster solutions in an ensemble of generic limit-cycle oscillators with periodic self-forcing via the mean-field

Cluster formation is a well known phenomenon in systems of coupled oscillators. It arises in discrete systems of individual units [19, 113, 120] and in spatially extended oscillatory media [11, 109–112]. The common property of clusters in these systems is that the oscillators separate into distinct groups having the same properties within. The oscillations in the different groups are then phase shifted with respect to each other. In the symmetrical phase cluster state, the phase shifts for n clusters are given by $2\pi m/n$ [111–113], where $m = 1, 2, \ldots, n-1$.

As we will see in this section, the nonlinear global coupling leads to two-cluster soltuions, i.e., solutions with two groups, exhibiting more complex than simple periodic dynamics. In many cases the amplitude variations in cluster states are very small and the dynamics can be approximated by phase models. However, in some solutions we observe here, essential variations in the amplitude occur. In this state the clusters are a modulation of a homogeneous oscillation, as visible in Fig. 4.1a. Such dynamics, which were also called type II clusters [97], have been described also in Refs. [13, 15, 97, 121].

The nonlinear global coupling in Eqs. (4.1) leads to a conserved periodic mean-field oscillation that acts back on the individual oscillators as a forcing. We will see that this indeed leads to a so-called Arnold tongue, a tongue-shaped region in which oscillations are entrained to the driving. Reducing the full set of equations to two effective equations, we describe the case of clustering with two groups. We show that we end up with an equation possessing the same (symmetry) properties as the resonantly forced CGLE near a 2:1 resonance [114], which also exhibits cluster formation [76]. For details on this equation, see Section 2.3. The special symmetry leads to a very complex bifurcation diagram and therefore to a wide variety of different dynamical states, in line with results on periodically forced oscillators near a 2:1 resonance [122, 123], with

one exception: inside the locking region we observe a 1:1 entrainment, despite the bifurcation structure of a 2:1 resonance.

Equations (4.1) are equivariant to the direct product $\mathbf{S}_N \times S^1$ of the symmetry group $\mathbf{S}_N$ of permutations of N elements and the circle group S^1, describing the global phase invariance. The equivariance to $\mathbf{S}_N$ is obvious, as a permutation of indices in Eqs. (4.1) leaves the whole set of equations invariant. Nevertheless, particular solutions are not required to possess the full $\mathbf{S}_N \times S^1$ symmetry, only all solutions together exhibit it [124]. This consideration will help us later identifying the bifurcations that are possible to occur in the system.

We numerically solved Eqs. (4.1) using an implicit Adams method with timestep $dt = 0.01$ for $N = 1000$ oscillators, starting from random initial conditions on the real axis fulfilling the conservation law; see also Chapter 2. For certain parameter regimes the whole population divides into two subgroups of sizes N_1 and N_2 with $N_1 + N_2 = N$. Thus, the full symmetry is reduced to $\mathbf{S}_{N_1} \times \mathbf{S}_{N_2} \times S^1 \subseteq \mathbf{S}_N \times S^1$. For $\eta > 0$ one then observes modulated amplitude and amplitude clusters as shown in Figs. 4.1a and b, respectively. These cluster dynamics are the most commonly oberserved coherent solutions.

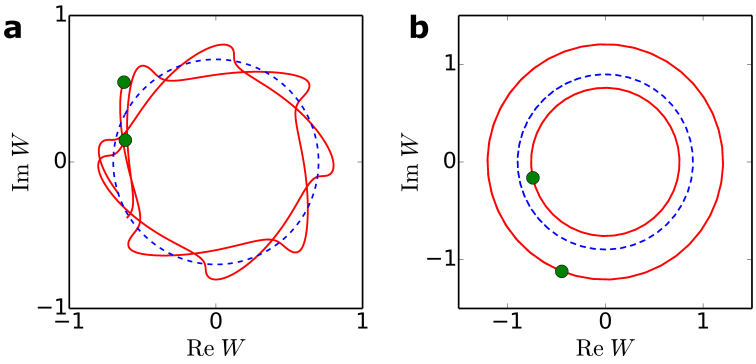

Figure 4.1: Cluster dynamics in the Stuart-Landau ensemble. Solid lines describe the trajectories of individual oscillators and dots mark their positions in a snapshot. Dashed lines describe the oscillation of the mean-field $\langle W \rangle$. (a) Modulated amplitude clusters for $c_2 = -0.6$, $\nu = 0.1$ and $\eta = 0.7$. Here, the subgroups perform additional oscillations around their mean-field $\eta \exp(-i\nu t)$ given in Eq. (4.2). (b) Amplitude clusters for $c_2 = -0.6$, $\nu = -1.5$ and $\eta = 0.9$. The main differences between the two groups are the different radii of their respective limit cycles. The phase shift is much smaller than π.

In the modulated amplitude cluster state the subgroups oscillate, in addition to the mean-field oscillation (shown as a blue dashed line), around their mean field. This leads to a repeated passing by each other of the subgroups in the complex plane. Similar states were observed in continuous systems in Refs. [13, 15, 97, 109, 121, 125]. In the amplitude cluster state the two groups oscillate on different limit cycles separated by an amplitude difference, while the phase shift is much smaller than π [98]. In the next section, in order to treat these solutions mathematically, we reduce the full set of N

equations in Eqs. (4.1) to two effective equations modelling the two subgroups.

4.2.1 Modulated amplitude clusters in the two-groups reduction

We will now focus on modulated amplitude clusters as presented in Fig. 4.1a. As visible in the figure, the ensemble splits into two groups, each performing amplitude-modulated oscillations in the complex plane. To analyze these dynamics, we reduce the N equations of the Stuart-Landau ensemble, Eqs. (4.1), to two effective equations. Therefore, we assume two groups W_1 and W_2, each synchronized, with sizes N_1 and N_2, respectively. The average over the entire ensemble is then given by

$$\langle W \rangle = \frac{1}{N} \left(N_1 W_1 + N_2 W_2 \right) ,$$

and analogously for $\left\langle |W|^2 W \right\rangle$. Inserting these expressions into Eqs. (4.1) results in

$$\begin{aligned} \frac{\mathrm{d}}{\mathrm{d}t} W_1 = &\left(1 - (1 + i\nu) \frac{N_1}{N} \right) W_1 \\ &- (1 + ic_2) \left(1 - \frac{N_1}{N} \right) |W_1|^2 W_1 \\ &- (1 + i\nu) \frac{N_2}{N} W_2 + (1 + ic_2) \frac{N_2}{N} |W_2|^2 W_2 , \end{aligned} \tag{4.3}$$

where the same holds for W_2 with indices 1 and 2 interchanged. Thus, we reduced the set of N equations to two effective equations and can now perform a linear stability analysis of the synchronized state. By setting $W_1 = W_2$ we obtain

$$\frac{\mathrm{d}}{\mathrm{d}t} W_1 = \frac{\mathrm{d}}{\mathrm{d}t} W_2 = -i\nu W_1 = -i\nu W_2 ,$$

and thus

$$W_1 = W_2 = \eta e^{-i\nu t} = W_0 ,$$

as expected. Since the conservation law, Eq. (4.2), still has to be fulfilled, the synchronized solution is given by W_0. We define deviations w_1 and w_2 from W_0 via $W_1 = W_0(1 + w_1)$ and $W_2 = W_0(1 + w_2)$. To fulfill the conservation law,

$$\frac{1}{N} \left(N_1 w_1 + N_2 w_2 \right) = 0 \tag{4.4}$$

holds. Inserting the definitions of w_1 and w_2 in Eq. (4.3), one obtains

$$\begin{aligned} \frac{\mathrm{d}}{\mathrm{d}t} w_1 = (1 + i\nu) \frac{N_2}{N} (w_1 - w_2) - (1 + ic_2) \frac{N_2}{N} \eta^2 \Big(&2(w_1 - w_2) + w_1^* - w_2^* + w_1^2 - w_2^2 \\ &+ 2(|w_1|^2 - |w_2|^2) + |w_1|^2 w_1 - |w_2|^2 w_2 \Big) . \end{aligned}$$

The condition in Eq. (4.4) yields $w_2 = -N_1 w_1/N_2$ and thus

$$\begin{aligned}\frac{\mathrm{d}}{\mathrm{d}t}w_1 &= \left[1-2\eta^2+i\left(\nu-2c_2\eta^2\right)\right]w_1 \\ &\quad -(1+ic_2)\eta^2\left[w_1^* + \left(w_1^2+2|w_1|^2\right)\frac{1}{N}\left(\frac{N_2^2-N_1^2}{N_2}\right) + |w_1|^2 w_1 \frac{1}{N}\left(\frac{N_2^3+N_1^3}{N_2^2}\right)\right] \\ w_2 &= -\frac{N_1}{N_2}w_1\,.\end{aligned} \tag{4.5}$$

The above equations still depend on the group sizes N_1 and N_2. By considering symmetric cluster states with $N_1 = N_2 = N/2$ this dependence vanishes and we obtain

$$\begin{aligned}\frac{\mathrm{d}}{\mathrm{d}t}w_1 &= (\mu+i\beta)\,w_1 - (1+ic_2)\eta^2\left(|w_1|^2\,w_1 + w_1^*\right)\,, \\ w_2 &= -w_1\,,\end{aligned} \tag{4.6}$$

where $\mu = 1-2\eta^2$ and $\beta = \nu - 2c_2\eta^2$.

Note here already that now the equation for w_1 is a forced CGLE near a 2:1 resonance [114] without the diffusive coupling, which is a result of the self-forcing in the system. Remember also that we encountered this equation for w_1 with additional terms already in Section 3.8.1, when considering cluster solutions in the MCGLE (Eq. (3.4)) (the additional terms are reflected in the additional terms in Eq. (4.5) and the diffusive coupling). There, we stopped at this point, while now we analyze solutions and bifurcations.

The synchronized solution W_0 possesses the symmetry $\mathbf{S}_2 \times S^1$ in the present two-oscillators description. A bifurcation with emanating solution branches exhibiting the reduced symmetry S^1 (separation into two subgroups) has to have the following symmetry property: the sum of the two solutions $W_1 + W_2$ is required to possess the full symmetry $\mathbf{S}_2 \times S^1$ (W_1 is on one of the solution branches and W_2 on another). Therefore, the symmetry breaking parts w_1 and w_2 have to cancel each other, i.e., $w_1 = -w_2$. This symmetry condition is fulfilled by three types of bifurcations, namely the pitchfork, the Hopf and the period doubling bifurcations. The two new solution branches emanating from the bifurcations are phase shifted by π. For the pitchfork bifurcation this is illustrated as an example in Fig. 4.2. One group, here w_1 chooses the upper branch, while the other group, here w_2, then has to choose the lower branch.

We will see that we indeed find the Hopf and the pitchfork bifurcation in the following linear stability analysis of the synchronized state, which is given by $w_1 = w_2 = 0$, and in the next section. The linear stability of the synchronized state is determined by

$$\frac{\mathrm{d}}{\mathrm{d}t}\begin{pmatrix}w_1\\ w_1^*\end{pmatrix} = \begin{pmatrix}\mu+i\beta & -(1+ic_2)\eta^2\\ -(1-ic_2)\eta^2 & \mu-i\beta\end{pmatrix}\cdot\begin{pmatrix}w_1\\ w_1^*\end{pmatrix}\,.$$

The eigenvalues of the Jacobian matrix are given by

$$\lambda_\pm = 1-2\eta^2 \pm \sqrt{\eta^4\left(1-3c_2^2\right)+4\nu c_2\eta^2-\nu^2}\,. \tag{4.7}$$

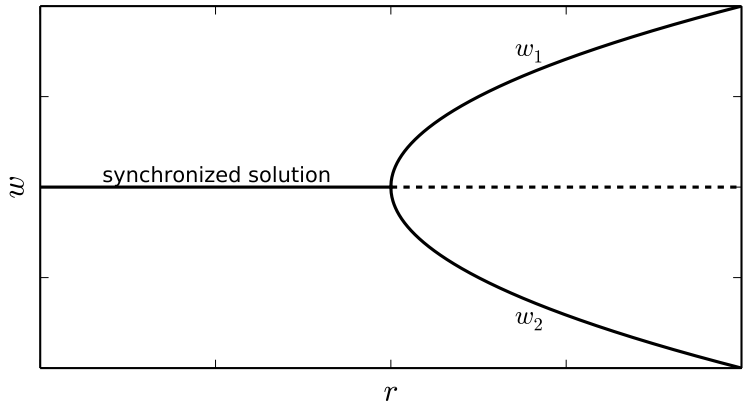

Figure 4.2: Schematic pitchfork bifurcation demonstrating the emergence of the two cluster solutions. r denotes an arbitrary parameter. Each group realizes one of the two stable branches created in the pitchfork. Exemplary shown is the first group w_1 realizing the upper branch and the second group w_2 realizing the π-rotated lower branch.

Thus, we find a secondary Hopf bifurcation in this system at $\eta = \eta_H = 1/\sqrt{2}$ for $\left(1 - 3c_2^2\right)/4 + 2\nu c_2 - \nu^2 < 0$. This Hopf bifurcation is the origin of the modulated amplitude clusters shown in Fig. 4.1a. In order to visualize this, we use the ansatz $W_k = W_0(1 + w_k)$ in the full system (Eqs. (4.1)) for the analysis of simulation results. For the modulated amplitude clusters shown in Fig. 4.3a, the dynamics of w_k are depicted in Fig. 4.3b.

One can clearly identify the two limit cycles of the two subgroups (blue solid lines) in Fig. 4.3b. The green dots mark a snapshot of the dynamics. In this reference frame the phase shift between the two groups is given by π. The two limit cycles are not identical, since the full system is divided into two groups with different sizes, i.e., $N_1 \neq N_2$. This results in different radii of the limit cycles in order to fulfill the condition in Eq. (4.4) and thus to fulfill the conservation law in Eq. (4.2). The red square marks the position of the synchronized solution. These observations confirm the result of the two-groups analysis that modulated amplitude clusters arise in a secondary Hopf bifurcation.

Using the eigenvalues in Eq. (4.7) we can determine the Hopf frequency ω_H to be

$$\omega_H = \mathrm{Im}\left(\sqrt{\eta^4\left(1 - 3c_2^2\right) + 4c_2\eta^2\nu - \nu^2}\right). \tag{4.8}$$

Next, we investigate the frequencies occurring in the dynamics in the original frame. Therefore, we calculate the cumulative power spectrum. To obtain this, one first has to Fourier transform all individual time series Re W_k of the oscillators and then average the resulting squared amplitudes $|a_k(\omega)|^2$, where k is the oscillator index. It is thus given by $S(\omega) = \left\langle |a(\omega)|^2 \right\rangle$. An exemplary cumulative power spectrum for the dynamics in the modulated amplitude cluster state (in the full system) is shown in Fig. 4.4 and it exhibits several peaks.

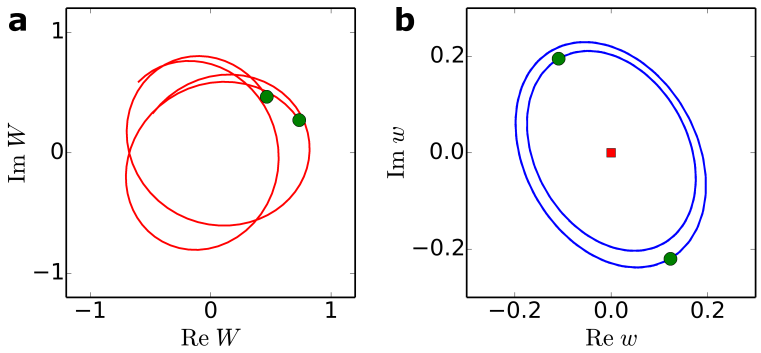

Figure 4.3: Emergence of modulated amplitude clusters in the full ensemble for $c_2 = -0.6$, $\nu = 1.2$ and $\eta = 0.7$. (a) Modulated amplitude clusters in the original frame. (b) Two limit cycles in antiphase and the fixed point at η (red square) in the rotating frame of w_k defined via $W_k = W_0(1 + w_k)$. The limit cycles have different radii as the whole population is divided into subgroups with $N_1 \neq N_2$.

The strongest peak is at the frequency ν of the mean-field oscillation. As we will show in what follows, the next two highest peaks are given by $\pm(\nu - \omega_H)$ and $\pm(\nu + \omega_H)$ as indicated by vertical lines in the figure.

In the vicinity of the Hopf bifurcation, the limit-cycle solution for w_1 in Eq. (4.6) is given by

$$w_1 = w_+^0 e^{i\omega_H t} + w_-^0 e^{-i\omega_H t} ,$$

where $w_\pm^0$ are complex-valued constants. In the original frame this results in

$$\begin{aligned} W_1 &= \eta e^{-i\nu t}\left(1 + w_+^0 e^{i\omega_H t} + w_-^0 e^{-i\omega_H t}\right) , \\ W_2 &= \eta e^{-i\nu t}\left(1 - w_+^0 e^{i\omega_H t} - w_-^0 e^{-i\omega_H t}\right) . \end{aligned}$$

Thus, we obtain frequency contributions in the cumulative power spectrum at

$$\begin{aligned} &\pm\nu \quad \left(\propto \eta^2\right) , \\ &\pm(\nu - \omega_H) \quad \left(\propto \left|\eta\omega_+^0\right|^2\right) , \\ &\pm(\nu + \omega_H) \quad \left(\propto \left|\eta\omega_-^0\right|^2\right) , \end{aligned} \tag{4.9}$$

as can be seen for the three major peaks in the power spectrum in Fig. 4.4. The other peaks are presumably given by higher resonances. Note that for a circular limit cycle ω_+^0 or ω_-^0 equals zero leading to vanishing contributions at $\pm(\nu - \omega_H)$ or $\pm(\nu + \omega_H)$, respectively.

To further check the validity of the frequencies, obtained via a reduction to two effective equations and via linear stability analysis, we compare them with the frequencies in the full system for several values of ν. The results for $|\nu + \omega_H|$ (blue, dashed) and

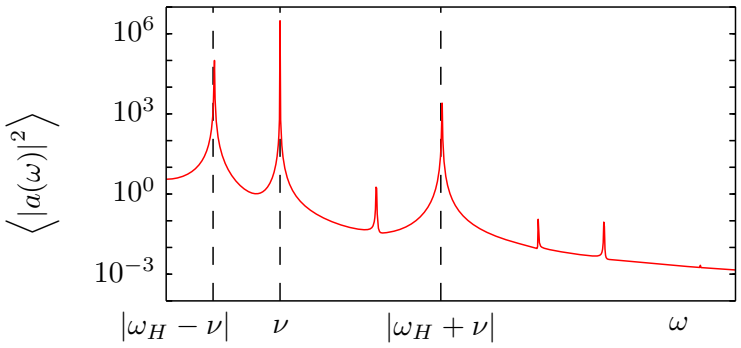

Figure 4.4: Cumulative power spectrum for the full system at parameter values $c_2 = -0.6$, $\nu = 1.2$, $\eta = 0.7$. The major peaks in this spectrum can be traced back to linear combinations of the Hopf frequency ω_H in Eq. (4.8) and the frequency of the mean-field oscillation ν as indicated by the vertical lines (see text and Eq. (4.9)).

$|\nu - \omega_H|$ (red, solid) are shown in Fig. 4.5a. In Fig. 4.5b we show the comparison for $|\nu - \omega_H|$ in more detail.

The simulation results shown are for $\eta = 0.7$, which is close to the value at the Hopf bifurcation $\eta_H = 1/\sqrt{2} \approx 0.707$. As visible in the figure, the results of the linear stability analysis (lines), Eqs. (4.9), reproduce the simulation results (symbols) very well. The nearly constant shift visible in Fig. 4.5b is due to the finite distance to the Hopf bifurcation.

We conclude that the modulated amplitude clusters arise through a Hopf bifurcation in the rotating frame with frequency ν, which gives rise to the amplitude modulations in the full system. The dynamics on the created limit cycle are in anti-phase as to fulfill the conservation law, which is also in line with our symmetry considerations above. Since the Hopf bifurcation occurs in the rotating frame, it is in fact a secondary Hopf bifurcation. The dynamics in the original frame is thus quasiperiodic. This is also obvious from the continuous frequency curves in Fig. 4.5.

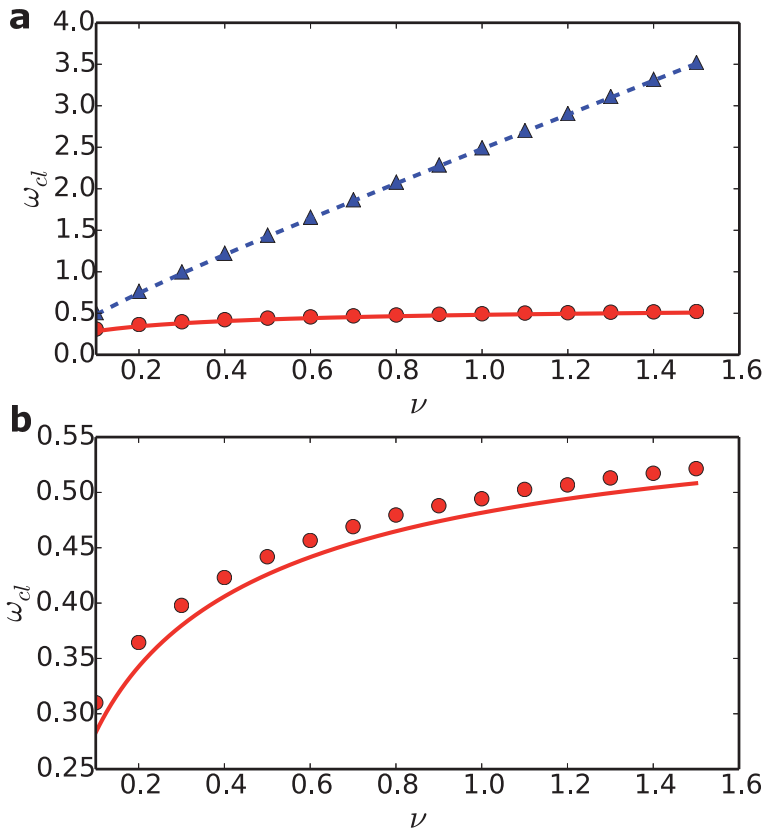

Figure 4.5: Comparison of the calculated peak frequencies with the frequencies in the full system for $c_2 = -0.6$ and $\eta = 0.7$. The Hopf bifurcation occurs at $\eta_H = 1/\sqrt{2}$. (a) Both frequencies $|\nu + \omega_H|$ in blue (dashed) and $|\nu - \omega_H|$ in red (solid) versus ν. Lines describe the results of the linear stability analysis, Eqs. (4.9), and symbols mark the simulation results. (b) Magnified ω_{cl}-axis, showing $|\nu - \omega_H|$ vs. ν in more detail.

4.2.2 Amplitude clusters in the two-groups reduction

The modulated amplitude clusters described in the preceding section arise for certain parameters through a Hopf bifurcation. This motion on a torus can be destroyed through a saddle-node bifurcation leading to the amplitude clusters shown in Fig. 4.1b. These amplitude clusters are solutions of Eq. (4.6) in the form $w_1 = R\exp(i\chi_\pm)$ [114], as this results in $|W_1| = \eta\sqrt{1+2R\cos\chi_\pm + R^2}$. With $\chi_+ = \chi_- + \pi$ the two solutions describe limit cycles with different radii. Inserting this ansatz into Eq. (4.6), separating real and imaginary parts and assuming $R \neq 0$ one obtains

$$\begin{aligned}\mu - \eta^2 R^2 - \eta^2\cos 2\chi - c_2\eta^2\sin 2\chi &= 0\,,\\ \beta - c_2\eta^2 R^2 - c_2\eta^2\cos 2\chi + \eta^2\sin 2\chi &= 0\,.\end{aligned}$$

This set of equations can be solved for R and χ and one finds two pairs of solutions [126, 127]:

$$\begin{aligned}R^{(1)} &= \sqrt{\frac{\mu + c_2\beta - \sqrt{\eta^4\left(1+c_2^2\right)^2 - (c_2-\nu)^2}}{\eta^2\left(1+c_2^2\right)}}\,,\\ \chi_-^{(1)} &= \frac{1}{2}\arcsin\left(\frac{c_2-\nu}{\eta^2\left(1+c_2^2\right)}\right),\\ \chi_+^{(1)} &= \chi_-^{(1)} + \pi\,,\end{aligned}$$

$$\begin{aligned}R^{(2)} &= \sqrt{\frac{\mu + c_2\beta + \sqrt{\eta^4\left(1+c_2^2\right)^2 - (c_2-\nu)^2}}{\eta^2\left(1+c_2^2\right)}}\,,\\ \chi_-^{(2)} &= \frac{\pi}{2} - \frac{1}{2}\arcsin\left(\frac{c_2-\nu}{\eta^2\left(1+c_2^2\right)}\right),\\ \chi_+^{(2)} &= \chi_-^{(2)} + \pi\,.\end{aligned}$$

We calculate the boundaries $\eta(c_2,\nu)$ of their existence and obtain:

$$\begin{aligned}&R^{(1)},\ \chi_\pm^{(1)} \text{ exists for } \eta > \eta_{SN}\ \&\ \eta < \eta_c\ \&\ \eta < \eta_P^-\,,\\ &R^{(2)},\ \chi_\pm^{(2)} \text{ exists for } \begin{cases}\eta > \eta_{SN}\,, & \text{for } \eta < \eta_c\,,\\ \eta_P^- < \eta < \eta_P^+\,, & \text{for } \eta > \eta_c\,.\end{cases}\end{aligned}$$

$\eta_{SN}(c_2, \nu)$, $\eta_c(c_2, \nu)$ and $\eta_P^{\pm}(c_2, \nu)$ are given by

$$\begin{aligned} \eta_{SN} &= \sqrt{\frac{|c_2 - \nu|}{1 + c_2^2}}\,, \\ \eta_c &= \sqrt{\frac{1 + c_2\nu}{2\left(1 + c_2^2\right)}}\,, \\ \eta_P^{\pm} &= \sqrt{\frac{2(1 + c_2\nu) \pm \sqrt{4(1 + c_2\nu)^2 - 3\left(1 + c_2^2\right)(1 + \nu^2)}}{3\left(1 + c_2^2\right)}}\,. \end{aligned} \tag{4.10}$$

Linear stability analysis reveals that the amplitude cluster solutions $R^{(1,2)} \exp\left(i\chi_{\pm}^{(1,2)}\right)$ arise as two saddle-node pairs at η_{SN}, thereby destroying the limit cycle of the modulated amplitude clusters in a saddle-node of infinite period bifurcation (sniper). Solutions (1) are saddles and solutions (2) are stable nodes. Note that at $\eta = \eta_{SN}$, $\chi_-^{(1)} = \chi_-^{(2)} = \pi/4$ and thus $\chi_+^{(1)} = \chi_+^{(2)} = 5\pi/4$ and furthermore, $R^{(1)} = R^{(2)}$. Both solutions (1) and (2) can be destroyed in pitchfork bifurcations with the synchronized solution ($\eta_P^{\pm}$). Note that η_c is not a bifurcation line. Below η_c the pitchfork involves $R^{(1)} \exp\left(i\chi_{\pm}^{(1)}\right)$ and above η_c it involves $R^{(2)} \exp\left(i\chi_{\pm}^{(2)}\right)$. Furthermore, the crossings of η_c and η_P^- mark degenerate pitchfork bifurcations. For details see the next section. In essence, the amplitude clusters emerge in a sniper bifurcation when coming from a parameter region, where the modulated amplitude clusters are stable. And they arise in a pitchfork bifurcation when coming from a parameter region, where the synchronized solution is stable (in a small region they also arise via a saddle-node bifurcation; see next section). A coarse bifurcation diagram is depicted in Fig. 4.6 with illustrations of the dynamical states along the path A to E given in Fig. 4.7.

The overall structure reminds of a so-called Arnold tongue and we will discuss the relation to the locking behavior of forced oscillatory media in Section 4.2.4. Inside the tongue one observes amplitude clusters. The tongue is bounded by a sniper bifurcation for small η values and by a pitchfork bifurcation for high η values. A Hopf bifurcation separates the region of modulated amplitude clusters from the region of stable synchronized solutions. To illustrate the different dynamical behaviors in the distinct regions, we go through the path A to E (for comparison see Fig. 4.7): Starting at A with the synchronized solution, the Hopf bifurcation creates the limit cycle for the modulated amplitude clusters in B. This limit cycle is then destroyed by the sniper bifurcation resulting in amplitude clusters in C. Approaching the outer pitchfork bifurcation brings the fixed points of the amplitude clusters closer together in D. Note that in the pitchfork between C and D the unstable solutions $R^{(1)} \exp\left(i\chi_{\pm}^{(1)}\right)$ meet the synchronized solution, thus the stable solutions $R^{(2)} \exp\left(i\chi_{\pm}^{(2)}\right)$ are unaffected by this pitchfork bifurcation. At the upper pitchfork the fixed points of the amplitude clusters merge with the synchronized solution with what we end up in E. Note that,

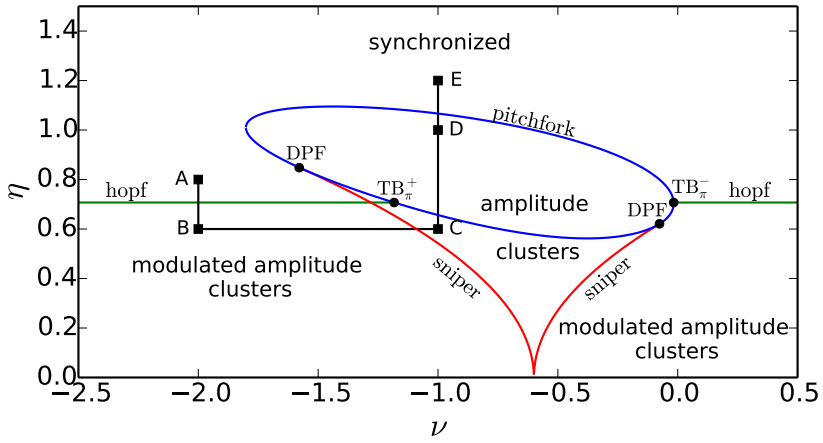

Figure 4.6: Coarse bifurcation diagram for the two-groups reduction. Shown is the amplitude η of the mean-field oscillation versus its frequency ν for fixed $c_2 = -0.6$. The stable dynamical states are indicated in the figure. The Hopf bifurcation (green) is given by $\eta = \eta_H$, the pitchfork (blue) is described by $\eta_P^\pm$ and the sniper (red) occurs at η_{SN}, see Eqs. (4.10). The dynamical states along the path A to E are depicted in Fig. 4.7. The codimension-two points are two Takens-Bogdanov points of π-rotational symmetry (TB$_\pi^\pm$) and two degenerate pitchfork bifurcations (DPF). The details of the bifurcation structure, which have been omitted here, including the unfoldings of the TB$_\pi^\pm$ points, will be discussed in Section 4.2.3.

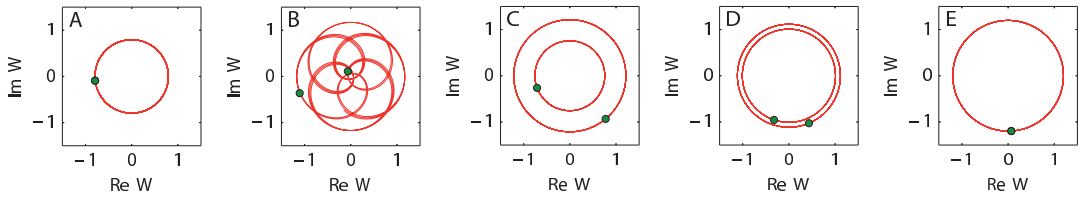

Figure 4.7: Simulation results for the two-groups reduction in the original frame illustrating the dynamical states along the path A-E in the bifurcation diagram in Fig. 4.6.

as $w_2 = -w_1$ in Eq. (4.6), both groups undergo the bifurcations simultaneously and the second group always realizes the π-rotated solution of the first group.

Furthermore we encounter three codimension-two bifurcations, namely a degenerate pitchfork (DPF) and two types of Takens-Bogdanov points TB$_\pi^\pm$. The unfoldings of the Takens-Bogdanov points are presented in the next Section. Note that due to the symmetry present in the system, the unfoldings are much more complicated than in the standard case.

This diagram is strictly valid only for the two-groups reduction. It clarifies, which bifurcations lead to the amplitude and modulated amplitude clusters. The diagram is applicable whenever the full ensemble is separated into two subgroups.

4.2.3 Details of the bifurcation diagram

The codimension-two bifurcations $TB^{\pm}_{\pi}$ present in the coarse bifurcation diagram in Fig. 4.6 have rather complex unfoldings. Using the software `AUTO-07P` for numerical continuation, we could identify the local and global bifurcations occurring around the $TB^{\pm}_{\pi}$ points. The unfolding of the plus case, TB^{+}_{π}, is shown schematically in Fig. 4.8, while the minus case, TB^{-}_{π}, is presented in Fig. 4.9. Sketches of corresponding phase portraits are also depicted in the figures.

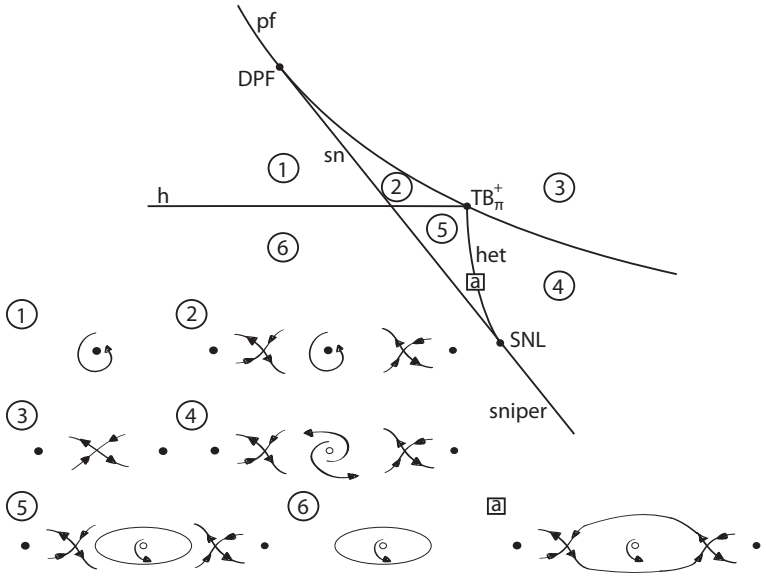

Figure 4.8: Sketch of the local bifurcation structure around the TB^{+}_{π} point with corresponding phase portraits. The involved codimension-one bifurcations are: pitchfork (pf), saddle-node (sn), Hopf (h), saddle-node of infinite period (sniper) and heteroclinic (het). The codimension-two bifurcations are: Takens-Bogdanov TB^{+}_{π}, degenerate pitchfork (DPF) and saddle-node loop (SNL). Stable fixed points are marked by filled circles and unstable ones by empty circles. Stable limit cycles are drawn with a solid line and unstable limit cycles with a dashed line.

In the TB^{+}_{π} point a pitchfork, a Hopf and a heteroclinic bifurcation meet. In our system, we find in the vicinity also a saddle-node bifurcation, which meets the pitchfork in a degenerate pitchfork bifurcation (DPF) and the heteroclinic in a saddle-node loop (SNL) bifurcation, see Fig. 4.8. The DPF turns the pitchfork from supercritical to subcritical and the TB^{+}_{π} changes it back to supercritical. The SNL turns the saddle-node into a saddle-node of infinite period (sniper).

When following the numbering in Fig. 4.8, we start with a stable focus (1), then cross the saddle-node, thereby creating two saddle node pairs (2). Then, we cross the subcritical pitchfork and end up in (3) with two stable nodes and a saddle. Next, we cross the pitchfork on the supercritical side, yielding two saddle node pairs with an unstable focus in between (4). Note that the foci that seem (from the figure) to

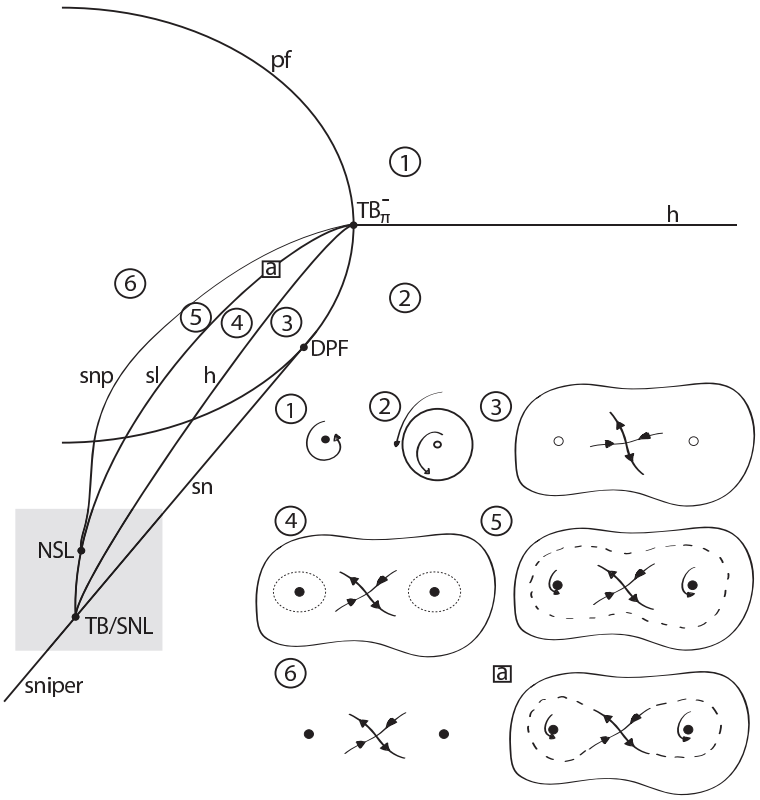

Figure 4.9: Sketch of the local bifurcation structure around the TB_π^- point with corresponding phase portraits. The involved codimension-one bifurcations are: pitchfork (pf), saddle-node (sn), Hopf (h), saddle-node of infinite period (sniper), saddle-loop (sl) and saddle-node of periodic orbits (snp). The codimension-two bifurcations are: Takens-Bogdanov with symmetry (TB_π^-) and without symmetry (TB), saddle-node loop (SNL), degenerate pitchfork (DPF) and neutral saddle-loop (NSL). Here, a TB and a SNL belonging to different solutions coincide, for details see text. Stable fixed points are marked by filled circles and unstable ones by empty circles. Stable limit cycles are drawn with a solid line and unstable limit cycles with a dashed line. Note that the bifurcation structure in the shaded box is not a result of the continuation as this diverges. It is consistent with the rest of the diagram, but there might be other bifurcations involved, see, e.g., Ref. [122].

be involved in the pitchfork bifurcations change to nodes just before the bifurcations occur. Crossing the heteroclinic bifurcation creates a stable limit cycle around the unstable focus in the center (5), which emerges from a double heteroclinic connection at the bifurcation (a). Finally, the saddle node pairs are annihilated in a saddle-node bifurcation and we are left with a stable limit cycle around an unstable focus in (6).

The local bifurcation structure around the TB_π^- point is more complex. In the TB_π^- point, a pitchfork, a Hopf concerning the synchronized solution, a Hopf concerning the amplitude cluster solutions, a saddle-loop and a saddle-node of periodic orbits (snp) meet. The saddle-loop line is in fact the coincidence of two saddle-loop bifurcations,

one which describes the saddle-loop bifurcation of the amplitude cluster solutions (small limit cycles in Fig. 4.9) and one which concerns the modulated amplitude cluster solutions (outer limit cycles in Fig. 4.9). With this, we can understand the codimension-two bifurcations occurring in the vicinity of the TB_π^- point: the snp and the two saddle-loops meet first in a neutral saddle-loop (NSL) and later the saddle-loops meet with the Hopf and the saddle-node in a Takens-Bogdanov (TB) without symmetry and a saddle-node loop (SNL). The saddle-loop corresponding to the amplitude cluster solution ends in the TB point and the other saddle-loop turns the saddle-node into a saddle-node of infinite period (sniper) at the SNL. Note that this region of the bifurcation diagram, i.e., the shaded region, is not a result of the continuation as this diverges. It is consistent with the rest of the diagram, but there might be other bifurcations involved, see, e.g., Ref. [122]. In the degenerate pitchfork (DPF) the saddle-node bifurcation meets the pitchfork.

Again we can go through the diagram step by step by following the numbering in Fig. 4.9: We start with a stable focus (1) and cross the Hopf to obtain a stable limit cycle around an unstable focus (2). Then, the subcritical pitchfork turns the unstable focus into a saddle point and creates two unstable nodes (3). The subcritical Hopf creates two unstable limit cycles (4), which form homoclinic loops when meeting the manifolds of the saddle point in the saddle-loop bifurcation (a). This saddle-loop bifurcation coincides with a saddle-loop bifurcation of an unstable modulated amplitude cluster solution, which is given by the unstable limit cycle in (5). Finally, the stable and the unstable limit cycle annihilate each other in a snp, and a pair of stable nodes (describing the amplitude cluster solutions) with a saddle point in between remain (6).

In fact the $\mathrm{TB}_\pi^\pm$ points are Takens-Bogdanov points of π-rotational or cubic symmetry [45, 128], see also Ref. [75]. This is the symmetry present in Eq. (4.6). They possess the same principal bifurcation structure as the second order resonance points found in the investigation of periodically forced oscillators [122]. However, some bifurcations are different, as we will discuss in the next section.

4.2.4 Conclusions

We could unravel the complex bifurcation structure exhibited by the two-cluster solutions of an ensemble of generic limit-cycle oscillators near a Hopf bifurcation. The conservation of the mean-field oscillation leads to mainly two bifurcations: a Hopf bifurcation yielding the modulated amplitude clusters and a pitchfork bifurcation resulting in common amplitude clusters. The meeting of these two gives rise to two Takens-Bogdanov points of π-rotational symmetry and therewith to a wide variety of dynamical states. We obtained these results for equal group sizes. Only in this case the special symmetry is present, since for $N_1 \neq N_2$ the unsymmetric contributions in Eq. (4.5) do not cancel. In the unsymmetric equation, the pitchfork, Hopf and period-doubling bifurcations should not be observable. However, the applicability of the results on dynamics with unequal group sizes suggests that also for $N_1 \neq N_2$ the clusters arise via the same bifurcations. The qualitative dynamics for $N_1 \neq N_2$ look the

same as for $N_1 = N_2$. Furthermore, we compared quantitatively the cluster frequencies in the full system with $N_1 \neq N_2$ to the prediction based on $N_1 = N_2$ and obtained very good agreement.

So far, we cannot predict, for which parameter values the full system spontaneously reduces to two groups. This is a question that should be addressed in future work.

The results of the bifurcation analysis apply directly to the spatio-temporal patterns found in the MCGLE in Chapter 3, thereby explaining the origins of the spatially extended modulated amplitude and amplitude clusters. In Chapter 5, we will demonstrate that the dynamics of individual oscillators in the MCGLE are perfectly described by the Stuart-Landau oscillators considered here, for the discussed cluster solutions.

Besides, there is a strong connection to resonantly forced oscillatory media [49, 75, 76, 111, 112, 114–118]. The symmetry properties of the reduced dynamics in Eq. (4.6), namely the cubic and π-rotational symmetries, are also present in the complex Ginzburg-Landau equation (CGLE) with resonant forcing near a 2:1 resonance. In fact, there is a linear transformation that transforms the equation for w_1 in Eq. (4.6) to the form given in, e.g., Ref. [114] (see Eq. (10) therein) of the resonantly forced CGLE, when omitting the diffusive coupling. As for forced oscillatory media, we observe an Arnold tongue, a region of frequency locking, in the bifurcation diagram in Fig. 4.6. The tongue starts at $\nu = c_2$, i.e., at a value of the driving frequency ν equal to the natural frequency c_2 of the Stuart-Landau oscillator. The locking region is bounded by the saddle-node, sniper and pitchfork bifurcations. The dynamics lock to the frequency ν of the mean-field oscillations, i.e., to the frequency of the driving. Thus, we observe a 1:1 locking instead of a 2:1 locking, which one would expect, since we observe the bifurcation structure of a 2:1 resonance. This is reflected in the occurrence of a pitchfork bifurcation instead of the period doubling bifurcation, which is present in the vicinity of a second order resonance point, see Ref. [122]. A schematic bifurcation diagram of a standard $p/2$ Arnold tongue (2:p locking) is shown in Fig. 4.10. The second order resonance points are denoted with $R_{2\pm}$ and correspond to the $\mathrm{TB}_\pi^\pm$ points in Fig. 4.6. The Hopf bifurcation in Fig. 4.6 and the Neimark-Sacker bifurcation in Fig. 4.10 are qualitatively the same, as the Neimark-Sacker is the discrete version of a Hopf bifurcation. In case of the second order resonance point one finds a saddle-node instead of a sniper bifurcation, i.e., the torus persists. Furthermore, to achieve the 2:p dynamics, a period-doubling bifurcation appears in Fig. 4.10 instead of the pitchfork in Fig. 4.6.

As in the forced CGLE, the locked solutions in our system do not lie on a torus, since the torus is destroyed in a sniper bifurcation. This can be easily seen, when considering the ansatz that we made. We investigated the dynamics of w_k defined via $W_k = W_0(1 + w_k)$. The sniper bifurcation that we found creates fixed points in w_k, namely $R^{(1,2)} \exp(i\chi_\pm^{(1,2)})$. Thus, $W_k = W_0(1 + R^{(1,2)} \exp(i\chi_\pm^{(1,2)}))$ exhibits only one timescale, which is given by the frequency ν of the mean-field oscillation. Therefore, the torus is destroyed.

In our system the forcing is in fact a self-forcing, as the dynamics produce a mean-field oscillation, which is conserved and then acts back as a forcing on the system. This

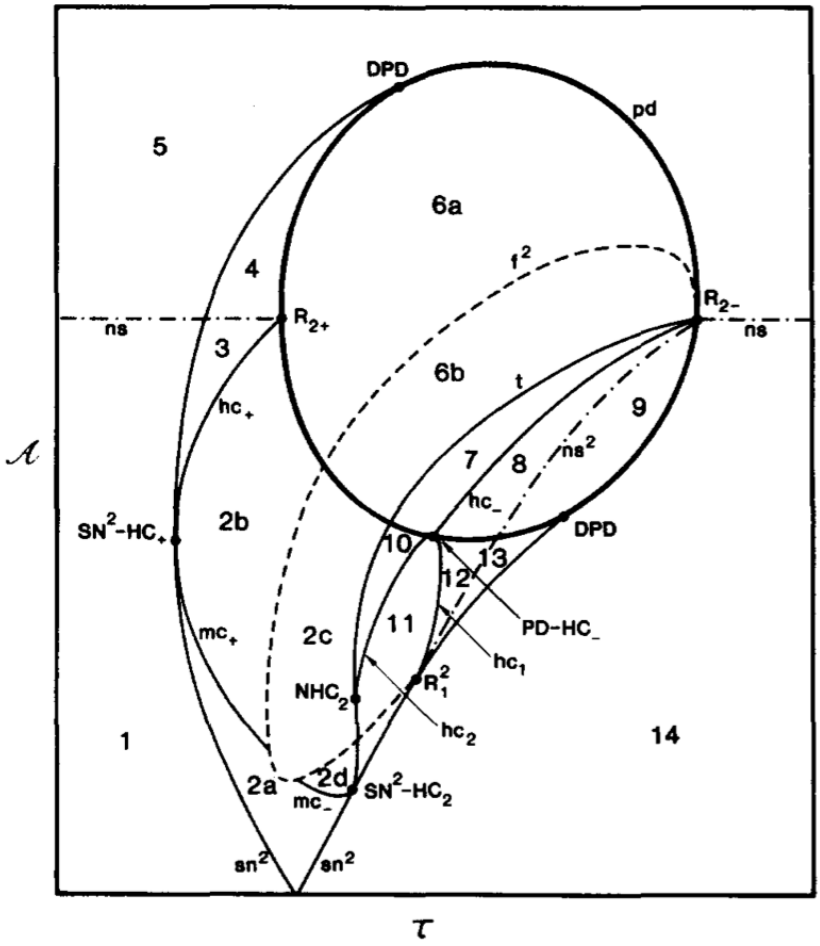

Figure 4.10: Schematic bifurcation diagram of a $p/2$ Arnold tongue (2:p locking) in the τ vs. $\mathcal{A}$ parameter plane. τ: normalized forcing period; $\mathcal{A}$: normalized forcing amplitude. The second order resonance points are marked by $R_{2\pm}$. Other bifurcations: sn: saddle-node; pd: period-doubling; ns: Neimark-Sacker; DPD: degenerate period doubling; hc: homoclinic connection; t: torus collision; a superscript n denotes the period, nT_{ext}, of an orbit. For more details see Ref. [122]. Reprinted with permission from W. Vance and J. Ross, *J. Chem. Phys.* **91** (12) 7654 (1989). Copyright 1989, AIP Publishing LLC.

self-forcing renders the cluster solutions possible. But note that it is the mathematical structure of a 2:1 resonance that is responsible for the cluster formation. We observe a 1:1 locking and in general this would not give rise to cluster formation.

4.3 Clustering as a prerequisite for chimera states in globally coupled systems

4.3.1 Introduction

In the introduction of this thesis, we outlined the story of chimeras in nonlinear dynamics. Quite a lot of studies deal with this topic, investigating different systems. However, concerning the prerequisites of their existence and the mechanisms of their emergence only very little is known. Bifurcation analysis revealed that they can emerge via a saddle-node bifurcation [17, 23, 26, 36], and they were found in maps with coupling-induced bistability [27]. First analytical studies aiming to analyze the stability and to characterize the emergence and dynamics of chimera states in nonlocally coupled systems in a general way are presented in Refs. [36, 37].

In this Section we argue that a clustering mechanism observed typically in globally coupled systems is a sufficient feature, rendering chimera states possible, as it splits the oscillators into several groups and yields at least bistability. Then, one of the two groups can desynchronize, while the other group stays coherent if the response on the coupling is effectively different in the two groups. In the present study we demonstrate that this situation can arise via nonlinear amplitude effects. Moreover, we show that different cluster states lead to different chimera states and that the chimera states inherit properties from the cluster states in which they originate.

4.3.2 Chimera states under nonlinear global coupling

We consider again the ensemble of $N = 1000$ Stuart-Landau oscillators with nonlinear global coupling in Eqs. (4.1). Again, we observe amplitude clusters and modulated amplitude clusters in Figs. 4.11a and f, respectively, as in the last section.

The cluster formation is the first symmetry-breaking step enabling the emergence of chimera states as it produces first of all two different groups. Indeed, in the vicinity of the two types of clusters we also observe two associated types of chimera states, as shown in Figs. 4.11b and e, respectively. The first type obviously inherited the property that the two groups are separated by an amplitude difference. Thus, starting from the amplitude cluster state, the group with the smaller radius got desynchronized. The second type of chimeras shares properties with the modulated amplitude clusters, but this will be discussed below, where it becomes more apparent. As we will demonstrate in Chapter 5, these chimera states are the discrete counterparts of the spatially extended type I and II chimeras of Chapter 3. Type I chimeras mediate between the cluster solution in Fig. 4.11a and the synchronized state in Fig. 4.11c. In contrast, type II chimeras bridge the gap between the cluster solution in Fig. 4.11f and completely irregular dynamics in Fig. 4.11d.

To gain a better understanding of the temporal dynamics in the chimera states, we depict $|W_k|$ and Re W_k versus time for type I and II chimeras in Figs. 4.12(a,b) and (d,e), respectively. The synchronized group is marked with red color and the

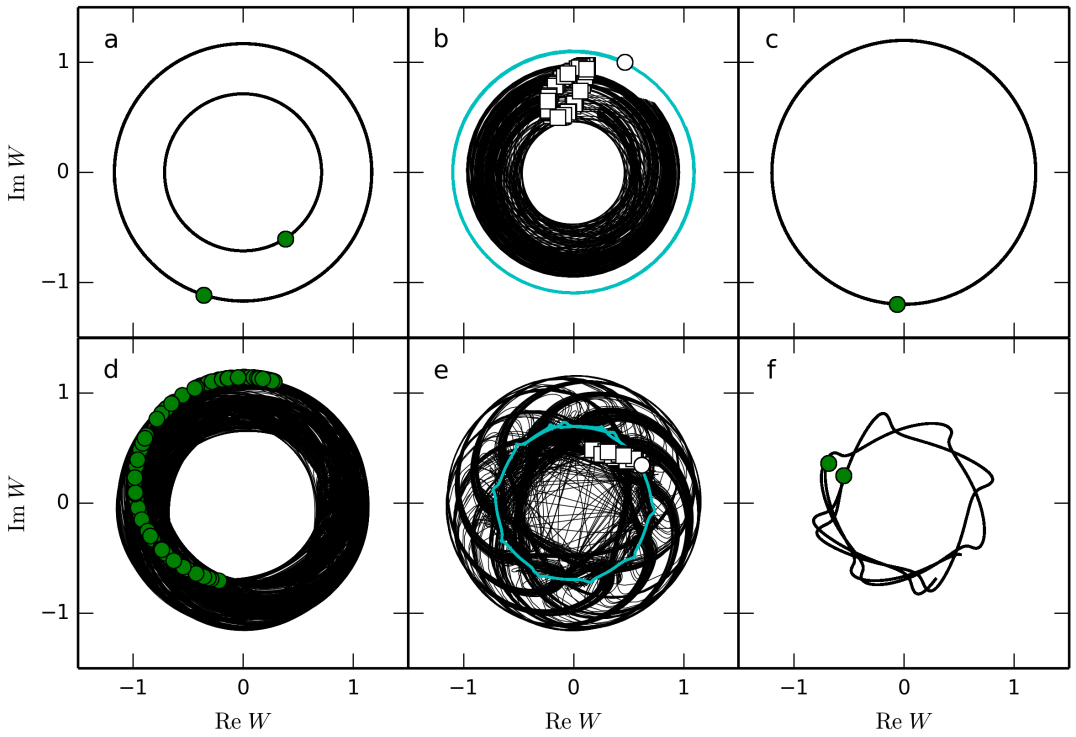

Figure 4.11: Evolutions in the complex plane and snapshots. Trajectories of the oscillators are shown as solid lines, whereas the symbols describe snapshots of the system. First row: type I dynamics. (a) Amplitude clusters ($\eta = 0.9$). (b) Type I chimera ($\eta = 1.02$), black lines and squares: incoherent group; cyan (gray) lines and circles: coherent group. (c) Complete synchronization ($\eta = 1.2$). Other parameters: $c_2 = 0.58$ and $\nu = 1.49$. Second row: type II dynamics. (d) Irregular dynamics ($\nu = -0.1$). (e) Type II chimera ($\nu = 0.02$), black lines and squares: incoherent group; cyan (gray) lines and circles: coherent group. (f) Modulated amplitude clusters ($\nu = 0.1$). Other parameters: $c_2 = -0.6$, $\eta = 0.7$.

incoherent group is plotted in blue. In the type I chimera there is a clear separation of the groups by an amplitude difference. The coherent group has an approximately constant amplitude, while the oscillators in the incoherent group exhibit irregular amplitude fluctuations. This is reflected in the real part, showing an approximately harmonically oscillating synchronized group. The incoherent group oscillates with the same main frequency, but forms a band of oscillators due to the irregularity in the modulus. This state is in fact unstable, as we observe heteroclinic transitions between the type I chimera and two other cluster states on a large timescale. This will be discussed below. In contrast, the second type of chimeras seems to be stable, as we could not observe a break down in the simulations up to $T = 1 \cdot 10^6$. The incoherent oscillators in this type II chimera show a nearly-periodic spiking behavior (which is not performed by all incoherent oscillators at the same time). This is a property inherited

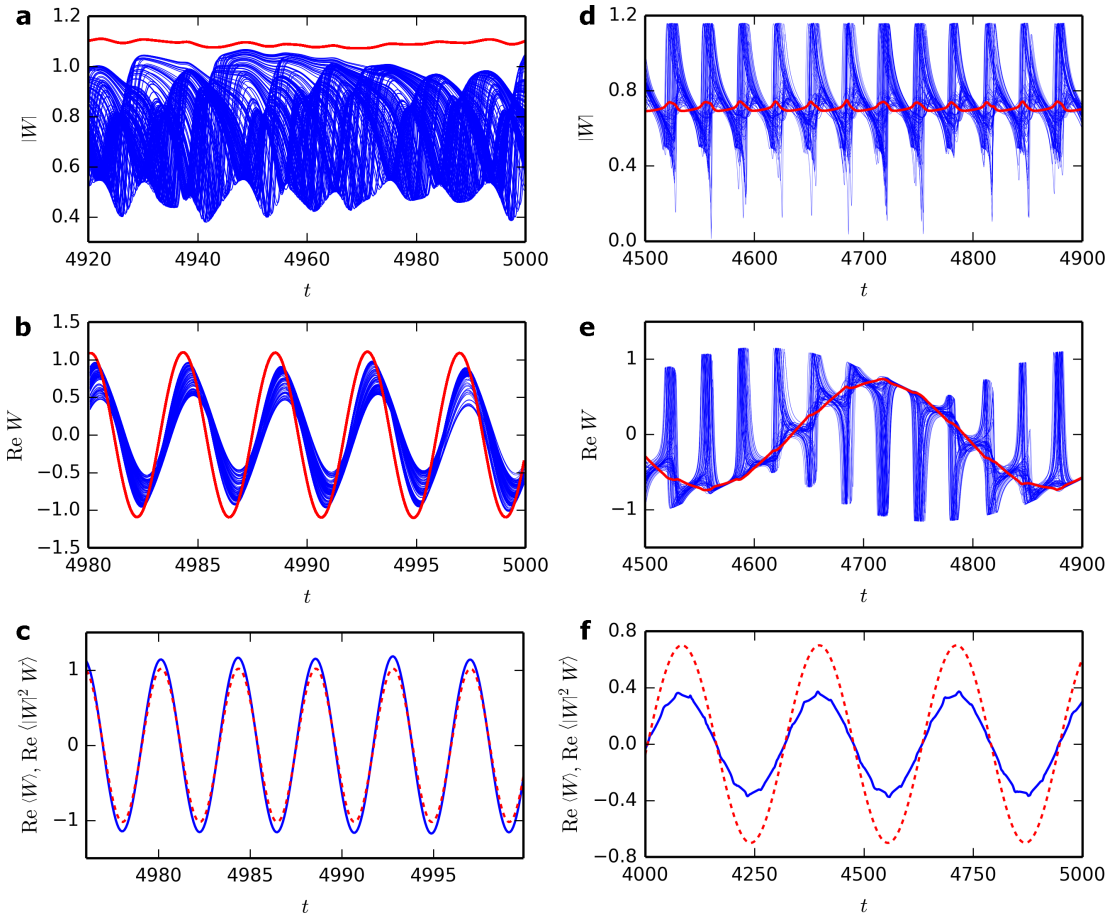

Figure 4.12: Type I and II chimera states, moduli (a,d) and real parts (b,e) versus time, respectively. The population splits into two groups, one being synchronized (red) and one being desynchronized (blue). (c,f) Linear, $\langle W \rangle$, (dashed lines) and nonlinear, $\left\langle |W|^2 W \right\rangle$, (solid lines) averages versus time for type I chimeras (c) and type II chimeras (f).

from the modulated amplitude clusters (Fig. 4.11f). The frequency of the spiking is given by the frequency of the modulational oscillations that are a result of a secondary Hopf bifurcation [129], see Section 4.2. This spiking dynamics is also visualized in the complex plane in Fig. 4.13. We observe a slow clock-wise oscillation of the synchronized group, while incoherent oscillators repeatedly perform a counter clock-wise rotation, which is the spiking dynamics. Between the excursions, both groups are very close to each other. Thus, this type of chimera state is only possible if the synchronized solution is unstable. Furthermore, this dynamics is similar to the breathing chimera state [23], where the incoherence of the desynchronized group is oscillating.

In essence, the dynamics show that the separations into incoherent and coherent groups occur via the corresponding clustering mechanism, for both types of chimeras.

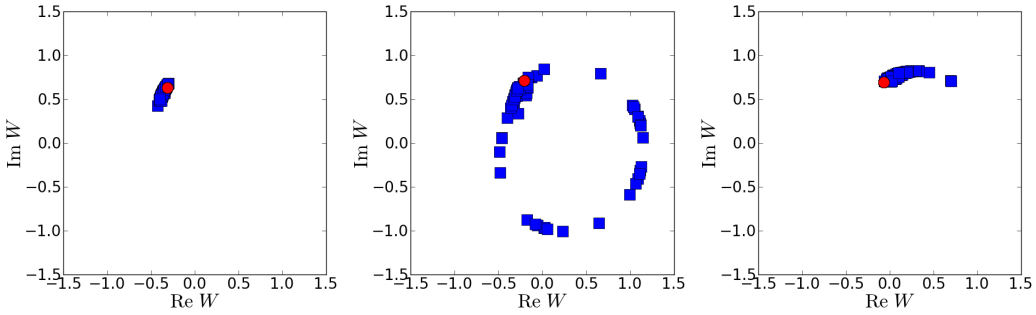

Figure 4.13: Consecutive snapshots in the complex plane for a type II chimera state. Red marks the synchronized group and blue the incoherent one.

Type I chimeras can also be found with a linear global coupling. Daido & Nakanishi [98] and also Nakagawa & Kuramoto [20] describe a state that seems to be such a chimera state, but they do not identify them as such. Only later they have been identified as chimera states [99]. We present the chimera states found under linear global coupling in Section 4.3.3. In fact, the nonlinear global coupling we consider behaves effectively like a linear global coupling in case of type I dynamics. This is visualized in Fig. 4.12c, where we plot the linear part of the coupling $\langle W \rangle$ as a red dashed line and the nonlinear part $\left\langle |W|^2 W \right\rangle$ as a blue solid line. We see that the nonlinear term is also sinusoidal, i.e., $\left\langle |W|^2 W \right\rangle \propto \langle W \rangle$, yielding an effective overall linear behaviour of the coupling. Since this implies $\left\langle |W_k|^2 W_k \right\rangle = \left\langle r_k^3 e^{i\phi_k} \right\rangle \propto \left\langle r_k e^{i\phi_k} \right\rangle$, averaging leads to vanishing nonlinear effects in the global coupling for type I chimeras. In contrast, in case of type II chimeras the dynamics of $\left\langle |W|^2 W \right\rangle$ is highly nonlinear, as shown in Fig. 4.12f. We conclude that type II dynamics might not be observable with a solely linear global coupling.

Furthermore, we looked at time series of individual oscillators in the incoherent groups. Examples are depicted in Figs. 4.14a and c for type I and II chimeras, respectively. As a simple test for chaoticity, next-maximum maps for the timeseries are shown in Figs. 4.14b and d, respectively. Both next-maximum maps are highly nontrivial and structurally very different. We see this as a clear indication that the dynamics in the incoherent parts of the two types of chimeras take place on different types of chaotic attractors. In the case of type II chimeras, the incoherent dynamics inherits properties from the motion on the torus existing at close-by parameter values, while no torus exists in the neighborhood of type I chimeras.

As already mentioned, type I chimeras are unstable and we observe heteroclinic connections. To visualize this we define a measure characterizing the different dynamical states. The natural choice of the Kuramoto order parameter is inappropriate here, because of the strong amplitude fluctuations and since $\langle W \rangle = \eta \exp(-i\nu t)$ at all times. Therefore we use the variance $\sigma = \left\langle W^2 \right\rangle - \langle W \rangle^2$. An exemplary timeseries of $|\sigma|$ for parameters of type I chimeras is shown in Fig. 4.15a.

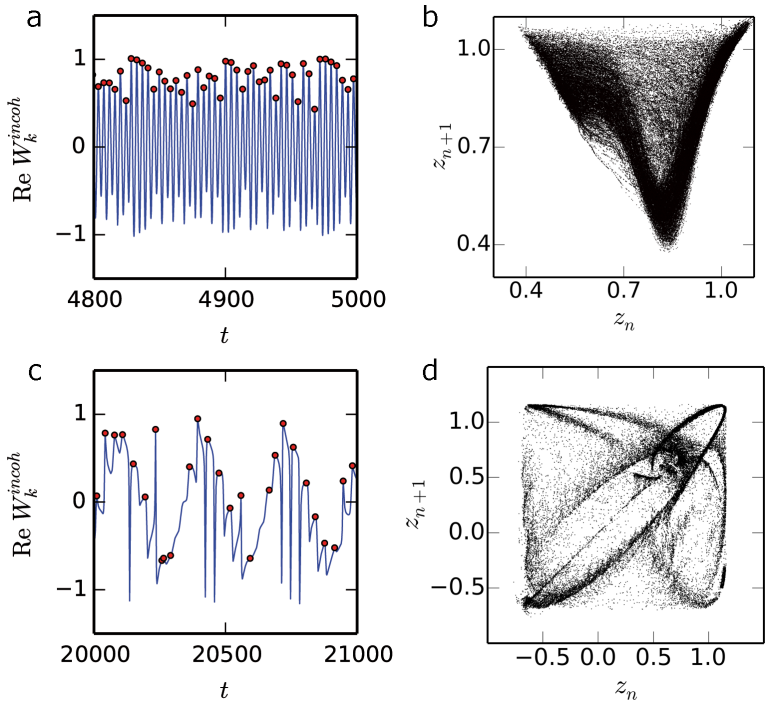

Figure 4.14: Chaos in the chimera states. (a,c) Samples of timeseries of incoherent oscillators for type I and II chimeras, respectively. Identified peaks are marked with circles. (b,d) Next-maximum maps for the peaks in (a,c).

Three qualitatively different regimes can be identified and after an initial transient, the system randomly settles first to one of them; in the trajectory shown it is a 1-3 cluster state. The dynamics in this state are depicted in Fig. 4.15b and the phase distribution at one timestep is shown in a histogram in Fig. 4.15c. This state consists of one large cluster and three small clusters of approximately the same size. The measure $|\sigma|$ exhibits strong variations around a value of approximately 0.1. Then around t = 15000 the 1-3 cluster state breaks down and the system moves to a new state that exhibits fluctuations of $|\sigma|$ around 0.05: the type I chimera state. After approximately $\Delta t = 10000$ we observe another transition to a state with nearly constant $|\sigma|$. This is the amplitude cluster state as depicted in Fig. 4.11a. Figure 4.15a suggests that transitions between these three states follow in a non-cyclic and non-periodic sequence. Thus, though being reminiscent of a heteroclinic orbit, the dynamics possesses a further peculiar, unpredictable feature.

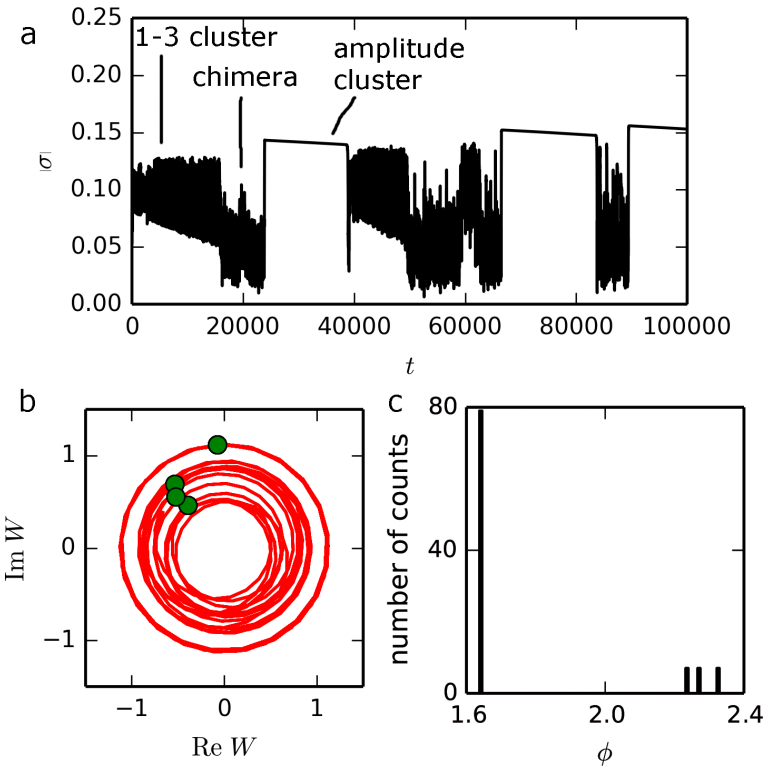

Figure 4.15: Heteroclinic connections between type I chimeras, 1-3 cluster states and amplitude clusters for $N = 100$ oscillators. (a) Trajectory of $|\sigma|$ in time showing the transitions between the different states. (b) An example for the dynamics of the 1-3 cluster state in the complex plane: lines depict time evolution and dots represent the configuration of the oscillators at one timestep. (c) Histogram of phases in the 1-3 clusters state showing that it consists of 1 large cluster and 3 small clusters of approximately the same size.

4.3.3 Type I chimeras under linear global coupling

We demonstrated in Fig. 4.12 that in case of type I chimeras the nonlinear term in the global coupling is proportional to the linear term and thus, the nonlinear global coupling is effectively linear. Indeed, type I chimeras can also be found under solely linear global coupling, as discussed in Ref. [99]. The authors considered the model:

$$\frac{\mathrm{d}W_k}{\mathrm{d}t} = W_k - (1 + ic_2)\,|W_k|^2\,W_k + K(1 + ic_3)\,(\langle W\rangle - W_k)\ , \quad k = 1, 2, \ldots, N\,. \tag{4.11}$$

Here, $K(1 + ic_3)$ is the complex prefactor of the coupling function with parameters K and c_3. We reproduced their chimera states and depict the results in Fig. 4.16. Comparing with the type I chimeras found in our model (Figs. 4.12a-c), we observe many similarities. Again, the synchronized group has a larger modulus than the desynchronized one and the overall dynamics in the modulus look similar, see Fig. 4.16a. In the real part in (b), the synchronized group performs a nearly harmonic oscillation, while

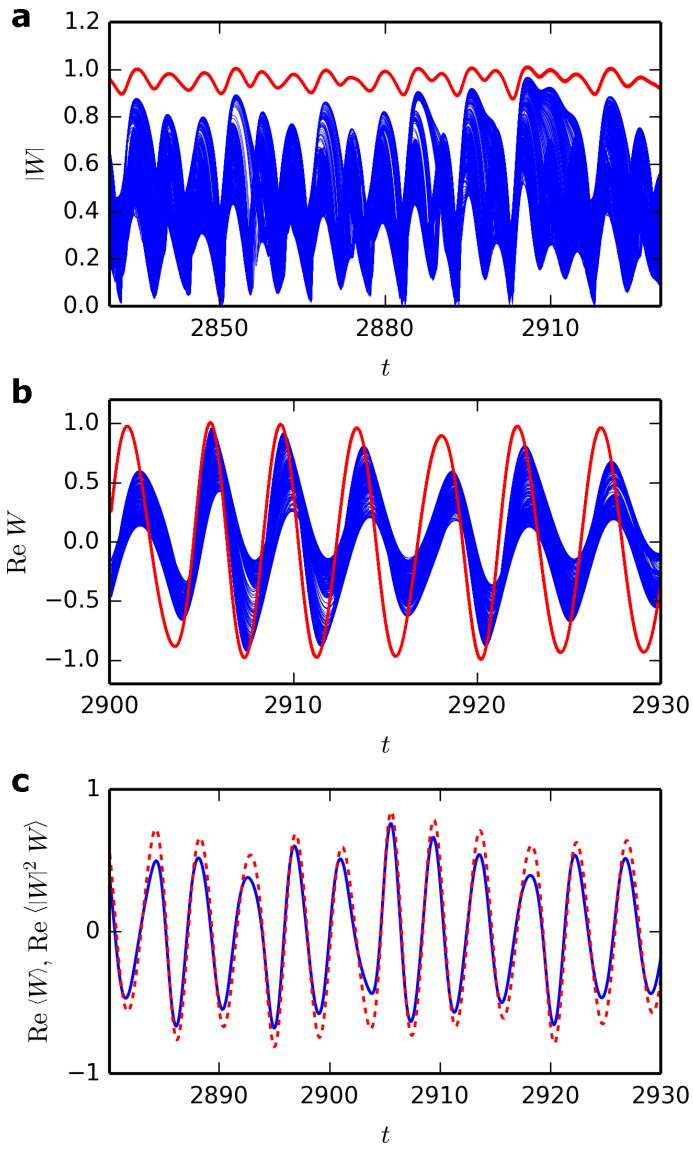

Figure 4.16: Type I chimera state in an ensemble of Stuart-Landau oscillators with linear global coupling, see Eq. (4.11). (a) Modulus $|W|$ versus time; red: synchronized group, blue: desynchronized group. (b) Real part of W versus time; red: synchronized group, blue: desynchronized group. (c) Linear average (dashed), $\langle W \rangle$, and nonlinear average (solid line), $\left\langle |W|^2 W \right\rangle$, versus time. Parameters read $c_2 = 2.0$, $K = 0.7$ and $c_3 = -1.25$.

the incoherent oscillators form a band and exhibit as a main frequency the frequency of the synchronized group. Finally, the linear and nonlinear averages in Fig. 4.16c oscillate approximately harmonically. In fact, the authors in Ref. [99] approximate the mean-field with a harmonic oscillation in order to analyze the emergence of these

chimera states. Thus, the type I chimeras under nonlinear global coupling constitute the idealized case of the chimeras presented in Fig. 4.16, in the sense that the mean-field oscillates exactly harmonically, leading to equivalent overall dynamics. Due to the preserved harmonic mean-field oscillation, the dynamics of the two groups in our model are itself more orderly. One difference is that the chimeras found under linear global coupling seem to be stable, while, so far, we could not find stable type I chimeras in the Stuart-Landau ensemble with nonlinear global coupling.

4.3.4 Phase diagrams

In order to give an impression of the existence regions of the two types of chimera states found in Eqs. (4.1), we present phase diagrams in the η vs. ν parameter plane for type I and II dynamics in Figs. 4.17 and 4.18, respectively. Note that they are only qualitative and approximative: as we do not have quantitative measures differentiating the various dynamical states, we identified them by visual inspection of the simulation results. Furthermore, as in the case of type I dynamics heteroclinic transitions occur, the phase diagram may alter for longer simulation durations. Further details are given in the figure captions. The phase diagrams demonstrate that the chimera states are indeed found in a finite parameter region.

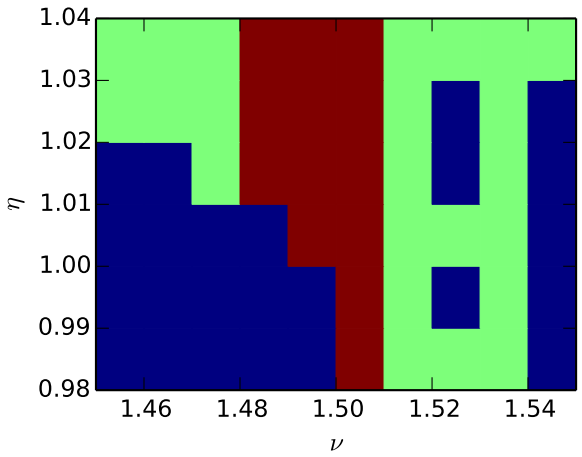

Figure 4.17: Approximate phase diagram for type I dynamics in the vicinity of the type I chimera state (Fig. 4.11b) in the η vs. ν parameter plane. We simulated $N = 100$ oscillators for a duration of $T = 1 \cdot 10^5$. By visually inspecting the simulation results, we grouped into three classes on a qualitative basis: amplitude cluster (blue), multistable without chimera (green) and multistable with chimera (red).

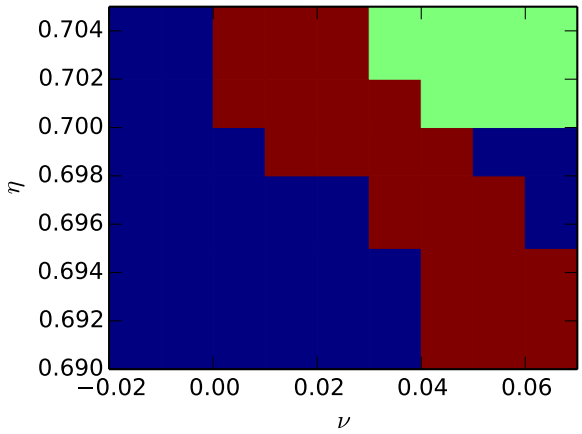

Figure 4.18: Approximate phase diagram for type II dynamics in the vicinity of the type II chimera state (Fig. 4.11e) in the η vs. ν parameter plane. We simulated $N = 1000$ oscillators and recorded data between $t = 5000$ and $t = 7000$, which is sufficient as no heteroclinic transitions are expected to occur. By visually inspecting the simulation results, we grouped into three classes on a qualitative basis: irregular (blue), modulated amplitude cluster (green) and chimera (red).

4.3.5 Conclusions

In summary, we found numerically two types of chimera states in the vicinity of two types of clusters. The chimera states inherit properties from the respective cluster states. We conclude that the clustering mechanism is a first symmetry-breaking step sufficient for chimera states to occur in oscillatory systems with uniform global coupling [130]. It differentiates the system into two groups thereby rendering it bistable. Effectively, oscillators in the two states respond differently to the coupling due to nonlinear amplitude effects. Note that as a consequence, this mechanism will not give rise to chimeras in ensembles of phase oscillators, where other mechanisms may render their formation possible [119]. Additionally, an effective difference between intra- and inter-group coupling arises as discussed in Section 3.4. Furthermore, we demonstrated that the chimera states can mediate between cluster states and completely incoherent behavior as well as between cluster states and synchrony. This leads us to the conclusion that chimera states might appear spontaneously in many globally coupled systems, as a clustering mechanism and the possibility of amplitude variations are sufficient features a system has to exhibit.

In the system with the two groups with different intra- and inter-group coupling, the separation of an ensemble into two subpopulations is done artificially [23, 31, 33]. However, it resembles the situation that arises dynamically via the clustering mechanism in our system. In the system composed of metronomes [33], the authors observe the chimeras between synchrony and the anti-phase synchronization, which corresponds to a two-cluster state. Furthermore, they found a region of bistability,

where the anti-phase synchronization and the chimera state is stable. We observe such a bistability in the case of type I chimeras, where additionally heteroclinic transitions occur.

Yeldesbay *et al.* considered two different mechanisms leading to chimera states under global coupling [119]. In one system, the bistability also emerges dynamically as a balance situation, while a second system is composed of individual bistable elements. In this latter system, the coupling is designed such that it acts repulsively in the one state and attractively in the other state. We stressed the point that nonlinear amplitude effects are important for chimera states to exist in globally coupled systems as they lead to different responses on the global force in the different states. This conclusion is corroborated by a study of globally coupled van der Pol oscillators with a nonlinear position-dependent frequency [131]. The authors show that this nonlinear effect on the frequency renders chimera states under global coupling possible.

In contrast to chimera states found in systems with nonlocal coupling [132], we could not observe a limited lifetime of type II chimeras. In case of type I chimeras, the behavior is defined by the heteroclinic network and thus, we observe a limited residence time in the type I chimera state. However, as the type II chimeras demonstrate, the separation into distinct groups, one synchronized, one desynchronized, might be more robust than the situation found under nonlocal coupling, where the synchronized and the desynchronized regions are connected by a smooth boundary. Especially the frequency curve in the incoherent part [16] shows that there is a more or less smooth transition from synchrony to incoherence. If the synchronized solution is additionally stable, it is reasonable that the chimera states are only transient in nonlocally coupled systems, at least for small numbers of oscillators.

At this point, we should remember the cluster and chimera states in the extended system, i.e., in the MCGLE. The investigation of Stuart-Landau oscillators was devoted to the better understanding of the spatio-temporal dynamics in the MCGLE. In order to transfer the conclusions of this chapter to the extended model, we have to proof that we really describe the dynamics in the extended system with this discrete model. Therefore, we compare the dynamics of oscillators in the Stuart-Landau ensemble with the dynamics of individual oscillators in the extended system, i.e., points in space, in the next chapter.

Chapter 5

Comparison of symmetry-breaking bifurcations and dynamics in the MCGLE and the Stuart-Landau ensemble

Verlockend ist der äußre Schein. Der Weise dringet tiefer ein.

(Wilhelm Busch)

So far, we simply assumed that dropping the diffusive coupling in the MCGLE, one does not loose a dynamically relevant term. Now, we demonstrate that this assumption is reasonable by comparing the dynamics of oscillators in the Stuart-Landau ensemble with the dynamics of individual oscillators, or points in space, in the extended model, the MCGLE. Therefore, we choose a few points in space in each phase of the spatio-temporal patterns. For the cluster dynamics the resulting time series are depicted in Fig. 5.1. The evolution in the complex plane in case of modulated amplitude clusters in the MCGLE (a) is indistinguishable from the corresponding dynamics of oscillators in the Stuart-Landau ensemble (b). The same holds for amplitude clusters in the MCGLE (c) and in the ensemble (d). With no doubt the results of the bifurcation analysis in Section 4.2 apply directly to the two-phase clusters in the MCGLE. A similar conclusion could be made for cluster patterns during the CO oxidation on Pt(110): Falcke & Engel demonstrate that clusters arise with the global coupling alone, no local coupling is needed [102]. In their experiment, the local coupling is due to surface diffusion of mobile adsorbates and the global coupling is due to pressure changes in the gas phase.

In Fig. 5.2 the temporal dynamics in the two types of chimera states are compared. Individual oscillators in the MCGLE in case of type I chimeras (a) exhibit the same qualitative features as oscillators in the discrete ensemble (b): the synchronized group has a larger modulus, while the incoherent oscillators show irregular motion at lower values of the modulus. Note that the c_2, ν and η values differ a bit between the extended

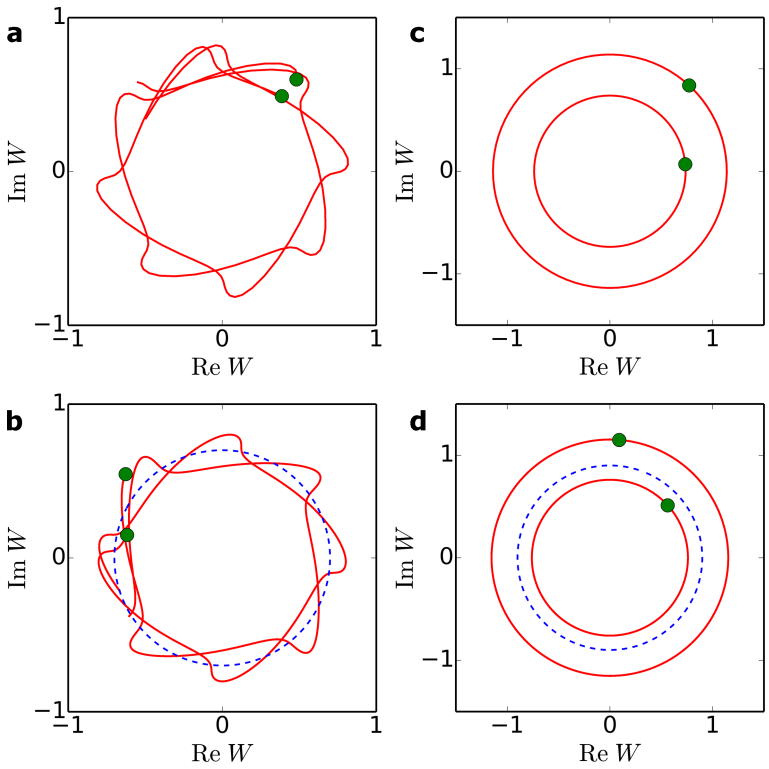

Figure 5.1: Cluster dynamics of individual oscillators in the MCGLE and in the Stuart-Landau ensemble. (a) Modulated amplitude cluster in the MCGLE ($c_1 = 0.2$, $c_2 = -0.6$, $\nu = 0.1$, $\eta = 0.7$). (b) Modulated amplitude cluster in the Stuart-Landau ensemble ($c_2 = -0.6$, $\nu = 0.1$, $\eta = 0.7$). (c) Amplitude cluster in the MCGLE ($c_1 = 0.2$, $c_2 = -0.56$, $\nu = -1.5$, $\eta = 0.9$). (d) Amplitude cluster in the Stuart-Landau ensemble ($c_2 = -0.56$, $\nu = -1.5$, $\eta = 0.9$). In (b,d) the dashed line describes the mean-field.

and the discrete model. This is attributable to the change of stability by the diffusional coupling, i.e., in the extended system the chimera state spontaneously emerges at other parameter values as the diffusional coupling shifts the stability of the solutions. This might also be the reason, why the type I chimeras seem to be stable in the MCGLE, while we could only find unstable type I chimeras in the Stuart-Landau ensemble. However, on a qualitative basis the discrete model describes the same type I chimeras as the MCGLE.

This holds also for type II chimeras, which are compared in Figs. 5.2c and d, for the MCGLE and the Stuart-Landau ensemble, respectively. In the MCGLE the oscillation of the synchronized group is not as harmonic as in the discrete model; the modulational oscillations are far more pronounced. The reason for this difference is that in the discrete model the desynchronized group is much smaller than the synchronized group, while in the extended system we observe approximately phase balance, i.e., both groups are of the same size. In both cases the mean-field has to oscillate harmonically. Hence,

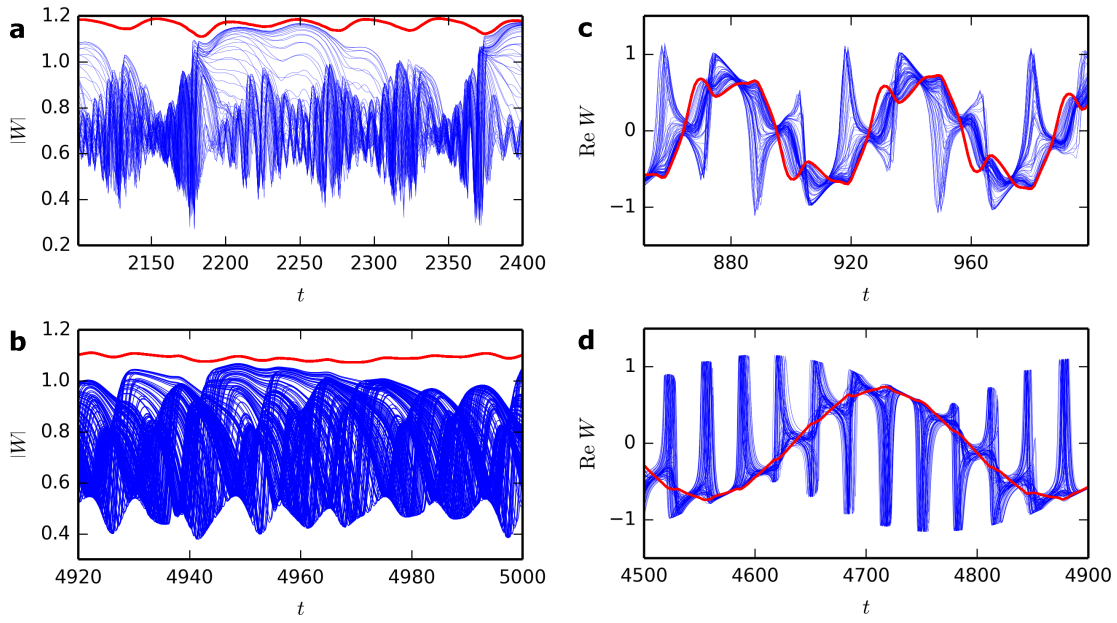

Figure 5.2: Dynamics in the two types of chimera states of individual oscillators in the MCGLE and in the Stuart-Landau ensemble. Red denotes the synchronized group and blue the desynchronized one. (a) Type I chimera in the MCGLE ($c_1 = 0.2$, $c_2 = 0.61$, $\nu = 1.5$, $\eta = 1.0$). (b) Type I chimera in the Stuart-Landau ensemble ($c_2 = 0.58$, $\nu = 1.49$, $\eta = 1.02$). (c) Type II chimera in the MCGLE ($c_1 = 0.2$, $c_2 = -0.58$, $\nu = 0.1$, $\eta = 0.66$). (d) Type II chimera in the Stuart-Landau ensemble ($c_2 = -0.6$, $\nu = 0.02$, $\eta = 0.7$).

the spiking of the incoherent oscillators has to be compensated by the synchronized group, which is more pronounced if the groups are of the same size. Furthermore, due to the diffusional interaction of nearby oscillators, the spiking is more smooth in the MCGLE. Again, the parameters are a bit different for the same reason as in case of type I chimeras.

Besides minor differences in the details of the dynamics, we can conclude that also the dynamics in the two types of chimera states in the MCGLE are sufficiently captured by the discrete Stuart-Landau ensemble. Thus, the qualitative conclusions from Section 4.3 can also be transferred to the spatio-temporal patterns.

5.1 Phase balance in the MCGLE

In the MCGLE, type II dynamics are found to display so-called phase balance, i.e., both dynamical phases are of the same spatial extension. Dropping the diffusional coupling and thus, considering the ensemble of Stuart-Landau oscillators, phase balance is broken: Usually, the two groups N_1 and N_2 are not of the same size, i.e., $N_1 \neq N_2$. Consequently, phase balance should be a result of the diffusional coupling. In order to verify this assumption and unravel the underlying mechanism, let us consider

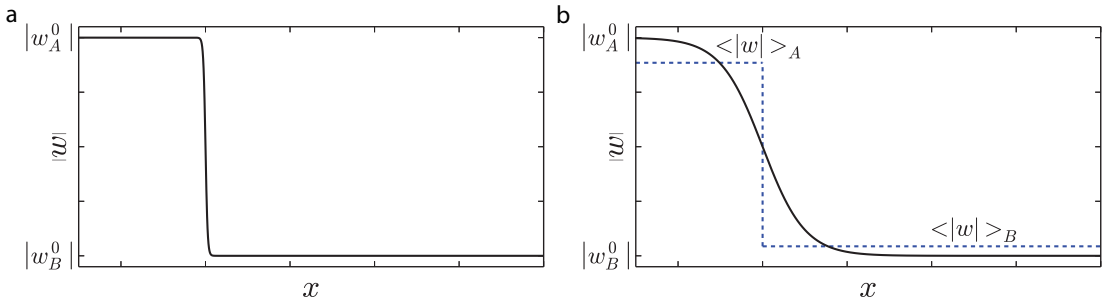

Figure 5.3: Schematical profile of a modulated amplitude cluster solution in the MCGLE in terms of $|w|$ (for definition see text), which is out of phase balance. (a) Initial profile with phase A (left) smaller than phase B (right) and a sharp phase boundary. (b) The phase boundary has become smooth due to the diffusional coupling.

modulated amplitude clusters in the MCGLE in a non-balance situation. We describe the system in the rotating frame w defined by $W = W_0(1+w)$. Figure 5.3a visualizes the non-balance situation and we call the left region phase A and the right region phase B.

From the conservation law, $\langle W \rangle = W_0$, we have

$$\langle w \rangle = \langle w_A \rangle + \langle w_B \rangle = 0 \,,$$

where the subscripts denote phases A and B, respectively. We can use the picture of discrete oscillators and write the above equation as

$$\langle w \rangle = \frac{1}{N} \left(N_A \left\langle |w| \, e^{i\phi} \right\rangle_A + N_B \left\langle |w| \, e^{i\phi} \right\rangle_B \right) = 0 \,.$$

N_A and N_B denote the number of oscillators in phase A and B, respectively, and $< \cdots >_X$ is the average over oscillators in region X, with X=A,B. Now, we assume that we can replace the phases ϕ in region A with ϕ_A and in region B with ϕ_B and these phases do not change due to diffusion. This is reasonable, since there has to be a phase shift of π between the groups, otherwise the terms cannot cancel each other. Furthermore, the amplitude dynamics are sufficient to explain the phenomenon of phase balance. Thus, we obtain

$$\frac{1}{N} \left(N_A \langle |w| \rangle_A \, e^{i\phi_A} + N_B \langle |w| \rangle_B \, e^{i(\phi_A + \pi)} \right) = 0 \,,$$

and finally

$$N_A \langle |w| \rangle_A = N_B \langle |w| \rangle_B \,. \tag{5.1}$$

The latter equation has to be fulfilled because of the conservation law present in our system. In case of the ensemble of Stuart-Landau oscillators, a cluster solution can be realized for many values of N_A and N_B, while then $\langle |w| \rangle_{A,B}$ have to adopt appropriate values in order to fulfill Eq. (5.1).

What happens if the diffusional coupling is introduced, is visualized in Figs. 5.3a and b. Let the initial configuration be as shown in Fig. 5.3a, i.e., phase A is smaller than

phase B and the phase boundary is very sharp. Initial values of $|w|$ in phases A and B are given by $\left|w^0_{A,B}\right|$, respectively. The diffusional coupling will smoothen the boundary, resulting in a boundary as shown schematically in Fig. 5.3b. We observe that the mean value $\langle|w|\rangle_A$ decreased compared to $\left|w^0_A\right|$ and $\langle|w|\rangle_B$ increased compared to $\left|w^0_B\right|$ (see dashed lines). In order to satisfy the conservation law in Eq. (5.1), the cluster sizes N_A and N_B have to adapt appropriately. Thus, N_A increases and N_B decreases and this procedure takes place until phase balance is reached. Note that in the phase-balance situation, $N_A = N_B$ and also $\langle|w|\rangle_A = \langle|w|\rangle_B$, while there is still a phase shift of π.

The above considerations verify that the diffusional coupling together with the conservation law can lead to the occurrence of phase balance in the MCGLE. However, phase balance is only observed for type II dynamics, while type I dynamics, e.g., amplitude clusters, show a non-balance configuration. We could not identify the reason behind this difference between the two types of patterns.

Chapter 6

Summary & Outlook

Das Ganze ist mehr als die Summe seiner Teile.
(Aristoteles)

Spatially resolving the thickness of the oxide-layer on an n-type silicon working electrode during its photoelectrodissolution reveals peculiar spatio-temporal dynamics [13, 14, 79, 80, 91]. Typical patterns range from cluster dynamics and turbulence to such astonishing, symmetry-breaking dynamics as chimera states [16, 17, 35]. In a chimera state, the system splits into two dynamical phases, one phase oscillating in synchrony and the other phase displaying incoherent dynamics. In this thesis, we investigated the underlying mechanisms of these dynamics.

Since the basic oscillation in the photoelectrodissolution of n-type silicon arises via a Hopf bifurcation, in the vicinity of this bifurcation, the dynamics are captured with the CGLE. Yet, this is only appropriate to describe the synchronized oscillation, as the relevant coupling terms are missing. Thus, more details of the system have to be introduced in the model. The key property is the oscillation of the spatially averaged oxide-layer thickness, which is harmonic with constant amplitude and frequency, for a huge region in parameter space, despite complex spatio-temporal dynamics. Introducing a nonlinear global coupling in the CGLE, a preserved harmonic mean-field oscillation can be achieved [13, 15]. In the experiments such a nonlinear global coupling is most likely also present: We believe that the restriction of available charge carriers by limitation of the illumination results in a nonlinear global coupling, as it influences the total current, in a nonlinear fashion.

In this thesis we demonstrated, by means of two-dimensional simulations of the CGLE with nonlinear global coupling, that the patterns forming in the oxide-layer thickness are well captured with this very general model, mimicking only essential features of the experiment, but omitting all detailed mechanisms. Not only the cluster patterns exhibiting two characteristic frequencies, but also the chimera state can be reproduced with the modified complex Ginzburg-Landau equation. In both, the

experiments and the simulation, we could encounter the same route leading from the cluster state via subclustering to the chimera state [79]. In the subcluster state, one of the two phases is synchronous, while the other exhibits two-phase clusters as a substructure. We argued that a cluster state breaks, first of all, the symmetry. The phase difference results in a intra-group coupling that is different to the inter-group coupling. Chimera states could be observed theoretically [23] and experimentally [31] in a system, where this situation of two groups with different intra- and inter-group coupling is introduced artificially. In the experiments of Ref. [31] the same route from clusters to chimeras via subclustering is found. Remarkably, in our simulations as well as in our experiments nothing is imposed to introduce this symmetry breaking. The chimera states arise spontaneously due to the intrinsic dynamics. All parameters are kept uniform and care was taken to make the coupling in the experiment symmetric. Also the initial conditions are not relevant, as one can start in a uniform state with superimposed noise.

In the simulations we found a further type of cluster pattern and also a corresponding chimera state. The cluster pattern in this case is the well-known amplitude cluster [98], which consists of two groups oscillating at different radii with a small and fixed phase difference. We termed these states type I dynamics and the dynamics reproducing the experiments type II dynamics. This nomenclature goes back to Ref. [97], where the authors describe type II clusters, which exhibit an uniform oscillation plus a second oscillation with which two-phase clusters come along. This resembles the situation in the type II clusters described in this thesis. Thus, in the MCGLE we observe two types of clusters with two associated types of chimera states, where the second type of dynamics reproduces patterns found in the experiments.

It has long been thought that a nonlocal coupling, i.e., a coupling whose range is between local and global and whose strength decreases with the distance, is indispensable for the formation of chimera states. During the course of this thesis we were able to proof the contrary, as the chimera states we found arise under global coupling. In the MCGLE the diffusional coupling disguises this fact as one might argue that a global coupling plus a local coupling amounts to a nonlocal coupling. Note that the model describing two groups with different intra- and inter-group coupling [23, 31] constitutes a minimal model with nonlocal coupling, as the coupling in some sense still decreases with the distance. This situation arises in our model only effectively, the underlying coupling is still global plus diffusive. In fact, by omitting the diffusional coupling, we could proof that the chimera states survive and emerge under solely global coupling. We will come back to that point below. Meanwhile, chimera states could be observed in other globally coupled systems [99, 119].

Type II chimera states in the extended system are always found in a phase-balanced configuration. Thus, interchanging the coherent with the incoherent phase yields for symmetry reasons again a solution to the underlying equations. Consequently, we could oberserve spontaneously emerging alternating chimera states, in which synchronized and desynchronized regions interchange from time to time. This observation might be of importance in understanding unihemispherical sleep, where such alterna-

tions could also be observed [35, 38, 39, 42].

Various dynamics found in the MCGLE are not reliant on the diffusional coupling. The nonlinear global coupling yields the essential dynamics, while the diffusional coupling only leads to the spatial arrangement of the patterns. We verified this assumption in Chapter 5. We omitted the diffusional coupling and considered an ensemble of Stuart-Landau oscillators with nonlinear global coupling in Chapter 4, in order to gain more insight into the mechanisms behind the spatio-temporal dynamics we found.

Starting with the cluster patterns in Section 4.2, we reduced the set of N equations to two effective equations, describing two groups of sizes N_1 and N_2. Under the assumption of equal group sizes, i.e., $N_1 = N_2$, a bifurcation analysis became possible. Therefore, we described the dynamics in terms of a deviation w from the uniform oscillation, defined via $W = W_0(1 + w)$, where W_0 is the mean-field oscillation. The resulting equations for w_1 and w_2 constitute the forced CGLE near a 2:1 resonance, when neglecting the diffusional coupling. This gives rise to a complex bifurcation structure, which is tongue-shaped in the η (mean-field amplitude) versus ν (mean-field frequency) plane. Its origin for $\eta = 0$ is at $\nu = c_2$, i.e., at the frequency of the underlying homogeneous dynamics of the Stuart-Landau oscillator. This leads to the interpretation that the conserved mean-field oscillation can be seen as a periodic self-forcing of the system.

The bifurcation analysis revealed that the type II clusters arise in a Hopf bifurcation for w, which is then a secondary Hopf bifurcation in the full system. This Hopf bifurcation gives rise to the modulational oscillations, the reason why we call the type II clusters modulated amplitude clusters. Since $w_2 = -w_1$, the second group always realizes the π-rotated solution, explaining the phase shift of π in the full system at the frequency of the modulational oscillation. Consequently, we observe quasiperiodic behavior in the full system and the frequency of the modulational oscillation can be tuned with the parameters. In contrast, the modulated amplitude clusters in the experiments seem to arise via a period-doubling bifurcation, as the frequency of the modulational oscillation is always observed to amount to half the frequency of the uniform oscillation. Amplitude clusters arise either via a pitchfork bifurcation with the synchronized solution or in a saddle-node of infinite period bifurcation, thereby destroying the torus of the modulated amplitude clusters. Thus, the amplitude clusters constitute the locked solutions inside the tongue. Interestingly, we observe a 1:1 locking, despite the bifurcation structure of a 2:1 resonance, which is, in turn, indispensable to observe two-cluster solutions.

Finally, we demonstrated that the two types of chimera states found in the MCGLE are indeed observable without the diffusive coupling and thus, with a solely global coupling. The analysis of the neighboring states led us to the conclusion that a cluster mechanism is the first symmetry-breaking step on the way to chimera states in globally coupled systems. This is in line with the conclusion that the two-phase cluster states yield effectively different intra- and inter-group couplings. Additionally, nonlinear amplitude effects are important, especially for type I chimeras, as then the response on a global force can be different in different groups. Furthermore, the resulting chimera

dynamics inherit properties from the clusters, in which they originate. We found also that in case of type I dynamics the nonlinear global coupling effectively behaves like a linear global coupling and we could establish a connection to chimera states found in an ensemble of Stuart-Landau oscillators with solely linear global coupling [99]. Consequently, we demonstrated that these chimera states with linear global coupling in the discrete model give rise to chimera states in a CGLE with linear global coupling, which are equivalent to the type I chimeras found in the MCGLE. In contrast, in case of type II dynamics the nonlinearity of the coupling seems to be indispensable.

> *Chaos: When the present determines the future, but the approximate present does not approximately determine the future.*
>
> (Edward Lorenz)

Astonishing spatio-temporal dynamics can be observed in oscillatory media under nonlinear global coupling. In case of the photoelectrodissolution of n-type silicon we are able to model them with a general ansatz and identified principles and bifurcations underlying the pattern formation. Still unresolved are the physical model of the basic oscillation and the exact physical mechanism of the nonlinear global coupling. Once this is done, using a center manifold reduction technique, the corresponding normal form can be derived. This will show, for which parameter regions the ansatz chosen in this thesis is valid and yield a connection between the parameters in the theory and in the experimental system.

Further questions are: Can one define a measure that is minimized or maximized under the process of pattern formation? Why does the system exhibit the coexistence of different dynamics? These questions have to be answered in order to learn more about the principles governing pattern formation. This holds especially for the coexistence of synchrony and incoherence, the chimera state, constituting the strongest symmetry-breaking state. Measures have to be defined characterizing the different classes of chimera states. Furthermore, the connections to real world processes like unihemispherical sleep have to be extended and set on a profound scientific basis. Therefore, we need to look at neuronal dynamics in more detail and understand how the brain is working. We need to know in detail, how the basic oscillators, the neurons, can be described and how they are coupled to each other. This may lead to a deeper understanding of brain functions and disfunctions, rendering effective therapies for, e.g., Parkinson's disease or epileptic seizures possible.

Once the fundamental principles behind the spatio-temporal pattern formation and the symmetry-breaking states are identified, they can be transferred to other systems composed of many coupled elements. Examples can be found in social sciences, describing the dynamics of groups of human beings with their complex interactions. This can be the process of opinion formation or also mass panic dynamics. Another

example gaining in importance is the stability of the electrical power grid, when more and more renewable energies are used. Strong fluctuations in the power input and a very small inertia of the whole grid renders it more unstable with respect to small perturbations. Perhaps even the phenomenon of a chimera state in the electrical power grid is imaginable, yielding normal power supply in part of a country and local breakdown in other parts.

Not only in research, but also in the everyday world of politics and economics, we would all be better off if more people realised that simple nonlinear systems do not necessarily possess simple dynamical properties.

(Robert M. May)

Publications

L. Schmidt & K. Krischer. Chimeras in globally coupled oscillatory systems: From ensembles of oscillators to spatially continuous media. *Chaos* **25**(6), 064401 (2015).

S. W. Haugland, L. Schmidt & K. Krischer. Self-organized alternating chimera states in oscillatory media. *Scientific Reports* **5**, 9883 (2015).

L. Schmidt & K. Krischer. Clustering as a prerequisite for chimera states in globally coupled systems. *Phys. Rev. Lett.* **114**, 034101 (2015).

L. Schmidt, K. Schönleber, V. García-Morales & K. Krischer. Unusual synchronization phenomena during electrodissolution of silicon: the role of nonlinear global coupling. In A. S. Mikhailov & G. Ertl, editors, *Engineering of Chemical Complexity II, World Scientific Lecture Notes in Complex Systems*, volume 12. World Scientific Publishing Co. Pte. Ltd., Singapore (2015).

L. Schmidt & K. Krischer. Two-cluster solutions in an ensemble of generic limit-cycle oscillators with periodic self-forcing via the mean-field. *Phys. Rev. E* **90**, 042911 (2014).

L. Schmidt, K. Schönleber, K. Krischer & V. García-Morales. Coexistence of synchrony and incoherence in oscillatory media under nonlinear global coupling. *Chaos* **24**(1), 013102 (2014).

Bibliography

[1] R. M. May. Simple mathematical models with very complicated dynamics. *Nature* **261**, 459 (1976).

[2] S. H. Strogatz. *Nonlinear Dynamics and Chaos*. Perseus Books Publishing, LLC (1994).

[3] A. Gierer & H. Meinhardt. A theory of biological pattern formation. *Kybernetik* **12**, 30 (1972).

[4] A. M. Turing. The chemical basis of morphogenesis. *Phil. Trans. Roy. Soc. B* **237**, 37 (1952).

[5] J. Lechleiter, S. Girard, E. Peralta & D. Clapham. Spiral calcium wave propagation and annihilation in Xenopus laevis oocytes. *Science* **252**(5002), 123–126 (1991).

[6] A. T. Winfree. Electrical turbulence in three-dimensional heart muscle. *Science* **266**(5187), 1003–1006 (1994).

[7] E. M. Cherry & F. H. Fenton. Visualization of spiral and scroll waves in simulated and experimental cardiac tissue. *New Journal of Physics* **10**(12), 125016 (2008).

[8] A. Garfinkel, M. L. Spano, W. L. Ditto & J. N. Weiss. Controlling cardiac chaos. *Science* **257**, 1230 (1992).

[9] B. Ermentrout. Neural networks as spatio-temporal pattern-forming systems. *Rep. Prog. Phys.* **61**(4), 353 (1998).

[10] G. Ertl. Oscillatory kinetics and spatio-temporal self-organization in reactions at solid surfaces. *Science* **254**(5039), 1750–1755 (1991).

[11] V. K. Vanag, L. Yang, M. Dolnik, A. M. Zhabotinsky & I. R. Epstein. Oscillatory cluster patterns in a homogeneous chemical system with global feedback. *Nature* **406**, 389–391 (2000).

[12] I. R. Epstein & K. Showalter. Nonlinear chemical dynamics: Oscillations, patterns, and chaos. *The Journal of Physical Chemistry* **100**(31), 13132–13147 (1996).

[13] I. Miethe, V. García-Morales & K. Krischer. Irregular subharmonic cluster patterns in an autonomous photoelectrochemical oscillator. *Phys. Rev. Lett.* **102**, 194101 (2009).

[14] I. Miethe. Spatio-temporal pattern formation during the anodic electrodissolution of silicon in ammonium fluoride solution. *PhD Thesis, TU München* (2010).

[15] V. García-Morales, A. Orlov & K. Krischer. Subharmonic phase clusters in the complex Ginzburg-Landau equation with nonlinear global coupling. *Phys. Rev. E* **82**, 065202 (2010).

[16] Y. Kuramoto & D. Battogtokh. Coexistence of coherence and incoherence in nonlocally coupled phase oscillators. *Nonlin. Phenom. in Complex Syst.* **5**, 380–385 (2002).

[17] D. M. Abrams & S. H. Strogatz. Chimera states for coupled oscillators. *Phys. Rev. Lett.* **93**, 174102 (2004).

[18] D. K. Umberger, C. Grebogi, E. Ott & B. Afeyan. Spatiotemporal dynamics in a dispersively coupled chain of nonlinear oscillators. *Phys. Rev. A* **39**, 4835–4842 (1989).

[19] K. Kaneko. Clustering, coding, switching, hierarchical ordering, and control in a network of chaotic elements. *Physica D: Nonlinear Phenomena* **41**(2), 137 – 172 (1990).

[20] N. Nakagawa & Y. Kuramoto. Collective chaos in a population of globally coupled oscillators. *Prog. Theor. Phys.* **89**(2), 313–323 (1993).

[21] S.-i. Shima & Y. Kuramoto. Rotating spiral waves with phase-randomized core in nonlocally coupled oscillators. *Phys. Rev. E* **69**, 036213 (2004).

[22] G. C. Sethia, A. Sen & F. M. Atay. Clustered chimera states in delay-coupled oscillator systems. *Phys. Rev. Lett.* **100**, 144102 (2008).

[23] D. M. Abrams, R. Mirollo, S. H. Strogatz & D. A. Wiley. Solvable model for chimera states of coupled oscillators. *Phys. Rev. Lett.* **101**, 084103 (2008).

[24] E. A. Martens, C. R. Laing & S. H. Strogatz. Solvable model of spiral wave chimeras. *Phys. Rev. Lett.* **104**, 044101 (2010).

[25] G. Bordyugov, A. Pikovsky & M. Rosenblum. Self-emerging and turbulent chimeras in oscillator chains. *Phys. Rev. E* **82**, 035205 (2010).

[26] C. R. Laing. Chimeras in networks of planar oscillators. *Phys. Rev. E* **81**, 066221 (2010).

[27] I. Omelchenko, Y. Maistrenko, P. Hövel & E. Schöll. Loss of coherence in dynamical networks: Spatial chaos and chimera states. *Phys. Rev. Lett.* **106**, 234102 (2011).

[28] I. Omelchenko, B. Riemenschneider, P. Hövel, Y. Maistrenko & E. Schöll. Transition from spatial coherence to incoherence in coupled chaotic systems. *Phys. Rev. E* **85**, 026212 (2012).

[29] S. Nkomo, M. R. Tinsley & K. Showalter. Chimera states in populations of nonlocally coupled chemical oscillators. *Phys. Rev. Lett.* **110**, 244102 (2013).

[30] I. Omelchenko, O. E. Omel'chenko, P. Hövel & E. Schöll. When nonlocal coupling between oscillators becomes stronger: Patched synchrony or multichimera states. *Phys. Rev. Lett.* **110**, 224101 (2013).

[31] M. R. Tinsley, N. Simbarashe & K. Showalter. Chimera and phase-cluster states in populations of coupled chemical oscillators. *Nature Phys.* **8**, 662–665 (2012).

[32] A. M. Hagerstrom *et al.* Experimental observation of chimeras in coupled-map lattices. *Nature Phys.* **8**, 658–661 (2012).

[33] E. A. Martens, S. Thutupalli, A. Fourrière & O. Hallatschek. Chimera states in mechanical oscillator networks. *Proc. Natl. Acad. Sci.* **110**(26), 10563–10567 (2013).

[34] M. Wickramasinghe & I. Z. Kiss. Spatially organized dynamical states in chemical oscillator networks: Synchronization, dynamical differentiation, and chimera patterns. *PLoS ONE* **8**(11), e80586 (2013).

[35] M. J. Panaggio & D. M. Abrams. Chimera states: Coexistence of coherence and incoherence in networks of coupled oscillators. *arXiv* page 1403.6204v2 (2014).

[36] C. R. Laing. The dynamics of chimera states in heterogeneous Kuramoto networks. *Physica D: Nonlinear Phenomena* **238**(16), 1569 – 1588 (2009).

[37] O. E. Omel'chenko. Coherence–incoherence patterns in a ring of non-locally coupled phase oscillators. *Nonlinearity* **26**(9), 2469 (2013).

[38] N. C. Rattenborg, C. J. Amlaner & S. L. Lima. Behavioral, neurophysiological and evolutionary perspectives on unihemispheric sleep. *Neurosc. and Biobehav. Rev.* **24**, 817–842 (2000).

[39] C. G. Mathews, J. A. Lesku, S. L. Lima & C. J. Amlaner. Asynchronous eye closure as an anti-predator behavior in the western fence lizard (sceloporus occidentalis). *Ethology* **112**, 286–292 (2006).

[40] T. P. Vogels, K. Rajan & L. F. Abbott. Neural network dynamics. *Annu. Rev. Neurosci.* **28**, 357–376 (2005).

[41] D. Barkley & L. S. Tuckerman. Computational study of turbulent laminar patterns in Couette flow. *Phys. Rev. Lett.* **94**, 014502 (2005).

[42] O. I. Lyamin, P. R. Manger, S. H. Ridgway, L. M. Mukhametov & J. M. Siegel. Cetacean sleep: An unusual form of mammalian sleep. *Neurosci. Biobehav. Rev.* **32**(8), 1451 – 1484 (2008).

[43] C. R. Laing. Disorder-induced dynamics in a pair of coupled heterogeneous phase oscillator networks. *Chaos: An Interdisciplinary Journal of Nonlinear Science* **22**(4), 043104 (2012).

[44] R. Ma, J. Wang & Z. Liu. Robust features of chimera states and the implementation of alternating chimera states. *EPL (Europhysics Letters)* **91**(4), 40006 (2010).

[45] J. Guckenheimer & P. Holmes. *Nonlinear Oscillations, Dynamical Systems, and Bifurcations of Vector Fields*. Springer-Verlag New York, Inc. (1983).

[46] L. D. Landau. On the problem of turbulence. *C. R. Dokl. Acad. Sci. URSS* **44**, 311 (1944).

[47] J. T. Stuart. On the non-linear mechanics of wave disturbances in stable and unstable parallel flows. Part 1: The basic behaviour in plane Poiseuille flow. *J. Fluid. Mech.* **9**, 353 (1960).

[48] Y. Kuramoto. *Chemical Oscillations, Waves, and Turbulence*. Dover Publications, Inc., Mineola, New York (2003).

[49] V. García-Morales & K. Krischer. The complex Ginzburg–Landau equation: an introduction. *Contemporary Physics* **53**(2), 79–95 (2012).

[50] A. C. Newell & J. A. Whitehead. Finite bandwidth, finite amplitude convection. *J. Fluid Mech.* **38**, 279–303 (1969).

[51] K. Stewartson & J. T. Stuart. A non-linear instability theory for a wave system in plane Poiseuille flow. *J. Fluid Mech.* **48**, 529–545 (1971).

[52] R. C. DiPrima, W. Eckhaus & L. A. Segel. Non-linear wave-number interaction in near-critical two-dimensional flows. *J. Fluid Mech.* **49**, 705–744 (1971).

[53] A. Weber, L. Kramer, I. Aranson & L. Aranson. Stability limits of traveling waves and the transition to spatiotemporal chaos in the complex Ginzburg-Landau equation. *Physica D: Nonlinear Phenomena* **61**(1–4), 279 – 283 (1992).

[54] B. Shraiman *et al.* Spatiotemporal chaos in the one-dimensional complex Ginzburg-Landau equation. *Physica D: Nonlinear Phenomena* **57**(3–4), 241 – 248 (1992).

[55] I. S. Aranson, L. Aranson, L. Kramer & A. Weber. Stability limits of spirals and traveling waves in nonequilibrium media. *Phys. Rev. A* **46**, R2992–R2995 (1992).

[56] M. Bazhenov & M. Rabinovich. Synchronized disorder in a 2D complex Ginzburg-Landau equation. *Physica D* **73**, 318 (1994).

[57] H. Chaté. Spatiotemporal intermittency regimes of the one-dimensional complex Ginzburg-Landau equation. *Nonlinearity* **7**(1), 185 (1994).

[58] M. Bazhenov, M. Rabinovich & L. Rubchinsky. Time-periodic spatial chaos in the complex Ginzburg-Landau equation. *J. Stat. Phys.* **83**, 1165 (1996).

[59] R. Braun & F. Feudel. Supertransient chaos in the two-dimensional complex Ginzburg-Landau equation. *Phys. Rev. E* **53**, 6562–6565 (1996).

[60] H. Chaté & P. Manneville. Phase diagram of the two-dimensional complex Ginzburg-Landau equation. *Physica A* **224**(1–2), 348 – 368 (1996).

[61] P. Manneville & H. Chaté. Phase turbulence in the two-dimensional complex Ginzburg-Landau equation. *Physica D: Nonlinear Phenomena* **96**(1–4), 30 – 46 (1996).

[62] T. Bohr, G. Huber & E. Ott. The structure of spiral domain patterns. *EPL (Europhysics Letters)* **33**(8), 589 (1996).

[63] T. Bohr, G. Huber & E. Ott. The structure of spiral-domain patterns and shocks in the 2D complex Ginzburg-Landau equation. *Physica D: Nonlinear Phenomena* **106**(1–2), 95 – 112 (1997).

[64] M. van Hecke. Building blocks of spatiotemporal intermittency. *Phys. Rev. Lett.* **80**, 1896–1899 (1998).

[65] Y. Kuramoto & T. Tsuzuki. On the formation of dissipative structures in reaction-diffusion systems: Reductive perturbation approach. *Progress of Theoretical Physics* **54**(3), 687–699 (1975).

[66] Y. Kuramoto & T. Tsuzuki. Persistent propagation of concentration waves in dissipative media far from thermal equilibrium. *Progress of Theoretical Physics* **55**(2), 356–369 (1976).

[67] I. S. Aranson & L. Kramer. The world of the complex Ginzburg-Landau equation. *Rev. Mod. Phys.* **74**, 99–143 (2002).

[68] M. C. Cross & P. C. Hohenberg. Pattern formation outside of equilibrium. *Rev. Mod. Phys.* **65**, 851–1112 (1993).

[69] A. C. Newell, T. Passot & J. Lega. Order parameter equations for patterns. *Annu. Rev. Fluid Mech.* **25**(1), 399–453 (1993).

[70] K. Krischer. Nonlinear dynamics in electrochemical systems. In R. C. Alkire & D. M. Kolb, editors, *Advances in Electrochemical Science and Engineering*, volume 8, pages 89–208. Wiley-VCH, Weinheim (2003).

[71] V. García-Morales & K. Krischer. Nonlocal complex Ginzburg-Landau equation for electrochemical systems. *Phys. Rev. Lett.* **100**, 054101 (2008).

[72] D. Tanaka & Y. Kuramoto. Complex Ginzburg-Landau equation with nonlocal coupling. *Phys. Rev. E* **68**, 026219 (2003).

[73] F. Mertens, R. Imbihl & A. Mikhailov. Breakdown of global coupling in oscillatory chemical reactions. *The Journal of Chemical Physics* **99**(11), 8668–8671 (1993).

[74] F. Mertens, R. Imbihl & A. Mikhailov. Turbulence and standing waves in oscillatory chemical reactions with global coupling. *The Journal of Chemical Physics* **101**(11), 9903–9908 (1994).

[75] J. M. Gambaudo. Perturbation of a Hopf bifurcation by an external time-periodic forcing. *J. Diff. Eqs.* **57**, 172 (1985).

[76] A. Yochelis, C. Elphick, A. Hagberg & E. Meron. Two-phase resonant patterns in forced oscillatory systems: boundaries, mechanisms and forms. *Physica D: Nonlinear Phenomena* **199**(1–2), 201 – 222 (2004).

[77] M. Müller. Pattern formation in the two-dimensional complex Ginzburg-Landau equation with nonlinear global coupling. *Bachelor Thesis, TU München* (2011).

[78] S. M. Cox & P. C. Matthews. Exponential time differencing for stiff systems. *J. Comp. Phys.* **176**, 430–455 (2002).

[79] L. Schmidt, K. Schönleber, K. Krischer & V. García-Morales. Coexistence of synchrony and incoherence in oscillatory media under nonlinear global coupling. *Chaos: An Interdisciplinary Journal of Nonlinear Science* **24**(1), 013102 (2014).

[80] L. Schmidt, K. Schönleber, V. García-Morales & K. Krischer. Unusual synchronization phenomena during electrodissolution of silicon: the role of nonlinear global coupling. In A. S. Mikhailov & G. Ertl, editors, *Engineering of Chemical Complexity II, World Scientific Lecture Notes in Complex Systems*, volume 12. World Scientific Publishing Co. Pte. Ltd., Singapore (2015).

[81] D. R. Turner. Electropolishing silicon in hydrofluoric acid solutions. *J. Electrochem. Soc.* **105**, 402–408 (1958).

[82] R. Memming & G. Schwandt. Anodic dissolution of silicon in hydrofluoric acid solutions. *Surf. Science* **4**, 109–124 (1966).

[83] S. Cattarin, I. Frateur, M. Musiani & B. Tribollet. Electrodissolution of p-Si in acidic fluoride media: Modeling of the steady state. *J. Electrochem. Soc.* **147**, 3277–3282 (2000).

[84] H. Hasegawa, S. Arimoto, J. Nanjo, H. Yamamoto & H. Ohno. Anodic oxidation of hydrogenated amorphous silicon and properties of oxide. *J. Electrochem. Soc.* **135(2)**, 424 (1988).

[85] X. G. Zhang. *Electrochemistry of Silicon and Its Oxides*. Kluwer Academic/Plenum Publishers, New York (2001).

[86] D. J. Blackwood, A. Borazio, R. Greef, L. M. Peter & J. Stuper. Electrochemical and optical studies of silicon dissolution in ammonium fluoride solutions. *Electrochimica Acta* **37**, 889–896 (1992).

[87] J.-N. Chazalviel, C. da Fonseca & F. Ozanam. In situ infrared study of the oscillating anodic dissolution of silicon in fluoride electrolytes. *J. Electrochem. Soc.* **145**, 964–973 (1998).

[88] F. Yahyaoui *et al.* Etch rates of anodic silicon oxides in dilute fluoride solutions. *J. Electrochem. Soc.* **150**, B205–B210 (2003).

[89] J.-N. Chazalviel. Ionic processes through the interfacial oxide in the anodic dissolution of silicon. *Electrochimica Acta* **37**(5), 865 – 875 (1992).

[90] M. Aggour, M. Giersig & H. Lewerenz. Interface condition of n-Si(111) during photocurrent oscillations in NH_4F solutions. *J. Electroanal. Chem.* **383**(1–2), 67 – 74 (1995).

[91] K. Schönleber, C. Zensen, A. Heinrich & K. Krischer. Pattern formation during the oscillatory photoelectrodissolution of n-type silicon: turbulence, clusters and chimeras. *New Journal of Physics* **16**, 063024 (2014).

[92] H. H. Rotermund, G. Haas, R. U. Franz, R. M. Tromp & G. Ertl. Imaging pattern formation in surface reactions from ultrahigh vacuum up to atmospheric pressure. *Science* **270**, 608–610 (1995).

[93] J. N. Chazalviel *et al.* The p-Si/fluoride interface in the anodic region: Damped and/or sustained oscillations. *J. Electroanal. Chem.* **327**(1-2), 343–349 (1992).

[94] F. Paolucci, L. Peter & J. Stumper. Wavelength-dependent photocurrent multiplication during the anodic dissolution of n-Si in ammonium fluoride solutions. *J. Electroanal. Chem.* **341**, 165 (1992).

[95] K. Krischer, H. Varela, A. Bîrzu, F. Plenge & A. Bonnefont. Stability of uniform electrode states in the presence of ohmic drop compensation. *Electrochimica Acta* **49**, 103–115 (2003).

[96] I. Miethe & K. Krischer. Ellipsomicroscopic studies of the anodic oxidation of p-type silicon in fluoride containing electrolytes during current oscillations. *J. Electroanalyt. Chem.* **666**, 1 (2012).

[97] H. Varela, C. Beta, A. Bonnefont & K. Krischer. A hierarchy of global coupling induced cluster patterns during the oscillatory H_2-electrooxidation reaction on a Pt ring-electrode. *Phys. Chem. Chem. Phys.* **7**, 2429–2439 (2005).

[98] H. Daido & K. Nakanishi. Diffusion-induced inhomogeneity in globally coupled oscillators: Swing-by mechanism. *Phys. Rev. Lett.* **96**, 054101 (2006).

[99] G. C. Sethia & A. Sen. Chimera states: The existence criteria revisited. *Phys. Rev. Lett.* **112**, 144101 (2014).

[100] J. Argyris, G. Faust, M. Haase & R. Friedrich. *Die Erforschung des Chaos*. Springer-Verlag, Berlin Heidelberg (2010).

[101] A. Pikovsky, M. Rosenblum & J. Kurths. *Synchronization: a universal concept in nonlinear sciences*. Cambridge University Press, New York (2003).

[102] M. Falcke & H. Engel. Influence of global coupling through the gas phase on the dynamics of CO oxidation on Pt(110). *Phys. Rev. E* **50**, 1353–1359 (1994).

[103] M. Falcke. Strukturbildung in Reaktions-Diffusions-Systemen und globale Kopplung. *Wiss.-und-Technik-Verlag Gross* (1995).

[104] C. Hemming & R. Kapral. Turbulent fronts in resonantly forced oscillatory systems. *Faraday Discuss.* **120**, 371–382 (2002).

[105] C. Hemming & R. Kapral. Front explosion in a resonantly forced complex Ginzburg–Landau system. *Physica D: Nonlinear Phenomena* **168–169**(0), 10 – 22 (2002).

[106] J. Davidsen, A. Mikhailov & R. Kapral. Front explosion in a periodically forced surface reaction. *Phys. Rev. E* **72**, 046214 (2005).

[107] D. Battogtokh, A. Preusser & A. Mikhailov. Controlling turbulence in the complex Ginzburg-Landau equation II. Two-dimensional systems. *Physica D: Nonlinear Phenomena* **106**(3–4), 327 – 362 (1997).

[108] S. W. Haugland, L. Schmidt & K. Krischer. Self-organized alternating chimera states in oscillatory media. *Scientific Reports* **5**, 9883 (2015).

[109] V. K. Vanag, A. M. Zhabotinsky & I. R. Epstein. Pattern formation in the Belousov-Zhabotinsky reaction with photochemical global feedback. *J. Phys. Chem. A* **104**(49), 11566–11577 (2000).

[110] A. S. Mikhailov & K. Showalter. Control of waves, patterns and turbulence in chemical systems. *Physics Reports* **425**(2–3), 79 – 194 (2006).

[111] A. L. Lin, A. Hagberg, E. Meron & H. L. Swinney. Resonance tongues and patterns in periodically forced reaction-diffusion systems. *Phys. Rev. E* **69**, 066217 (2004).

[112] P. Kaira, P. S. Bodega, C. Punckt, H. H. Rotermund & D. Krefting. Pattern formation in 4:1 resonance of the periodically forced CO oxidation on Pt(110). *Phys. Rev. E* **77**, 046106 (2008).

[113] K. Okuda. Variety and generality of clustering in globally coupled oscillators. *Physica D: Nonlinear Phenomena* **63**(3–4), 424 – 436 (1993).

[114] P. Coullet & K. Emilsson. Strong resonances of spatially distributed oscillators: a laboratory to study patterns and defects. *Physica D: Nonlinear Phenomena* **61**(1–4), 119 – 131 (1992).

[115] V. Petrov, Q. Ouyang & H. L. Swinney. Resonant pattern formation in a chemical system. *Nature* **388**, 655–657 (1997).

[116] A. Yochelis, C. Elphick, A. Hagberg & E. Meron. Frequency locking in extended systems: The impact of a Turing mode. *EPL (Europhysics Letters)* **69**(2), 170 (2005).

[117] J. M. Conway & H. Riecke. Multiresonant forcing of the complex Ginzburg-Landau equation: Pattern selection. *Phys. Rev. E* **76**, 057202 (2007).

[118] B. Marts, A. Hagberg, E. Meron & A. L. Lin. Resonant and nonresonant patterns in forced oscillators. *Chaos* **16**, 037113 (2006).

[119] A. Yeldesbay, A. Pikovsky & M. Rosenblum. Chimeralike states in an ensemble of globally coupled oscillators. *Phys. Rev. Lett.* **112**, 144103 (2014).

[120] N. Nakagawa & Y. Kuramoto. From collective oscillations to collective chaos in a globally coupled oscillator system. *Physica D: Nonlinear Phenomena* **75**(1–3), 74 – 80 (1994).

[121] M. Bertram, C. Beta, H. H. Rotermund & G. Ertl. Complex patterns in a periodically forced surface reaction. *The Journal of Physical Chemistry B* **107**(35), 9610–9615 (2003).

[122] W. Vance & J. Ross. A detailed study of a forced chemical oscillator: Arnol'd tongues and bifurcation sets. *The Journal of Chemical Physics* **91**(12), 7654–7670 (1989).

[123] W. N. Vance & J. Ross. Bifurcation structures of periodically forced oscillators. *Chaos: An Interdisciplinary Journal of Nonlinear Science* **1**(4), 445–453 (1991).

[124] M. Golubitsky & I. Stewart. *The Symmetry Perspective: From Equilibrium to Chaos in Phase Space and Physical Space*. Birkhäuser Verlag, Basel (2003).

[125] M. Pollmann, M. Bertram & H. H. Rotermund. Influence of time delayed global feedback on pattern formation in oscillatory CO oxidation on Pt(110). *Chem. Phys. Lett.* **346**(1–2), 123 – 128 (2001).

[126] A. Yochelis, A. Hagberg, E. Meron, A. L. Lin & H. L. Swinney. Development of standing-wave labyrinthine patterns. *SIAM J. Appl. Dyn. Sys.* **1**, 236 (2002).

[127] A. Yochelis. Pattern formation in periodicaly forced oscillatory systems. *PhD Thesis, Ben-Gurion University* (2004).

[128] J. Guckenheimer. Multiple bifurcation problems of codimension two. *SIAM J. Math. Anal.* **15**(1), 1–49 (1984).

[129] L. Schmidt & K. Krischer. Two-cluster solutions in an ensemble of generic limit-cycle oscillators with periodic self-forcing via the mean-field. *Phys. Rev. E* **90**, 042911 (2014).

[130] L. Schmidt & K. Krischer. Clustering as a prerequisite for chimera states in globally coupled systems. *Phys. Rev. Lett.* **114**, 034101 (2015).

[131] V. K. Chandrasekar, R. Gopal, A. Venkatesan & M. Lakshmanan. Mechanism for intensity-induced chimera states in globally coupled oscillators. *Phys. Rev. E* **90**, 062913 (2014).

[132] M. Wolfrum & O. E. Omel'chenko. Chimera states are chaotic transients. *Phys. Rev. E* **84**, 015201 (2011).